Metallic Micro-cantilever Resonators: Fabrication and Mechanical Property Measurements

by

Serhat YAVUZ

A Thesis Submitted to the

Graduate School of Engineering

in Partial Fulfillment of the Requirements for

the Degree of

Master of Science

in

Mechanical Engineering

Koç University

October 2010

Koç University

Graduate School of Sciences and Engineering

This is to certify that I have examined this copy of a master's thesis by

Serhat YAVUZ

and have found that it is complete and satisfactory in all respects,

and that any and all revisions required by the final

examining committee have been made.

Committee Members:

B. Erdem Alaca, Ph.D. (Advisor)

Hakan Ürey, Ph.D.

Demircan Canadinç, Ph.D.

Date: 08 October 2010

ABSTRACT

The objective of this work is to improve the performance of a micro-cantilever resonator by modifying its fabrication flow and by measuring actual mechanical properties of its structural constituents. The latter is important for the quantification of biological measurements as resonators are intended to be used in biological sensing applications. Electro-plating, one of the critical steps in the proposed fabrication method of the biosensor chip is studied. The effect of changing current density and time to deposited nickel thickness and surface roughness is illustrated. For 1000 nm nickel thickness, a surface roughness range between 10-20 nm is obtained. By using a new photolithography layout, same fabrication procedure is carried out both on silicon and silicon-on-insulator (SOI) wafers, and obtained results on these substrates are compared. The surface roughness for the etched gap underneath the micro-cantilevers is decreased from 15-30 nm to 0.5-5 nm when switched from silicon wafer to SOI wafer. It is seen that better surface properties are obtained with SOI samples which is also more suitable for the optical resonance frequency measurement setup.

In continuation of this thesis, modulus of elasticity values for materials used in the fabrication of micro-cantilever resonators are determined by using resonance technique. Theoretical formulations and optical measurement setups used in this method are demonstrated. At the end, 165.5 GPa is obtained for the modulus of elasticity of electro-plated nickel (800 nm-thick) with a standard deviation of 10.5 GPa; 53.75 GPa is obtained for the modulus of elasticity of RF sputtered gold (100 nm-thick) with a standard deviation of 39.37 GPa; 67 GPa is obtained for the modulus of elasticity of RF sputtered chromium (20 nm-thick) with a standard deviation of 16 GPa. Obtained modulus values for thin nickel, gold and chromium films are in good agreement with what was found in the literature before. Finally, the change in the resonance frequency and the reliability of double-layered double-clamped micro cantilevers are studied over a 10-month period. The reliability study did not allow us to reach a conclusion about the factors affecting the resonance frequency of these devices.

ÖZET

Bu çalışmanın amacı bir konsol kiriş yapılı mikro çınlacın üretim şemasını tadil ederek ve çınlacın yapısal bileşenlerinin mekanik özelliklerini ölçerek performansını yükseltmektir. Çınlaçlar biyolojik algılama uygulamalarında kullanılacağından ikinci husus biyolojik ölçümlerin miktarının belirlenmesi açısından önemlidir. Biyolojik algılayıcı yongası için önerilen üretim metodunun en kritik basamaklarından biri olan elektro-kaplama, çalışıldı. Değişen akım yoğunluğunun ve kaplama zamanının kaplanan nikel kalınlığına ve yüzey pürüzlüğüne olan etkisi araştırıldı. 1000 nm nikel kalınlığı için 10-20 nm'lik yüzey pürüzlüğü elde edildi. Yeni bir fotolitografi serim tasarımı kullanılarak aynı üretim yolu hem silisyum hem de yalıtkan katman üstündeki silisyum (SOI) tabakalarda uygulandı ve bu tabakalarda elde edilen sonuçlar karşılaştırıldı. Silisyum alttaştan SOI alttaşa geçildiğinde mikro konsol kirişin altındaki oyulmuş yüzeyin pürüzlülüğü 15–30 nm'den, 0.5–5 nm'ye düştü. Bu sayede SOI numuneler ile optik çınlanım frekans ölçüm düzeneği açısından daha uygun ve güzel yüzey özellikleri elde edildi.

Çalışmanın devamında, çınlanım tekniği kullanılarak konsol kiriş yapılı mikro çınlaçların üretiminde kullanılan malzemelerin elastisite modülleri belirlendi. Teorik formüller ve çınlanım tekniği için kullanılan optik ölçüm düzenekleri gösterildi. En sonunda, elektro-kaplanmış nikelin (800 nm kalınlığında) elastisite modülü için 10.5 GPa standart sapma ile 165.5 GPa, RF-saçtırılmış altının (100 nm kalınlığında) elastisite modülü için 39.37 GPa standart sapma ile 53.75 GPa, RF-saçtırılmış kromun (20 nm kalınlığında) elastisite modülü için 16 GPa standart sapma ile 67 GPa bulundu. Nikel, altın ve krom katmanları için elde edilen modül değerlerinin daha önceki çalışmalarda bulunan değerler ile uyum içerisinde olduğu görüldü. Son olarak, çift katmalı ve iki yerden tutturulmuş mikro konsol kiriş yapıların çınlanım frekanslarındaki değişim ve bu yapıların güvenilirliği 10 ay boyunca çalışıldı.

Güvenilirlik testi bu cihazların çınlanım frekansına etki edecek faktörler hakkında bir sonuca varmamıza izin vermedi.

ACKNOWLEDGEMENTS

At the beginning, I would like to thank my advisor Asst. Prof. B. Erdem Alaca because of leading to a completely new experience in my life. Without him, I could hardly imagine to be a part of this continuously developing technology in the world. He is a wonderful guide, and cares his students all the time during their researches.

I also want to thank Asst. Prof. Demircan Canadinç and Assoc. Prof. Hakan Ürey for being in my thesis committee and for their valuable ideas during our studies.

I would like to specially thank my colleague M. Salih Kılıç because of sharing his experience, time, thoughts and advices inside and outside this project. His assistance makes me adapt the project more quickly and efficiently. I also want to appreciate my other colleagues Natali Özber and Yasin Kılınç for their contributions to my studies.

In addition to these people, I want to thank Selim Ölçer, Onur Ferhanoğlu, Erdem Erden, Erman Timurdoğan, Sven Holmström, Siva Konduri, Jaibir Sharma and all other Optical Microsystems Laboratory (OML) members for their kind behavior and help during my measurements with electrical equipment. Here, I would like to emphasize the help of Erdal Uzunlar because of letting me to use his measurement set-up place at rush times.

Furthermore, I have to say that it is a great pleasure for me to be a part of KoçFutbol group which enjoys us during our hard working studies.

Finally, I want to thank my family and my relatives for their continuous support, motivation and advice while walking in this different way.

TABLE OF CONTENTS

ABSTRACT .... **I**

ÖZET .... **III**

ACKNOWLEDGEMENTS .... **V**

TABLE OF CONTENTS .... **VI**

LIST OF TABLES .... **VIII**

LIST OF FIGURES .... **IX**

NOMENCLATURE .... **XVI**

CHAPTER 1 - INTRODUCTION **1**

- 1.1. OVERVIEW & BACKGROUND 1
  - 1.1.1. MICRO-CANTILEVERS AS BIOLOGICAL SENSORS 4
  - 1.1.2. DETERMINATION OF MECHANICAL PROPERTIES WITH MICRO-CANTILEVERS 7
  - 1.1.3. BASIC FABRICATION TECHNIQUES FOR A MICRO-CANTILEVER 9
  - 1.1.4. MICRO-CANTILEVER ARRAYS 11
- 1.2. STATEMENT OF THE PROBLEM 16
- 1.3. OUTLINE 16

CHAPTER 2 - FABRICATION **18**

- 2.1. FABRICATION FLOW OF A BIOSENSOR CHIP 18
- 2.2. ELECTRO-PLATING CURVES 24
- 2.3. 2^{ND} GENERATION LAYOUT 37
  - 2.3.1. FABRICATION ON SILICON WAFER 40

2.3.2. FABRICATION ON SILICON-ON-INSULATOR (SOI) WAFER 46
2.4. OPTIMIZATION WORK ON FABRICATION 49
2.4.1. IMPROVEMENTS ON LITHOGRAPHY 49
2.4.2. WET ETCHING OF SILICON LAYER 51
2.4.3. WET ETCHING OF GOLD LAYER UNDERNEATH NICKEL LAYER 55
CHAPTER 3 - USE OF RESONANCE TECHNIQUE IN THE DETERMINATION OF THE MODULUS OF ELASTICITY 59
3.1. EXPERIMENTAL SETUPS 67
3.2. RESONANCE BEHAVIOR 74
3.3. THEORETICAL FORMULATIONS 77
3.4. MEASUREMENTS & RESULTS 80
3.4.1. MEASUREMENT OF NICKEL MODULUS OF ELASTICITY 80
3.4.2. MEASUREMENT OF GOLD MODULUS OF ELASTICITY 85
3.4.3. MEASUREMENT OF CHROMIUM MODULUS OF ELASTICITY 90
3.5. RELIABILITY STUDY 93
CHAPTER 4 - CONCLUSION & FUTURE WORK 100
4.1. CONCLUSION 100
4.2. FUTURE WORK 103
APPENDIX A 105
A.1. ZINC SELENIDE (ZNSE) CRYSTAL 106
A.2. WAGON WHEEL 110
A.3. INDIUM TIN OXIDE (ITO) 113
BIBLIOGRAPHY 115
VITA 122

LIST OF TABLES

Table 1.1 – Different types of etching (Adapted from Refs. [33, 35]) 11

Table 2.1 – Biosensor Chip Fabrication Processs 24

Table 2.2 – Photolithography calibration experiment 50

Table 2.3 – Comparison between the old and new recipes for anisotropic silicon etching process.. 54

Table 2.4 – Comparison between Transene Inc. GE-8148® and Diluted Aqua Regia gold etchants 58

Table 3.1 – Modulus of elasticity values for the nickel thin films obtained in different experiments (Adapted from Ref. [23]).. 61

Table 3.2 – Experimental resonance frequency data (“IZ” defines the grating geometry of the cantilever beams which is introduced in the thesis of Hüseyin İlker Ocaklı [16])... 76

Table 3.3 – Nickel Modulus of Elasticity (# of measurements: 70 for Region – 1, 49 for Region – 2)... 83

Table 3.4 – $\sqrt{E/\rho}$ Term for Nickel Modulus of Elasticity (# of measurements: 70 for Region – 1, 49 for Region – 2)... 85

Table 3.5 – Gold Modulus of Elasticity (# of measurements: 28 for Region – 1, 41 for Region – 2)... 89

Table 3.6 – Chromium Modulus of Elasticity (for 20 nm sputtered chromium thickness) (# of measurements: 30 for Region – 1, 29 for Region – 2)................. 92

LIST OF FIGURES

Figure 1.1 – Schematic views of the possible usage of a MEMS cantilever: a) AFM force sensor, b) temperature or heat sensor, c) medium viscoelasticity sensor, d) mass sensor with an end load, e) stress sensor, f) a sensor for monitoring the magnetic particles on the cantilever surface 2

Figure 1.2 – The cantilever beam bends as the biological material binds onto its surface 5

Figure 1.3 – a) The resonance mode of a cantilever beam, b) the difference in frequency for two states (The shift in the resonance frequency after mass binding can be easily seen in Figure 1.3(b)) 6

Figure 1.4 – Schematic description of the photolithography process: a) Spin-coating of photoresist onto the SiO_2 surface, b) Negative and Positive PR is exposed to UV light according to the photomask, c) Photomask is removed and exposed region is developed, d) SiO_2 surface is etched with respect to PR (At the end, remaining PR on the oxide surface is removed.) (Adapted from Ref. [34]) 10

Figure 1.5 – Schematic view of a micro-cantilever array functionalized with different molecules 12

Figure 1.6 – Results obtained in the His-tagged hKOR protein and *anti-His* antibody experiment 14

Figure 1.7 – Results obtained in Hepatitis A and Hepatitis C experiments 15

Figure 2.1 – Electro-plating process setup: 1) Bio-sensor chip attached with four crocodile cables from four contact places, 2) Nickel Sulphamate solution, 3) Nickel Target Anode, 4) Thermometer for measuring the solution temperature, 5) Magnetic heater for adjusting temperature and stirring solution, 6) Digital

Multimeter for monitoring the current, 7) Power Supply for controlling the voltage and current (The inset shows a schematic view taken from Ref. [42]) 20

Figure 2.2 – Schematic view of the fabrication flow of a Biosensor Chip............22

Figure 2.3 – An array of fabricated cantilevers with a width of 7 µm...................23

Figure 2.4 – Temperature, current density and time effects to the electro-plating process: a) Nickel thickess vs. time graph (short term), b) Nickel thickness vs. time graph (long term), c) Nickel thickness vs. current density graph obtained after 5-minute deposition for different temperatures, d) Nickel thickness vs. temperature graph obtained after 5-minute deposition for different current densities 25

Figure 2.5 – Nickel thickness vs. current density (Constant time: 20 minutes, Constant temperature: 45°C) 27

Figure 2.6 – R_a (Arithmetic Average Surface Roughness) vs. current density (Constant time: 20 minutes, Constant temperature: 45°C)...................................27

Figure 2.7 – R_q (Root Mean Squared Surface Roughness) vs. current density (Constant time: 20 minutes, Constant temperature: 45°C)...................................28

Figure 2.8 – R_q (Root Mean Squared Surface Roughness) vs. nickel thickness (Constant time: 20 minutes, Constant temperature: 45°C)...................................28

Figure 2.9 – The definition of Arithmetic Average surface roughness (R_a)..........29

Figure 2.10 – The definition of Root Mean Squared surface roughness (R_q) 29

Figure 2.11 – Nickel thickness vs. time (Constant current density: 14.661 mA/cm^2, Constant temperature: 45°C) 31

Figure 2.12 – R_a (Arithmetic Average Surface Roughness) vs. time (Constant current density: 14.661 mA/cm^2, Constant temperature: 45°C)............................31

Figure 2.13 – R_q (Root Mean Squared Surface Roughness) vs. time (Constant current density: 14.661 mA/cm^2, Constant temperature: 45°C)............................32

Figure 2.14 – R_q (Root Mean Squared Surface Roughness) vs. nickel thickness (Constant current density: 14.661 mA/cm^2, Constant temperature: 45°C) 32

Figure 2.15 – R_a (Arithmetic Average Surface Roughness) vs. current density ...34

Figure 2.16 – R_q (Root Mean Squared Surface Roughness) vs. current density....34

Figure 2.17 – Deflection data for cantilevers without gratings 35

Figure 2.18 – Deflection data for cantilevers with gratings 36

Figure 2.19 – Top views of the deflected cantilevers with fringes (Cantilever dimensions are 4 μm in width and 49 μm in length) 36-37

Figure 2.20 – Nickel Mask Design: 1) 4" wafer with chips, 2) One single chip with contact places at each corner, 3) Cantilevers clamped to both sides of anchors, 4) Cantilevers with different gratings at the tips 39

Figure 2.21 – Gold (Functionalization) Mask Design: 1) 4" wafer with chips, 2) One single chip, 3) Differently functionalized cantilevers with labels between, 4) Differently functionalized cantilevers with labels between (Closer view) 40

Figure 2.22 – Electro-plated quarter wafer...42

Figure 2.23 – Better contact places on the corners of the chips obtained with electro-plating of the quarter wafer 43

Figure 2.24 – Gold and chromium layers etched quarter wafer 44

Figure 2.25 – One-end-fixed cantilevers fabricated with 2nd Generation Layout on silicon wafer. a) cantilevers with 21 μm x 31 μm and 45° aligned gratings (10x magnification), b) cantilevers with 21 μm x 31 μm and 45° aligned gratings (20x magnification), c) cantilevers with 100 μm x 100 μm geometry (20x magnification), d) cantilevers with 70 μm x 70 μm geometry (20x magnification). 45

Figure 2.26 – The schematic view of an SOI wafer 46

Figure 2.27 – Cantilevers fabricated with 2^{nd} Generation Layout on SOI wafer. a) One-end-fixed cantilevers with 21 µm x 21 µm and 0° aligned gratings (10x magnification), b) One-end-fixed cantilevers with 21 µm x 21 µm and 0° aligned gratings (20x magnification), c) One-end-fixed cantilevers with 21 µm x 36 µm and 0° aligned gratings (10x magnification), d) One-end-fixed cantilevers with 21 µm x 36 µm and 0° aligned gratings (20x magnification), e) Tuning fork cantilevers with 21 µm x 21 µm and 0° aligned gratings (10x magnification), f) Tuning fork cantilevers with 21 µm x 21 µm and 0° aligned gratings (20x magnification).. 47-48

Figure 2.28 – Better patterned surfaces obtained with photolithography calibration experiment a) Static cantilevers having 75 µm x 400 µm geometry (10x magnification), b) Static cantilevers having 75 µm x 400 µm geometry (20x magnification), c) Static cantilevers having 100 µm x 500 µm geometry (10x magnification), d) Static cantilevers having 100 µm x 500 µm geometry (20x magnification) 50-51

Figure 2.29 – Released 7 µm-width cantilevers with sticking and silicon surface problems 53

Figure 2.30 – Released 7 µm-width cantilevers after solving the sticking and silicon surface problems 54-55

Figure 2.31 – The precipitation formation as a result of etching the gold layer underneath the nickel layer...56

Figure 2.32 – Black dust formation on the 11 µm-width cantilevers as a result of etching the gold layer underneath the nickel layer...57

Figure 2.33 – Released 9 µm-width cantilevers after etching the gold layer underneath the nickel layer with Aqua Regia...58

Figure 3.1 – Different cantilever structures are used to obtain modulus of elasticity values 60

Figure 3.2 – Modulus of Elasticity values for electro-plated nickel thin films 62

Figure 3.3 – Modulus of Elasticity values for commercial electro-plated nickel thin films 63

Figure 3.4 – Current Density effect to Nickel Modulus of Elasticity 64

Figure 3.5 – Modulus of elasticity values for thermally evaporated chromium cantilevers with sub-100 nm thicknesses 65

Figure 3.6 – Formation of diffraction grating orders 68

Figure 3.7 – Comparison of LDV and Laser-PD setups (Cantilever dimensions are 12 μm in width and 60 μm in length) 69

Figure 3.8 – The schematic view of the Laser-PD mechanism 70

Figure 3.9 – The actual view of the Laser-PD mechanism: 1) Thermometer and Hygrometer for temperature and relative humidity measurements, 2) Microscope for viewing the measured micro-cantilevers, 3) Input (green) and output (white) signals on the oscilloscope screen, 4) XYZ Stage for adjusting the micro-cantilever position, 5) Electrocoil for providing the magnetic actuation, 6) Micro-cantilever, 7) Laser Aperture, 8) Photodiode, 9) Optical Lens, 10) Light for increasing the visibility of micro-cantilevers in the microscope, 11) 633 nm HeNe Laser source71

Figure 3.10 – The schematic view of the LDV mechanism 72

Figure 3.11 – A sample graph obtained with the frequency sweep method 73

Figure 3.12 – Resonance frequency variation with respect to thickness change 75

Figure 3.13 – Resonance frequency variation with respect to length change 76

Figure 3.14 – Sample cantilever beam used in nickel modulus of elasticity experiment (ANSYS model) 81

Figure 3.15 – Different regions on the chip..82

Figure 3.16 – Size comparison between the fabricated cantilever having geometry of 7 μm x 70 μm and its L-edit design..84

Figure 3.17 – Sample cantilever beam used in gold modulus of elasticity experiment (ANSYS model)...87

Figure 3.18 – Size comparison between the fabricated cantilever having geometry of 7 μm x 70 μm and its L-edit design..88

Figure 3.19 – SEM images of a fabricated cantilever: a) 5 μm-width cantilever having a length of 25 μm, b) 5 μm-width cantilever having a length of 50 μm 90

Figure 3.20 – Sample bridge-structured cantilever beam used in Reliability Study 94

Figure 3.21 – Resonance frequency variation with respect to the environmental factors (for 7x70IZ53 type geometry) (# of measurements: 10) 95

Figure 3.22 – Resonance frequency variation with respect to the environmental factors (for 7x105IZ53 type geometry) (# of measurements: 20) 95

Figure 3.23 – Resonance frequency variation with respect to the environmental factors (for 7x140IZ53 type geometry) (# of measurements: 20) 96

Figure 3.24 – Resonance frequency variation with respect to the environmental factors (for 8x80IZ53 type geometry) (# of measurements: 20) 96

Figure 3.25 – Resonance frequency variation with respect to the environmental factors (for 8x120IZ53 type geometry) (# of measurements: 16) 97

Figure 3.26 – Resonance frequency variation with respect to the environmental factors (for 8x160IZ53 type geometry) (# of measurements: 15) 97

Figure A.1 – ZnSe crystal after being etched in the $KMnO_4$, H_2SO_4 and DI water solution 107

Figure A.2 – Schematic view of the fabrication flow used in ZnSe crystal etching rate experiment 108

Figure A.3 – Obtained wagon-wheel structure at the end of the experiment (Red lines on Figure A.3(a) and A.3(b) show the deepened silicon surfaces with KOH solution) 111

Figure A.4 – Schematic view of the fabrication flow used in the wagon wheel experiment 112

Figure A.5 – Schematic view of the fabrication flow used in ITO experiment.... 114

NOMENCLATURE

E	Modulus of Elasticity / Young's Modulus parameter
E_1	Modulus of Elasticity for the first layer of the cantilever beam
E_2	Modulus of Elasticity for the second layer of the cantilever beam
E_3	Modulus of Elasticity for the third layer of the cantilever beam
E_r	Ratio of Modulus of Elasticity for the second layer with respect to the first layer of the cantilever beam
ρ	Density parameter
ρ_1	Density for the first layer of the cantilever beam
ρ_2	Density for the second layer of the cantilever beam
ρ_3	Density for the third layer of the cantilever beam
ρ_r	Ratio of density for the second layer with respect to the first layer of the cantilever beam
$\sqrt{E/\rho}$	Speed of sound
h	Thickness parameter
h_1	Thickness for the first layer of the cantilever beam
h_2	Thickness for the second layer of the cantilever beam
h_3	Thickness for the third layer of the cantilever beam
m	Mass parameter
m_1	Mass for the first layer of the cantilever beam
m_2	Mass for the second layer of the cantilever beam

m_r	Ratio of mass for the second layer with respect to the first layer of the cantilever beam
m^*	Effective mass for the cantilever beam
Δm^*	Effective mass for the bound extra mass onto the cantilever beam surface
Δm	Bound extra mass onto the cantilever beam surface
L	Length of the cantilever beam without grating part at the end
L_0	Original Length
L_1	Length for the first layer of the cantilever beam
L_2	Length for the second layer of the cantilever beam
L_g	Length for the diffraction grating part of the cantilever beam
L^1	Specific length of the cantilever beam with grating part at the end ($L^1 = L + 2L_g / 3$)
ΔL	Change in length
w	Width of the cantilever beam
w_g	Width for the diffraction grating part of the cantilever beam
C	Constant Number = 0,236
A	Surface area of the cantilever beam (wL)
A_R	Total surface area for the diffraction gratings at the end of the cantilever beam (Removed Area)
A_0	Cross-sectional Area
z_0	Neutral Axis of the cantilever beam
Δz	Tip deflection for the cantilever beam
$\Delta \sigma$	Surface Stress
υ	Poisson's Ratio

c	Damping parameter
k	Spring parameter / Stiffness
F	Applied Force
F(t)	External Force
f_o	Resonance Frequency
f_R	Damped Resonance Frequency
f_o^{I}	Resonance Frequency of the cantilever beam after mass binding / Resonance Frequency for mono-layered cantilever beam
f_o^{II}	Resonance Frequency for double-layered cantilever beam
$f_{o-grating}^{II}$	Resonance Frequency for double-layered cantilever beam with a grating structure at its tip
$f_{o-grating}^{III}$	Resonance Frequency for triple-layered cantilever beam with a grating structure at its tip
Q	Quality Factor
β	Damping factor
R_a	Arithmetic Average Surface Roughness
R_q	Root Mean Squared Surface Roughness
σ	Uniaxial Stress
ε	Uniaxial Strain

Chapter 1 - INTRODUCTION

1.1. Overview & Background

As an early example of a MEMS cantilever sensor, resonistor is an important device which is used as an electromechanical monolithic resonator in early 1970s [1]. It is basically a micro-cantilever which can be deflected by thermal expansion that is induced electrically. As a result of this deflection, the stresses on the cantilever can be detected with the help of diffused piezo-resistive elements; and these mechanical stresses help the resonistor to produce an electrical output. The maximum stress and electrical output can be obtained when the cantilever is vibrated at its resonance frequency [1, 2].

With the developing technology in the microelectromechanical systems (MEMS) area, micro-cantilever type structures are considered for many applications. These applications can be classified as infrared detection, gas sensing, acoustic wave detection, particle flux measurements, nano-calorimetry, rheometry, surface stress and magneto-elastic stress measurements [3, 4]. The rapid improvement in this technology leads the utilization of MEMS cantilevers in different areas. In addition to the resonistor, a micro-cantilever can also be used as different sensor devices such as an Atomic Force Microscopy (AFM) force sensor, temperature or heat sensor, medium viscoelasticity sensor, mass sensor, stress sensor and as a magnetic sensor [5]. In Figure 1.1, different types of cantilever sensors for different applications can be seen.

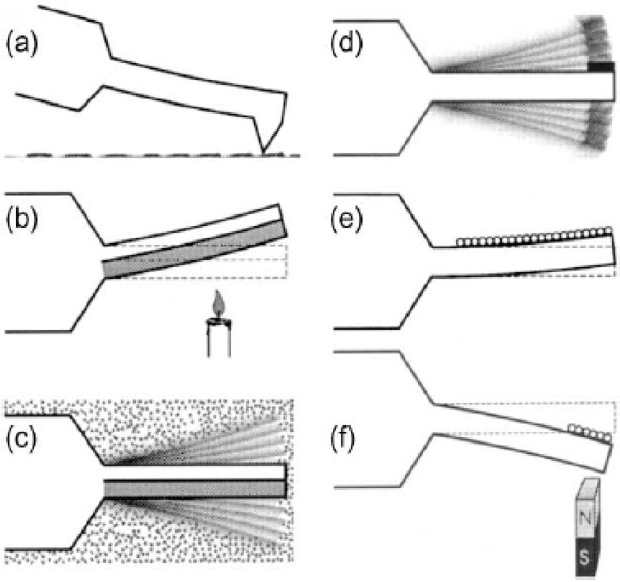

Figure 1.1: Schematic views of the possible usage of a MEMS cantilever: a) AFM force sensor, b) temperature or heat sensor, c) medium viscoelasticity sensor, d) mass sensor with an end load, e) stress sensor, f) a sensor for monitoring the magnetic particles on the cantilever surface. [5]

AFM force sensor is an important device for measuring the displacement and strain behavior of materials in nanometer scale. The displacement of the material can be provided with electro-thermal actuation, and the displacement field is determined by comparing the different surface topologies obtained for deformed and undeformed cases which are acquired with an AFM device [6]. With an integrated sharp stylus at its free end, AFM provides an improved resolution for the surface scanning [5]. Furthermore, AFM can be used to investigate the interactions and binding issues between biological matter such as antigens, antibodies and different DNA strands [5]. In addition to these applications, MEMS-based cantilevers can also be used as temperature, heat, pressure or gas flow sensors. As a result of heat generation or heat change in an environment, cantilevers which are composed of different materials with different thermal expansion coefficients, bend towards a specific direction. This movement gives the cantilever the ability to measure changes in the temperature as small as 10^{-5} K [5, 7].

The bending of cantilever can also help to obtain the velocity and pressure of different gases flowing through the cantilever surface. The velocity of these particles can be obtained by measuring the resistance change on the cantilever surface with the gas flow [8]. Moreover, MEMS-based cantilevers have an important application area as stress sensors in the Aeronautics and Astronautics field. These devices can be developed to measure the shear stress on the walls, tunnels and vessels for an air vehicle flying in severe conditions [7, 9]. Another important application for a MEMS-based cantilever is in magnetic area. These sensors can either be used to detect the magnetic particles on the cantilever surface, or they can be used as magnetic sensors themselves [5, 10]. As a current is applied on the magnetic sensor, sensor makes a movement and a force is generated with the help of magnetic field. Hence, the electrical and magnetic profile of the sensor can be figured out [10].

In addition to using the bending capability of MEMS-based cantilevers, they can be also dynamically vibrated to obtain the resonance frequency. This option gives these devices to be used as viscoelasticity and mass sensors. When placed in a different viscoelastic environment or functionalized with a specific mass, there occurs a change in the resonance frequency. Hence, the properties of the environment or the amount of mass can be detected [5].

Micro-cantilever sensor technology has three main advantages with respect to the other technologies which are being used to detect different substances. First of these is that whole instrumentation used in micro-cantilever sensor technology is relatively simple and inexpensive. Furthermore, since it is easy to get an electrical signal from a micro-cantilever by simply deforming it with external forces or mass accumulation, it is not necessary to consume too much power for detection and measurements. Therefore, a micro-cantilever sensor works with low power. Finally, above all as a result of having a small size, a micro-cantilever can be placed inside device without causing any excessive weight [11]. These advantages make the micro-cantilever sensor technology able to produce small-sized, low-cost, low-power consuming and portable devices for many applications.

In this work, a special emphasis is placed on measurement of biological interactions and mechanical properties at micro scale. Therefore we will focus on the literature on both of these applications in the next sections.

1.1.1. Micro-cantilevers as Biological Sensors

In the last few years, MEMS cantilevers have extended their use with the applications in the biological field. The term “biosensor” entered MEMS field. As a result of performing rapid, local, high resolution, label-free and real-time molecular recognition measurements, bio-sensing became one of the most widespread applications that is performed by using micro-cantilever resonators. Therefore, these miniaturized devices take the basic part of the studies for biological mass detection [4, 12]. Detection of biological mass by using micro-cantilever resonators has many applications in bio-engineering area. This emerging technology raises the opportunity to sense different biological molecules such as proteins, DNA molecules, bacteria and viruses at the same time [13]. In addition to this purpose, micro-cantilever resonators can be used for different applications such as DNA hybridization, bio-marking of different proteins, detection of these biomarkers and providing protein growth and aggregation [4, 14].

A biosensor is composed of three main components which are detector, transducer and a read-out system. The detector recognizes the signal caused by the adsorbed molecule; the transducer converts this signal into an electronic output; and the read-out system filters, amplifies, displays, records or transmits converted signal [5, 14, 15].

The investigation for bio-sensing depends on the application of two different principles of actuation mechanisms which are static mode and dynamic mode. In the static mode, the deflection of the cantilever beam is measured as a result of the adsorption of biological molecules. The deflection on the cantilever is the result of surface stress formation and bending behavior with the material adsorption [3, 15]. In Figure 1.2, the deflection of the cantilever as a result of the material adsorption can be seen.

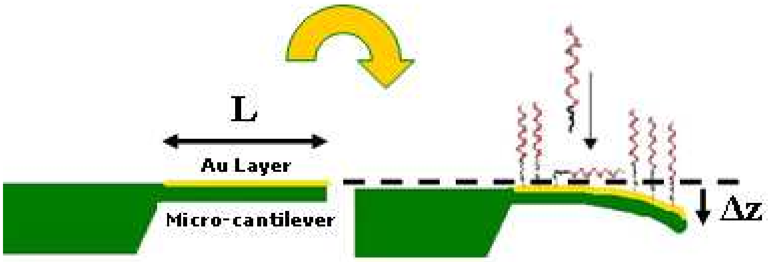

Figure 1.2: The cantilever beam bends as the biological material binds onto its surface. [12]

It can be understood from Figure 1.2 that there is a relationship between the surface stress and deflection of the cantilever beam. This relationship can be expressed with Eqn. 1.1 [4, 11, 13, 14, 16, 17];

$$\Delta z = \frac{3L^2(1-\upsilon)}{Eh^2}\Delta\sigma \qquad \text{(Eqn. 1.1)}$$

where L is the length, Δz is the tip deflection, h is the thickness of the cantilever beam. E is the Young's Modulus (Modulus of Elasticity), υ is the Poisson's Ratio of the cantilever material and $\Delta\sigma$ is the surface stress.

In the dynamic mode, the resonance frequency of the cantilever beam is measured [3, 15]. The measurements for resonance frequency are performed with optical readout mechanisms. According to the shift in the resonance frequency of the cantilever upon binding of a biological molecule, the amount of adsorbed mass onto the cantilever surface can be obtained. [3, 18, 19] In Figure 1.3 below, the difference in the frequency between the reference state (no binding) and the bio-molecular interaction state (binding of biological molecule) for the cantilever in the resonance mode can be seen.

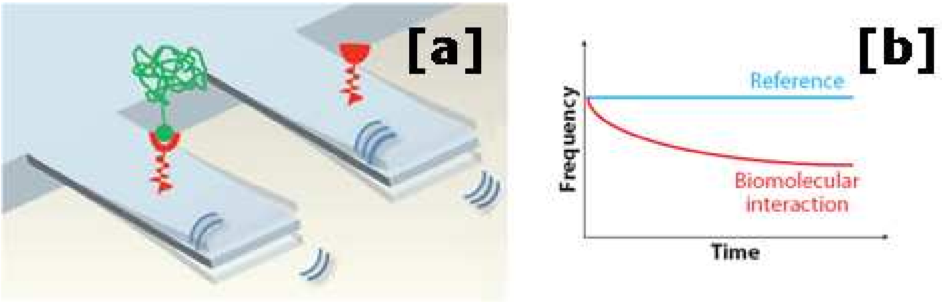

Figure 1.3: a) The resonance mode of a cantilever beam, b) the difference in frequency for two states. (The shift in the resonance frequency after mass binding can be easily seen in Figure 1.3(b)) [13]

The binding of biological mass causes a change in the resonance frequency as it can be seen in Figure 1.3. Since this change is related with the resonance frequency of the cantilever beam, this relationship should be figured out first. The resonance frequency of a cantilever beam can be obtained by constructing a mass-spring-damper system. The relationship for this system is as follows [13];

$$m\frac{d^2x}{dt^2}+c\frac{dx}{dt}+kx=F(t) \qquad \text{(Eqn. 1.2)}$$

where *m*, *c* and *k* are mass, damper and spring parameters and *F(t)* is the external force in this system. If it is assumed that there is no damping (c=0) and external force (F(t)=0) in the system, Eqns. 1.3 and 1.4 can be obtained [11, 13, 16, 17, 20];

$$f_0 = \frac{1}{2\pi}\sqrt{\frac{k}{m^*}} \qquad \text{(Eqn. 1.3)}$$

$$f_0^{\prime} = \frac{1}{2\pi}\sqrt{\frac{k}{m^* + \Delta m^*}} \qquad \text{(Eqn. 1.4)}$$

where f_0 is the resonance frequency for the unloaded initial case and $f_0^{\prime}$ is the case for binding of substance. Also, m^* is the effective mass for the cantilever beam and Δm^* is the effective bound biological mass onto the cantilever surface. If this mass is assumed to be distributed uniformly on the cantilever surface, m^* is equal to $0.236\times m$ and Δm^* is equal to $0.236\times\Delta m$ for a rectangular cantilever beam [13, 16, 17, 20]. By combining Eqns. 1.3 and 1.4, the amount of the bound biological mass can be calculated by using the Eqn. 1.5 [13, 16, 17, 20].

$$\Delta m = \frac{k}{4\pi^2}\left(\frac{1}{f_0^{\prime 2}} - \frac{1}{f_0^2}\right) \qquad \text{(Eqn. 1.5)}$$

1.1.2. Determination of Mechanical Properties with Micro-cantilevers

Another important application which can be performed with micro-cantilevers besides biological detection is the determination of mechanical properties of thin film materials. As one of the most important mechanical properties of materials, Modulus of Elasticity is the measure of stiffness for elastic materials. It can be expressed as the slope in the elastic region of stress-strain curve. This expression can be formulated by Hooke's Law as in Eqn. 1.6 [21, 22];

$$E = \frac{\sigma}{\varepsilon} = \frac{F/A_0}{\Delta L/L_0} \qquad \text{(Eqn. 1.6)}$$

where E is modulus of elasticity, σ is uniaxial stress and ε is uniaxial strain. In Eqn. 1.6, it can be seen that stress (σ) is the applied force (F) onto a cross-section of a material (A_0), and strain (ε) is the ratio of change in material length (ΔL) as a result of the applied force (F) to the original material length (L_0).

Previous studies [23 – 29] showed that modulus of elasticity value for thin film materials can be much different with respect to original bulk values. In order to obtain modulus of elasticity values for these materials, micro-cantilever technology can be used. Measuring resonance frequency of a micro-cantilever is an important method for determining the modulus of elasticity of thin films. In the literature, it was witnessed that some studies used resonance method in order to measure the mechanical properties of micro-machined structures [25, 26, 28, 30, 31]. In 1979, *Petersen* used resonance method for the first time for determining the modulus of elasticity of micromechanical thin films [30].

Since the dimensional properties of a micro-cantilever are known, modulus of elasticity can be determined by using a theoretical formulation after measuring the resonance frequency. The resonance frequency formulation is defined with Eqn. 1.7 [28, 30];

$$f_0 = \frac{\lambda^2 h}{4\pi L^2}\left(\frac{E}{3\rho}\right)^{1/2} \qquad \text{(Eqn. 1.7)}$$

where f_0 is the resonance frequency, h is the thickness of micro-cantilever, L is the length of micro-cantilever, E is the modulus of elasticity, ρ is the density and λ is 1.875 which represents first resonance mode eigenvalue.

1.1.3. Basic Fabrication Techniques for a Micro-cantilever

For the fabrication of a micro-cantilever based biosensor, the typical materials such as silicon (Si), silicon nitride (Si_3N_4) and silicon oxide (SiO_2) can be used with different shapes, dimensions and stiffness properties [5, 12]. These materials can either be used as wafers which are the ideal places for performing the whole fabrication processes, or be used as specific layers of a micro-structure. In a typical fabrication process, it is possible to meet with different geometries and structures with different dimensions and properties. These geometries can be produced by using a special technique which is called "photolithography". As one of the most fundamental processes in a MEMS-based fabrication, this technique requires the usage of a photomask and a high-intensity light (UV light). With this technique which was developed in 1959, the shape of a photomask can be transposed on a silicon wafer with the help of a light-dependent and light-sensitive material which is "photoresist" [32]. Photoresist compound can be either positive or negative according to the desired structure and used photomask. When a positive photoresist is used, radiation-exposed areas are washed away because of the weakening of polymers by chain scission. However when a negative photoresist is used, radiation-exposed areas remain because of the strengthening of polymers by cross-linking [32, 33]. In Figure 1.4, the photolithography process can be seen.

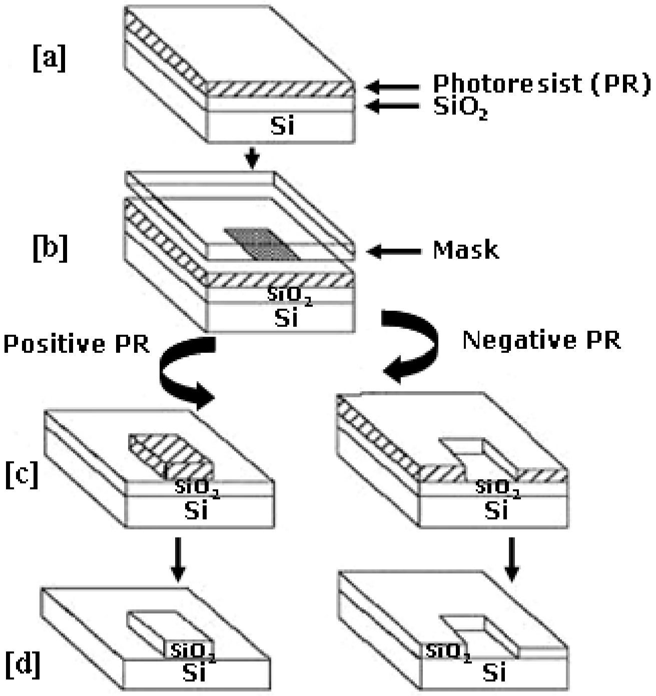

Figure 1.4: Schematic description of the photolithography process: a) Spin-coating of photoresist onto the SiO_2 surface, b) Negative and Positive PR is exposed to UV light according to the photomask, c) Photomask is removed and exposed region is developed, d) SiO_2 surface is etched with respect to PR. (At the end, remaining PR on the oxide surface is removed.) (Adapted from Ref. [34])

In Figure 1.4, it can be seen that when a positive type photoresist is used exposed areas are gone after being exposed to UV light; when a negative type photoresist is used exposed areas remain after being exposed to UV light. Photolithography is also a critical process for the protection of some specific places on the wafers during fabrication.

As the patterns are formed on the wafer, another important process is applied which is “etching”. Etching is another basic process in this type of fabrication, and it has many different types. Etching is necessary for removing the patterned layers around a structure, or for releasing this structure. In Table 1.1 below, different etching types with their applications and other important characteristics can be seen.

Type No.	**Etching Technique**	**Applications**	**Typical Etch Rate (µm/min)**	**Remarks**
1	Wet Chemical Etching	Cantilevers, bridges, grooves	1-50	Simple, but poor control
2	Electrochemical Etching	Etch stop technique	1.25-1.75 (for p-Si)	Complex, require electrode
3	Dry Chemical Etching	Resist Stripping, Isotropic features	0.1 (for Si)	Resolution better than 0.1 µm
4	Physical / Chemical Etching	Very precise pattern transfer	0.1-1 (for Si)	Most important of dry etching
5	Focused ion-beam Milling	Microstructures in arbitrary materials	1 (for Si)	Long fabrication time

Table 1.1: Different types of etching. (Adapted from Refs. [33, 35])

Wet chemical etching is one of the most widespread techniques for fabricating the micro-cantilevers. In spite of having a poor control in the fabrication process, wet etching provides a higher selectivity for the materials with respect to the dry etching techniques. Also, the process takes much longer for dry etching than wet etching [33]. Poor control for the wet chemical etching can be prevented by agitating the substrate inside the etchant.

1.1.4. Micro-cantilever Arrays

Continuously developing technology in this area makes it possible to use multiple cantilevers and cantilever arrays for the detection of many biological molecules at once [4, 14, 18, 36]. According to this technology, each micro-cantilever sensor in the array is functionalized with specific biological materials by using special techniques, so each of them becomes sensitive to different molecules. This fact provides the rapid and real-time detection of many substances at the same time. In Figure 1.5, the schematic view of a sample micro-cantilever array can be seen.

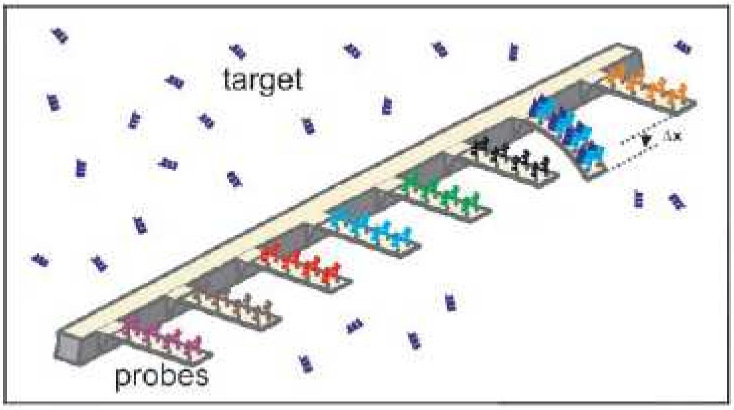

Figure 1.5: Schematic view of a micro-cantilever array functionalized with different molecules. [36]

However, using cantilever arrays instead of just one cantilever resonator may cause difficulties and errors for obtaining the properties of adsorbed mass [18]. The location of the adsorbed mass on a cantilever beam may not be same for every cantilever when a cantilever array is in question. And, this non-uniformity in the mass accumulation directly affects the resonance frequency measurements and calculations. With respect to these, there occurs confusion with the calculated mass by theoretical formulations and experimentally adsorbed mass [18, 37]. This fact can cause serious problems for the detection of a biological solution which includes many different molecules inside it. This situation makes the sensitivity an important concept for the micro-cantilever array technology.

Sensitivity of a micro-cantilever resonator directly depends on some critical factors such as resonance frequency, deflection, size of the cantilever beams and concentration of the biological materials. The sensitivity of a cantilever beam is directly proportional with resonance frequency, deflection of the cantilever beam and concentration of the molecules; but it is inversely proportional with the mass of the cantilever beam [4, 14, 19, 36, 38]. It is critical to produce a highly-sensitive micro-cantilever resonator in order to understand the amount of adsorbed molecule even in solutions with low concentrations [14, 38].

Two biological studies were carried out in relation to the work reported in this thesis:

1) Selective binding of the *anti-His* antibody on the His-tagged hKOR protein is studied. In that manner, two different chips including micro-cantilever resonators are prepared. The resonance frequencies of some specific cantilevers are measured in both chips inside a buffer solution (PBS) at first. Then, the resonance frequencies of the same cantilevers in the first chip (to serve as a reference) are measured inside different *anti-His* antibody concentrations between 80 ng/mL and 2 μm/mL without functionalizing the surface. The surface of the cantilevers in the second chip is functionalized with a linker, Dithiobis (Succinimidyl Propionate) (DSP). After that, His-tagged hKOR protein is immobilized onto the surfaces of the cantilevers with the help of DSP. Finally, the resonance frequencies of these cantilevers are measured inside same *anti-His* antibody concentrations between 80 ng/mL and 2 μg/mL as performed for the first chip [39]. The results obtained in this experiment can be seen in Figure 1.6.

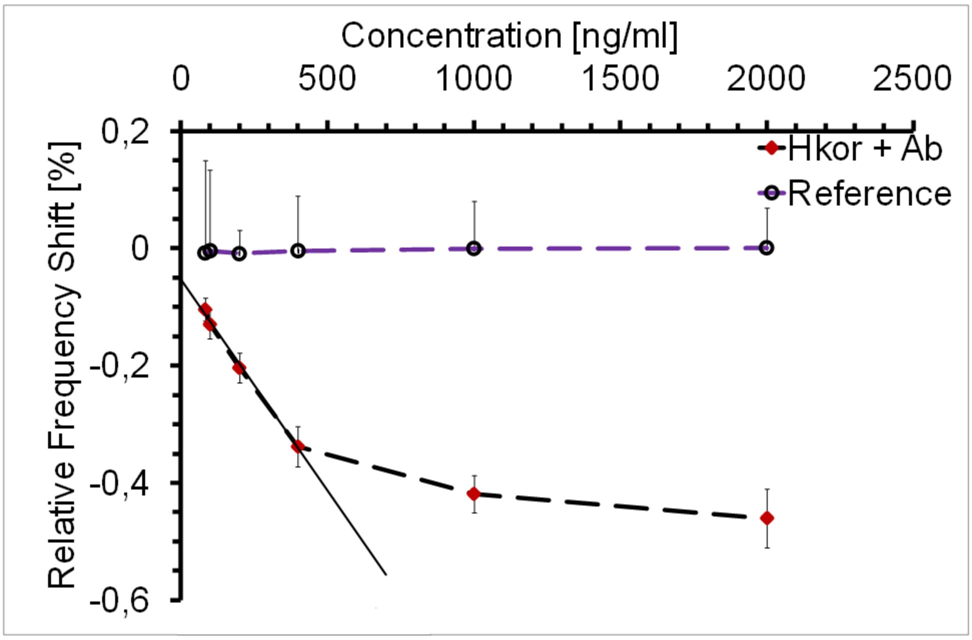

Figure 1.6: Results obtained in the His-tagged hKOR protein and *anti-His* antibody experiment. [39]

In this experiment, the measurements are carried out inside liquid environment with dynamic mode operation. Because no functionalization is carried out for reference chip, no shift in the resonance frequency is observed for the first chip. In the second chip, functionalization is provided between His-tagged hKOR proteins and *anti-His* antibodies, a shift in the resonance frequency is seen. The slope of the curve in Figure 1.6 gives a sensitivity value which is 7 ppm/(ng/mL). The minimum detectable limit in this experiment is 2 Hz. As a result of this, a resolution of 5.7 ng/mL for a 50 kHz-device is obtained [39].

2) Same kind of experiment is performed with Hepatitis molecules. In this experiment, selective binding of Hepatitis A and Hepatitis C molecules is studied. In that manner, two chips are functionalized with Hepatitis A and Hepatitis C antibodies with the help of same linker, DSP. Then, the functionalized cantilevers inside the chips are saturated with Hepatitis antibodies by using Dimethyl Sulfoxide (DMSO) solution.

For negative control samples, Hepatitis C antigen is mixed in bovine serum with increasing concentrations and introduced to the chip containing Hepatitis A antibody. This operation is also repeated for the Hepatitis A antigen and Hepatitis C antibody pair. Finally, each chip is subjected to the correct antigens at increasing concentrations until nearly saturated. The resonance frequency measurements of cantilevers are carried out in different concentrations between 0.04 ng/mL and 100 ng/mL for Hepatitis A samples, and between 0.02 ng/mL and 100 ng/mL for Hepatitis C samples. The results obtained in this experiment can be seen in Figure 1.7.

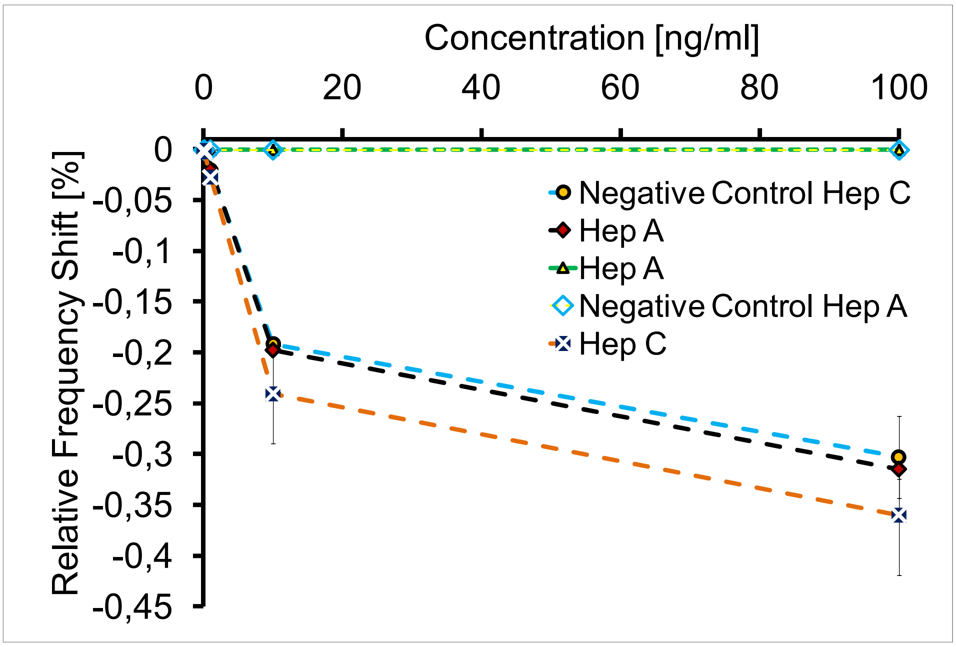

Figure 1.7: Results obtained in Hepatitis A and Hepatitis C experiments.

Also in this experiment, the measurements are carried out inside liquid environment with dynamic mode operation and a resolution of 0.1 ng/mL is obtained.

In previous studies, the resolution limit achieved in the liquid environment was 100 fg/mL for static mode analyses and 1 ng/mL for dynamic mode analyses [13].

1.2. Statement of the Problem

In this thesis, the fabrication flow of a micro-cantilever sensor with a specific design is demonstrated, and the mechanical properties of the materials such as nickel, gold and chromium which are used in the fabrication process of this sensor are demonstrated with the use of resonance technique. In that manner, resonance concept is perceived together with measurement methods and critical factors. Since the sensor will be used as a sensitive device for biological detection experiments, the fabrication process is tried to be developed with a number of improvements in order to provide the effectiveness and trustfulness of these experiments. These improvements include increasing yield for micro-cantilevers and reducing variation from sample to sample.

1.3. Outline

This thesis is composed of 5 chapters.

In the following chapter, the general fabrication flow of a double-layered micro-cantilever which is composed of nickel and gold materials is explained. As one of critical steps in this fabrication flow, electro-plating is investigated with characterization experiments. The effects of changing current density and deposition time on nickel thickness and roughness are studied with these characterization experiments. Furthermore, fabrication flows performed on different wafers such as single-crystalline silicon and silicon-on-insulator (SOI) are demonstrated with comparisons. In addition to this, improvements achieved in some critical steps of this process flow are illustrated.

In the third chapter, mechanical properties of the materials used in the fabrication flow of a biosensor chip such as nickel, gold and chromium are obtained with resonance technique. In that manner, resonance technique is explained with used optical measurement tools and theoretical formulations. At last, a reliability study carried out to investigate the drift of resonance frequency of micro-cantilevers for a 10-month period is demonstrated.

Conclusion chapter summarizes the work done in this thesis and possible future work which can be continued in fabrication of biosensor chips and in investigation of material properties.

Appendix chapter shows the additional work and process developments performed both on familiar and different substrates by using various chemicals and fabrication methods.

Chapter 2 - FABRICATION

In this chapter, the general fabrication flow used during the production of a double-layered nickel-gold cantilever beam with a grating structure at the tip will be illustrated first. Then, one of the important processes in the fabrication flow, which is electro-plating, will be discussed with the parameters that directly affect film quality by using some data obtained with characterization experiments for this process. After that, a new layout will be introduced with the new geometry of cantilevers, gratings, anchors, labeling and alignment marks inside it. In addition to this, the fabrication results with the new layout will be demonstrated both on silicon and silicon-on-insulator (SOI) wafers. Furthermore, the latest developments and improvements by changing some steps in the fabrication flow will be explained with comparisons.

2.1. Fabrication Flow of a Biosensor Chip

Biosensor project is the leading study carried out at Koç University Clean Room Facility. The fabrication flow of this project requires the production of micro-level double-layered nickel-gold cantilever beams for biological sensing applications. In that manner, the fabrication is carried out on a 4"-diameter single-crystalline silicon wafer. The wafer has a <1-0-0> orientation with a thickness and resistivity values of 525±25 μm and 0.1-0.5 Ω·cm, respectively.

Before starting the fabrication, the wafer is cleaned with buffered Hydrofluoric Acid (HF) solution and rinsed with DI water in order to get rid of the oxide remaining on the silicon surface. (Step#1) [For Step definitions, refer to Figure 2.2.] Then, 20 nm-thick chromium and 100 nm-thick gold layers are coated on the silicon surface with RF sputtering method. (Step#2) Here, chromium layer is used to provide adhesion of gold layer [40]. Gold layer is used to utilize the biological mass detection for a functionalized cantilever surface [41]. Additionally, it serves as the plating base.

After that, the wafer is coated with AZ-5214® type positive photoresist inside the spinner machine. The spin parameters are as follows; 3000 rpm for 20 seconds, 5000 rpm for 30 seconds. Immediately after spin-coating, the photoresist-coated wafer is soft-baked on a hot plate at a temperature of 110°C for 10 minutes. During soft-bake process, the wafer is kept covered for preventing the heat loss and effect of light on the photoresist. Soft-bake is needed for the proper sticking of photoresist on the wafer. Then, the wafer is cooled to room temperature. (Step#3)

For photolithography step, the layout introduced in the theses of Hüseyin İlker Ocaklı [16] and Alibey Öztürk [17] is used. Inside mask aligner, the wafer is exposed to UV light whose intensity is 22 mW/cm^2. The exposure time is determined as 15 seconds with contact printing option. After photolithography, wafer is placed inside a developer solution which is composed of 1:4 AZ-351B® type developer:DI water. Development of the patterns on the wafer surface lasts for 10-15 minutes. After the development step, the photoresist thickness is measured with Veeco® DEKTAK 8 Surface Profiler. Here, the thickness of photoresist is found between 1.3-1.6 μm. Once a patterned surface is obtained after photolithography and development steps, the wafer is cut into dice with a diamond-tip pen for the electro-plating of them separately. (Step#4) For photolithography and development steps, a considerable improvement can be achieved; when a different recipe is used. It will be explained in Section 2.4.1.

In the electro-plating step, the chips are coated with nickel inside a nickel sulphamate bath which is composed of 600 g/L nickel sulphamate ($Ni(SO_3NH_2)_2.4H_2O$), 10 g/L nickel chloride ($NiCl_2.6H_2O$) and 40 g/L boric acid (H_3BO_3) [16, 17, 20]. (Step#5) The pH of the nickel sulphamate solution is around 4.5 [16]. During electro-plating, there are many important parameters which affect the quality of electro-plating. The most critical ones among these are applied current and temperature of the solution [27]. These parameters are taken as 40 mA and 45°C. The applied current corresponds to a current density range between 71.456 mA/cm^2 and 97.352 mA/cm^2. The reason for using nickel in the electro-plating process is that nickel provides a corrosion resistance for the devices which are used for biosensor applications. Furthermore, the nickel surface is a suitable environment for providing magnetic actuation [17, 39]. In Figure 2.1, the actual nickel sulphamate bath used in the experiments can be seen with a schematic view.

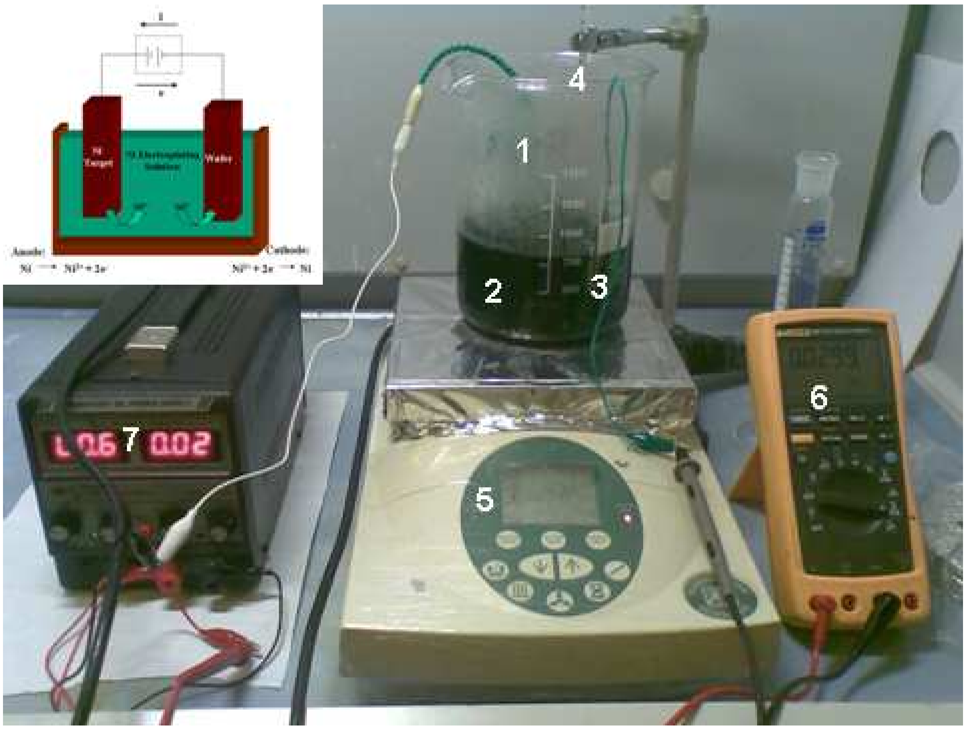

Figure 2.1: Electro-plating process setup: 1) Bio-sensor chip attached with four crocodile cables from four contact places, 2) Nickel Sulphamate solution, 3) Nickel Target Anode, 4) Thermometer for measuring the solution temperature, 5) Magnetic heater for adjusting temperature and stirring solution, 6) Digital Multimeter for monitoring the current, 7) Power Supply for controlling the voltage and current. (The inset shows a schematic view taken from Ref. [42])

At these conditions with an electro-plating time of 10-20 minutes, a nickel thickness in the range of between 0.75-1,5 μm can be achieved. After coating nickel, photoresist is stripped off by using pure AZ-100® type remover chemical. (Step#6)

Hence, nickel patterns on gold surface are obtained. After removing photoresist with remover, the chips are cleaned with DI water carefully.

After this process, wet etching and release of the patterns can be performed. For this purpose, gold surface around the nickel layer is etched by using Transene Inc. GE-8148® type gold etchant. The solution is diluted with DI water with a ratio of 75 % in order to control the etching process. This process takes around 1-2 minutes in that solution. Then, chromium surface underneath the gold surface is etched by using Microchrome Inc. CEP-200® type chromium etchant. This solution is also diluted with DI water with a ratio of 75 % as the gold etchant. This process takes around 30-45 seconds. (Step#7) After removing the gold and chromium layers on the surface, silicon surface is exposed. Silicon is etched with 35 % KOH solution at a temperature of 65°C. After the anisotropic etching of silicon for 30-45 minutes, a depth of 10-15 μm can be obtained. (Step#8) For wet etching of silicon layer, another improvement in the fabrication flow can be achieved; when a different recipe is used. It will be explained in Section 2.4.2.

At the end of wet etching of silicon layer, released and freely standing micro-cantilever beams are fabricated. Here, it is important to check if the cantilevers are completely released. This can be done by using the stylus of Surface Profiler. With the force applied by stylus, the cantilever beam bends downwards if it is released. After anisotropic etching of silicon layer, the remaining chromium layer is also etched by using same chromium etchant which is Microchrome Inc. CEP-200® with same concentration for 90 seconds. (Step#9) The time is kept longer with respect to previous chromium etching process to ensure complete removal of chromium in the absence of any agitation. In Figure 2.2 below, the schematic view of the whole fabrication process for the fabrication of different biosensor chips with additional steps can be seen.

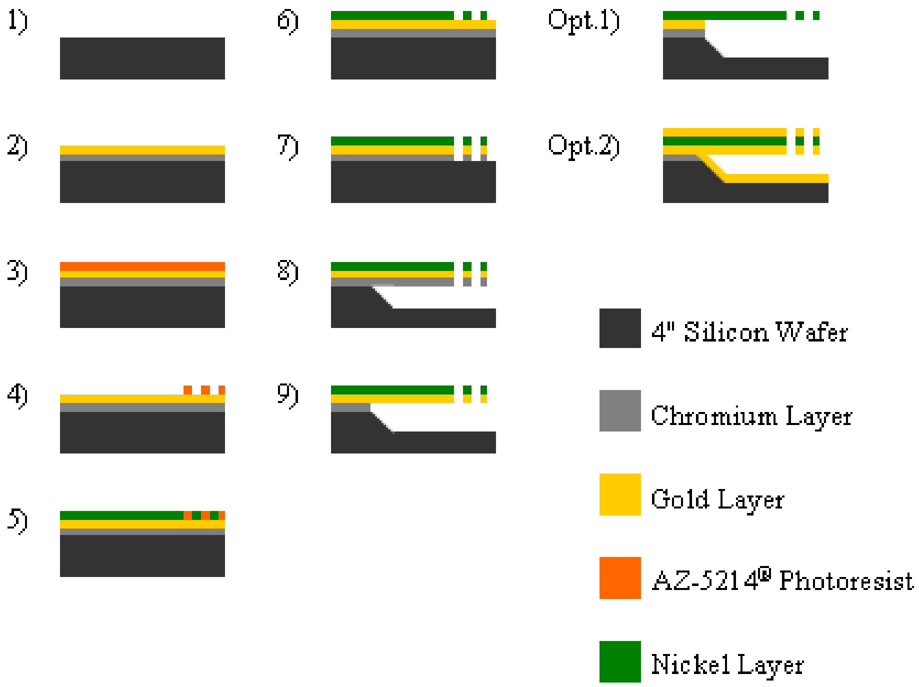

Figure 2.2: Schematic view of the fabrication flow of a Biosensor Chip.

Depending on further requirements, the fabrication flow may continue with some additional steps. In that manner, two optional steps are carried out. In the first optional step, the gold layer underneath the nickel layer is etched by using same gold etchant which is Transene Inc. GE-8148® with same concentration. (Step#Opt.1) Hence, a mono-layered nickel cantilever beam is fabricated. An optimization study on this step can be found in Section 2.4.3. In the second optional step, the gold layer underneath the nickel layer is not etched, but a further gold layer is sputtered onto the nickel layer with a thickness of 100 nm by using RF sputtering method. (Step#Opt.2) At the end, triple-layered sandwich cantilever beam structures where nickel is standing between double gold layers are obtained. In Figure 2.3, an array of double-layered fabricated cantilevers composed of nickel and gold layers can be seen.

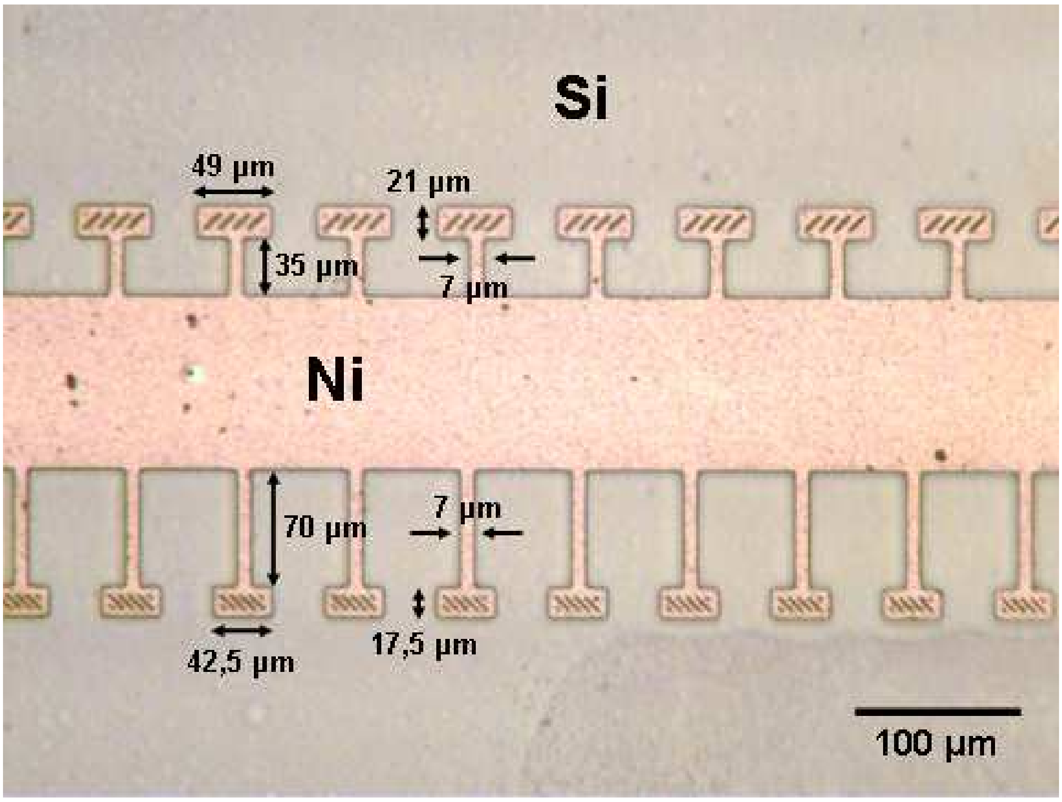

Figure 2.3: An array of fabricated cantilevers with a width of 7 µm.

It can be understood that fabrication flow of a biosensor chip includes many steps with the usage of different chemicals. In Table 2.1, biosensor chip fabrication process can be seen with critical details.

Process No.	**Process Name**	**Process Type**	**Chemical**	**Details**
1	Wafer Cleaning	Cleaning	*Buffered Hydrofluoric Acid (HF)*	(1:10) HF:DI water
2	RF Sputtering	Deposition	-	100 nm gold, 20 nm chromium
3	Spin-coating	Deposition	*AZ-5214®*	$t_{PR} = 1.3\text{-}1.6\ \mu m$
4	Soft-baking	Heating	-	at 110°C for 10 minutes
5	Photo-lithography	Exposure	-	15 seconds
6	Development	Pattern Formation	*AZ-351B®*	80 % diluted solution, 10-15 minutes
7	Electro-plating	Deposition	*Nickel Sulphamate Solution*	40 mA, 45°C, $t_{nickel} = 0.75\text{-}1.5\ \mu m$
8	Removing PR	Cleaning	*AZ-100®*	-
9	Gold Etching	Etching	*Transene Inc. GE-8148®*	75 % diluted solution, 1-2 minutes
10	1st Chromium Etching	Etching	*Microchrome Inc. CEP-200®*	75 % diluted solution, 30-45 seconds
11	Silicon Etching	Etching	*35 % KOH solution*	at 65°C for 30-45 minutes, $depth_{silicon} = 10\text{-}15\ \mu m$
12	2nd Chromium Etching	Etching	*Microchrome Inc. CEP-200®*	75 % diluted solution, 90 seconds

Table 2.1: Biosensor Chip Fabrication Process.

2.2. Electro-plating Curves

As it was mentioned in Section 2.1, electro-plating is one of the most important steps in the fabrication process of the biosensor chip. As a result of being a relatively simple and inexpensive technology, electro-plating is one of the most commonly used techniques in the MEMS field [27]. While being simple, this step should also be carefully analyzed in order to have highly uniform and smooth nickel surfaces on the chip. The smoothness and the quality of nickel surface is an important factor for the proper reflection of laser light onto the photodiode in a Laser-Photodiode (PD) mechanism for measuring the resonance frequency of a cantilever beam [39, 43]. In previous studies, factors affect the quality of electro-plating such as time, current density and temperature were studied. Figure 2.4 summarizes these studies in the literature.

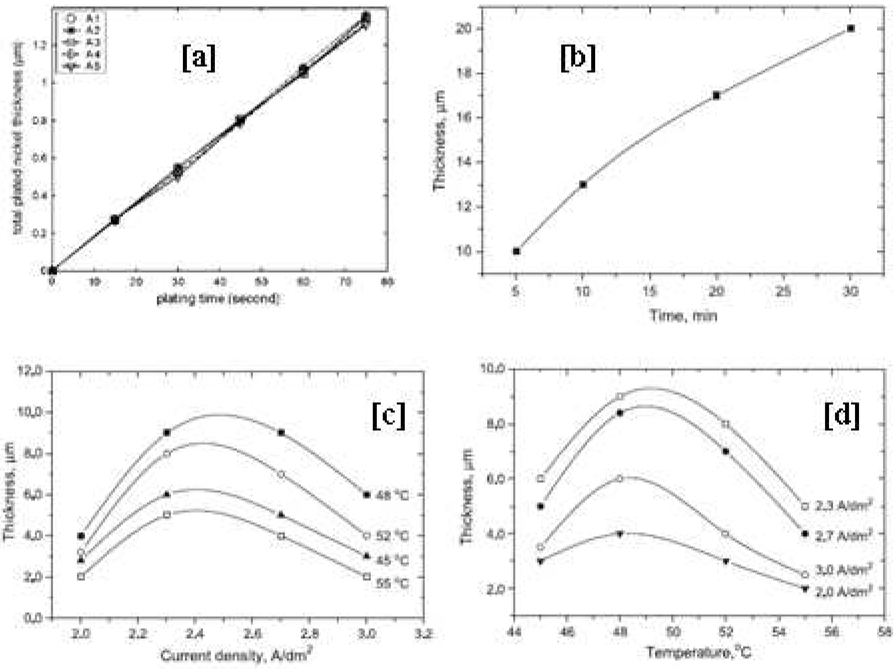

Figure 2.4: Temperature, current density and time effects to the electro-plating process: a) Nickel thickness vs. time graph (short term), b) Nickel thickness vs. time graph (long term), c) Nickel thickness vs. current density graph obtained after 5-minute deposition for different temperatures, d) Nickel thickness vs. temperature graph obtained after 5-minute deposition for different current densities. [23, 44]

As expected, deposited nickel thickness increases with increasing electro-plating time. This relationship is linear in short term (seconds); but as the electro-plating time increases to the order of minutes and hours, the relationship turns to a logarithmic behavior. Furthermore, maximum nickel thickness is obtained at a temperature around 48-49°C and at a current density between 2.3-2.7 A/dm^2 (23-27 mA/cm^2) after 5-minute deposition time for a specific deposition bath.

Previous studies which were performed about electro-plating were important sources for understanding this concept. In addition to these studies, two similar experiments are carried out in order to see the quality of used electro-plating bath.

In these experiments regarding the electro-plating process, the parameters which directly affect the quality of electro-plating are investigated. At the beginning of this section, these parameters are mentioned as current density, electro-plating time and temperature. In that manner, two different chips are prepared for two different characterization experiments. By using the first chip, the effect of changing current density to the thickness and roughness of the nickel surface is examined for constant time and temperature of the nickel sulphamate solution in the first characterization experiment. Hence, nine chips including 7 μm-width double-clamped cantilevers are electro-plated at 45°C with applied currents of 10, 15, 20, 25, 30, 35, 40, 45 and 50 mA for 20 minutes. The actual size of a chip is 1 cm^2 (100 mm^2), but from the Layout Editor program (L-edit) the electro-plated area on used chip is found as 68.21 mm^2. When the applied current is divided by this quantity, the current densities used in this experiment can be computed as 14.661, 21.992, 29.332, 36.653, 43.983, 51.314, 58.645, 65.975 and 73.306 mA/cm^2, respectively. Furthermore, the distance between the anode and cathode is kept constant at 8 ± 0.5 cm. As a result of this experiment, some graphs are obtained for showing the effects of current to nickel surface roughness and thickness. These graphs can be seen as in Figures 2.5, 2.6, 2.7 and 2.8 below.

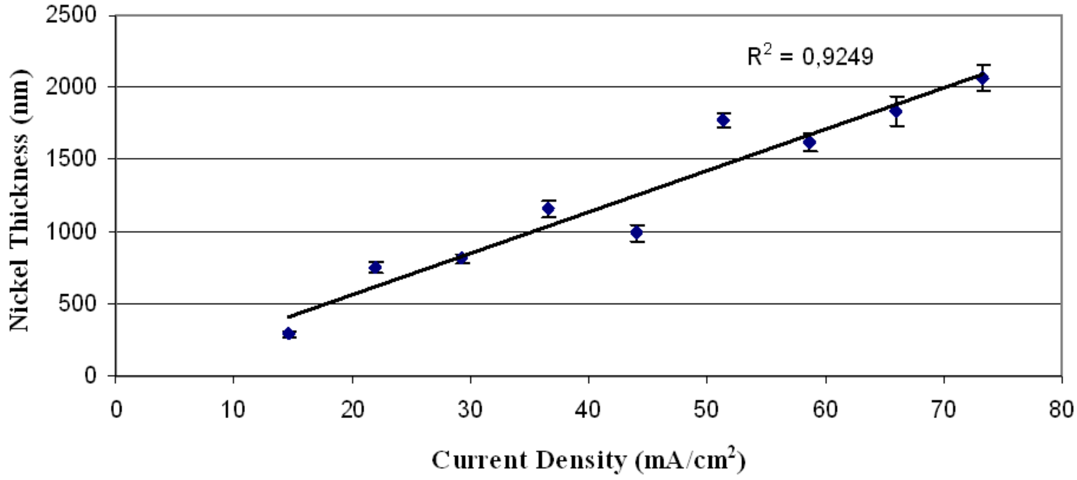

Figure 2.5: Nickel thickness vs. current density. (Constant time: 20 minutes, Constant temperature: 45°C)

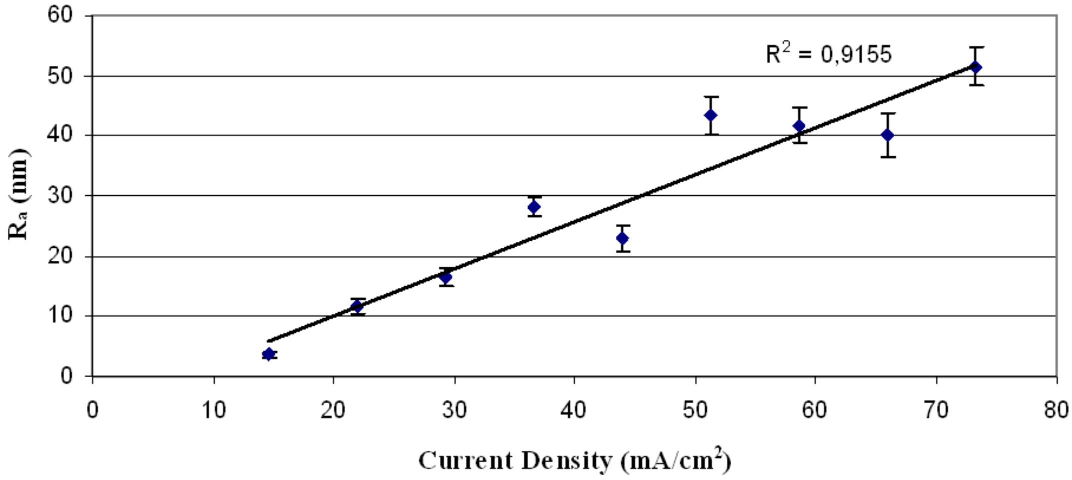

Figure 2.6: R_a (Arithmetic Average Surface Roughness) vs. current density. (Constant time: 20 minutes, Constant temperature: 45°C)

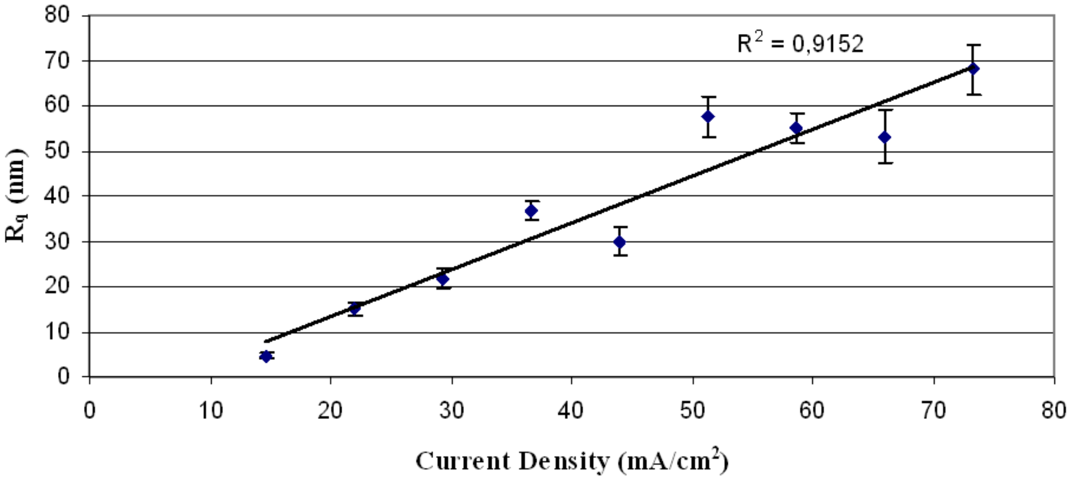

Figure 2.7: R_q (Root Mean Squared Surface Roughness) vs. current density. (Constant time: 20 minutes, Constant temperature: 45°C)

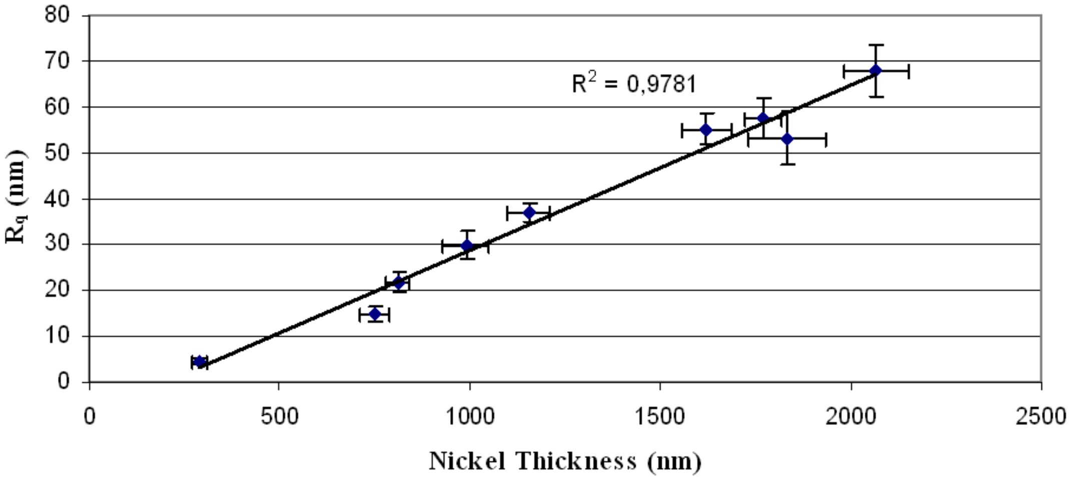

Figure 2.8: R_q (Root Mean Squared Surface Roughness) vs. nickel thickness. (Constant time: 20 minutes, Constant temperature: 45°C)

It can easily be seen Figures 2.5, 2.6, 2.7 and 2.8 that as the applied current increases, both the nickel thickness and the surface roughness increase. In the graphs, surface roughness is obtained by using two parameters which are Arithmetic Average surface roughness (R_a) and Root Mean Squared surface roughness (R_q). In Figures 2.9 and 2.10, the definitions of these parameters can be seen more clearly.

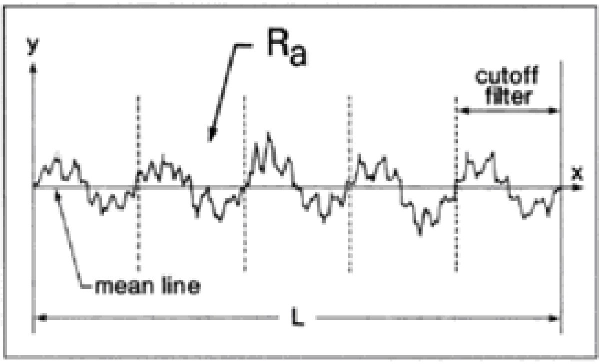

Figure 2.9: The definition of Arithmetic Average surface roughness (R_a). [45]

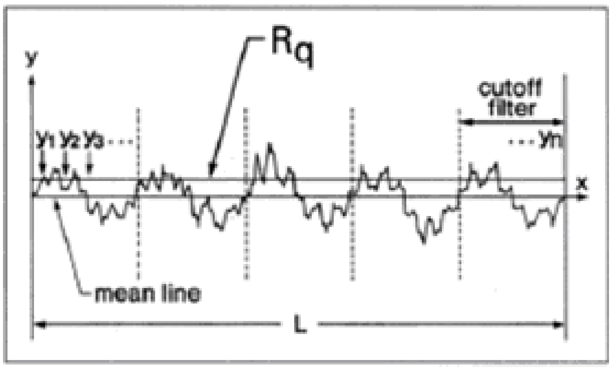

Figure 2.10: The definition of Root Mean Squared surface roughness (R_q). [45]

These parameters give the roughness for a specific surface (L) and can be computed by using Eqn. 2.1 and Eqn. 2.2 [45].

$$R_a = \frac{1}{L}\int_{x=0}^{x=L} |y|\,dx \qquad \text{(Eqn. 2.1)}$$

$$R_q = \sqrt{\frac{1}{L}\int_0^L y^2(x)dx} \qquad \text{(Eqn. 2.2)}$$

In the second characterization experiment, the effect of changing time to the thickness and roughness of the nickel surface is examined for constant current density and temperature of the nickel sulphamate solution. By using the data obtained in the first experiment, 10 mA current (14.661 mA/cm^2 current density) is selected as the available current. The reason for choosing this current density is that minimum surface roughness is obtained at this current density for 20-minute deposition time. Hence, four chips including 8 µm-width double-clamped cantilevers are electro-plated at 45°C with an applied current of 10 mA for 5, 30, 60 and 120 minutes. As in the first characterization experiment, the distance between anode and cathode is again kept constant at 8 ± 0.5 cm for this experiment. Moreover, the electro-plated area on used chip is found as 66.94 mm^2 from L-Edit program. In order to be consistent for the current density with the first experiment, the applied current is stabilized around 9.5-10 mA for this experiment. The obtained results in this experiment can be seen as in Figures 2.11, 2.12, 2.13 and 2.14 below.

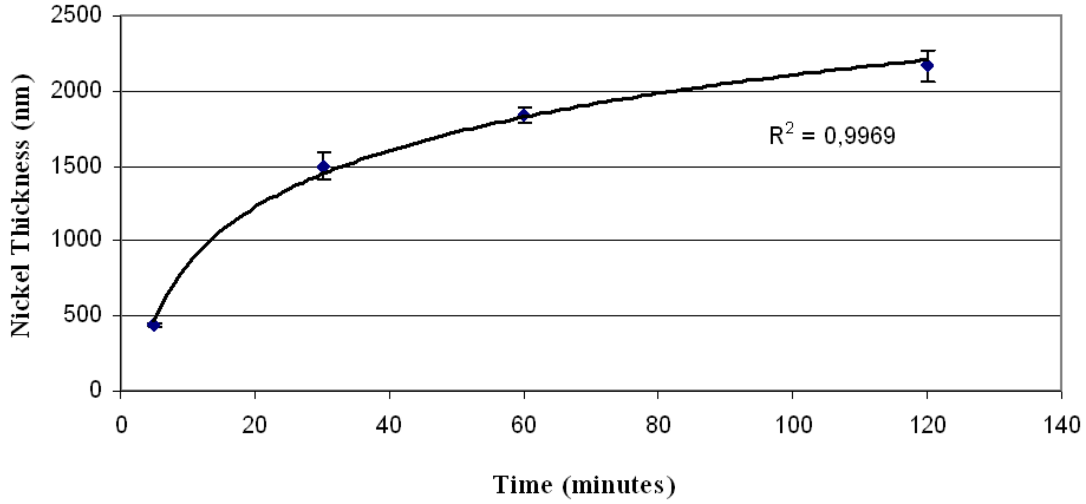

Figure 2.11: Nickel Thickness vs. time. (Constant current density: 14.661 mA/cm^2, Constant temperature: 45°C)

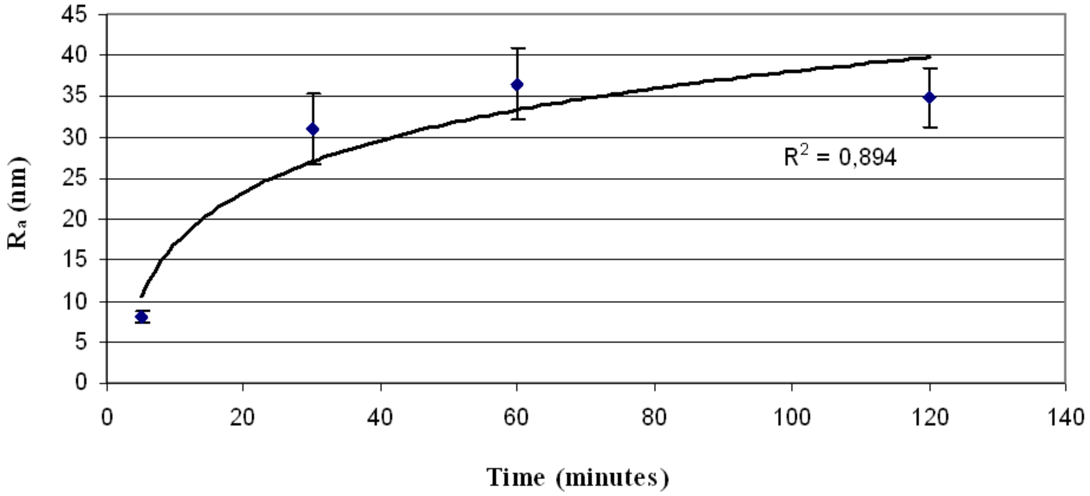

Figure 2.12: R_a (Arithmetic Average Surface Roughness) vs. time. (Constant current density: 14.661 mA/cm^2, Constant temperature: 45°C)

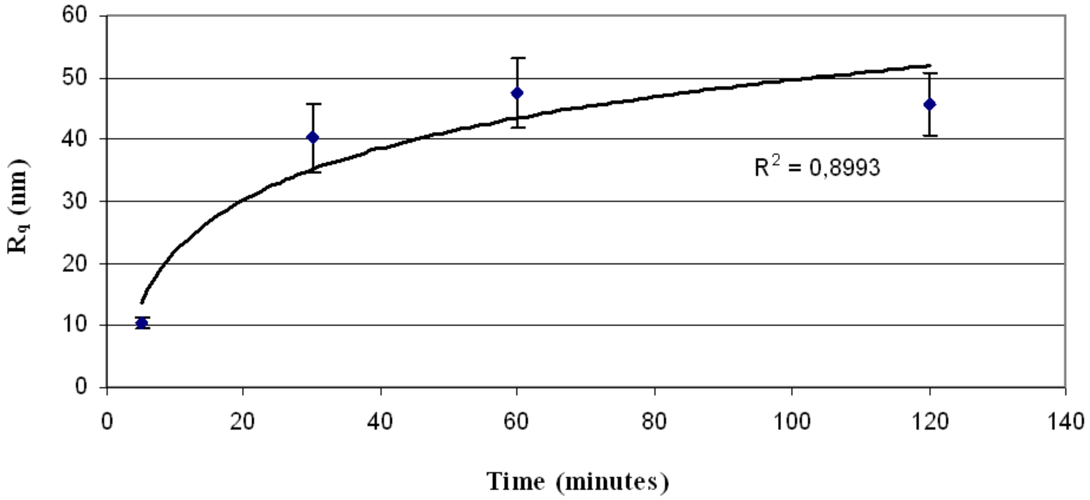

Figure 2.13: R_q (Root Mean Squared Surface Roughness) vs. time. (Constant current density: 14.661 mA/cm^2, Constant temperature: 45°C)

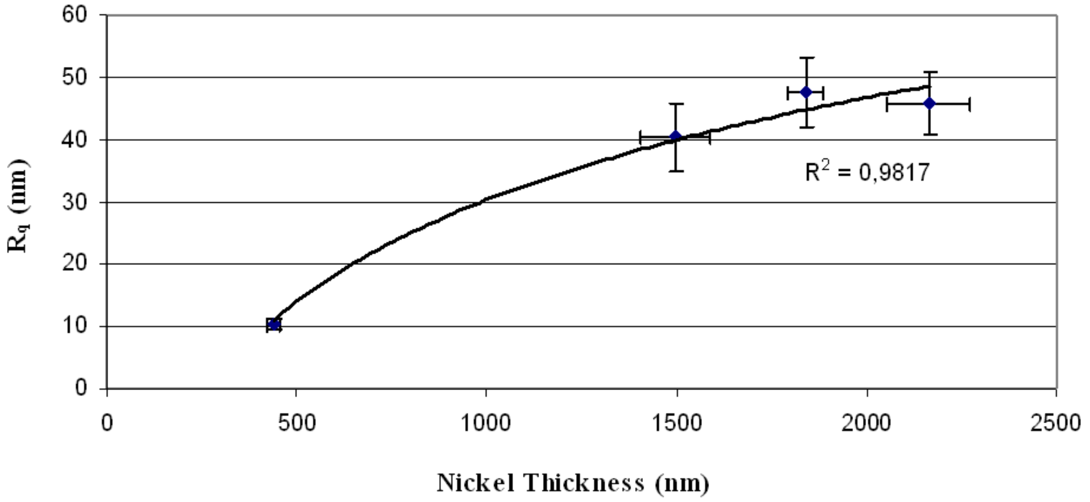

Figure 2.14: R_q (Root Mean Squared Surface Roughness) vs. nickel thickness. (Constant current density: 14.661 mA/cm^2, Constant temperature: 45 °C)

It is evident that as the electro-plating time increases, both the nickel thickness and the surface roughness increase again. Furthermore, the rate of increment for the nickel thickness slows down with increasing time. This fact supports the relationship between nickel thickness and electro-plating time which is linear at the beginning but later turns into logarithmic [23, 44]. Moreover, the surface roughness stabilizes after some time in spite of the increasing electro-plating time. The roughness value converges to 35 nm for R_a and 45 nm for R_q.

As a result of electro-plating characterization experiments, it is concluded that there is a linear relationship between nickel thickness and surface roughness for a specific current density range between 15 mA/cm^2 and 75 mA/cm^2. But in order to verify this conclusion strongly, a third experiment is conducted. In this characterization experiment, four chips are prepared and electro-plated with current densities of 10 mA/cm^2, 30 mA/cm^2, 50 mA/cm^2 and 70 mA/cm^2 until they reach the same nickel thickness. The electro-plated area of the chip used in this experiment is 36.62 mm^2, so the chips are electro-plated with 3.66, 11, 18.31 and 25.63 mA current values. Once the required nickel thickness is obtained, the surface roughness values for different current densities are compared. As previous characterization experiments, this experiment is also carried out inside a nickel sulphamate solution whose temperature is 45°C. Similarly, the distance between anode and cathode is kept constant at 8 ± 0.5 cm. As a result of this experiment, Figures 2.15 and 2.16 are achieved.

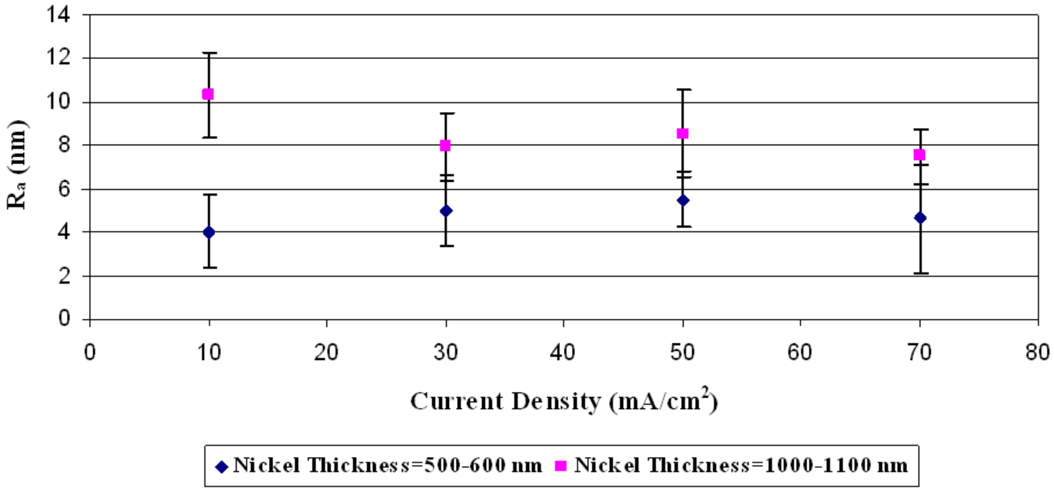

Figure 2.15: R_a (Arithmetic Average Surface Roughness) vs. current density.

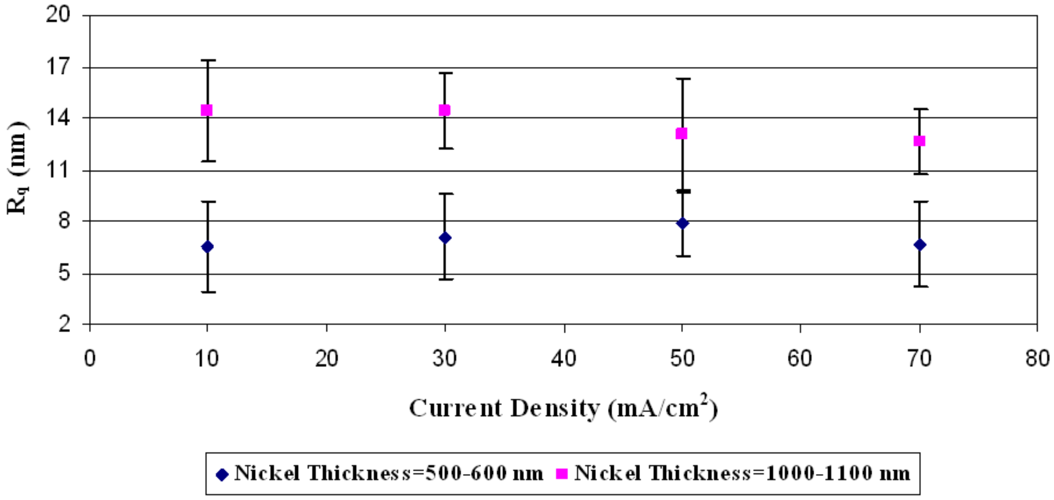

Figure 2.16: R_q (Root Mean Squared Surface Roughness) vs. current density.

The experiment is performed for two different nickel thicknesses which are 500-600 nm and 1000-1100 nm, and it is seen that the surface roughness is almost stable for a current density range between 10 mA/cm^2 and 70 mA/cm^2. At the end, it is concluded that the effect of current density to surface roughness is not as dominant as the effect of nickel thickness. There is a specific roughness range for a specific nickel thickness.

This range is around 10-20 nm for 1000 nm nickel thickness in the proposed deposition solution.

After this experiment, the deflection on the cantilevers is viewed by using a Mirau Objective Microscope. As a result of the residual stress accumulation, the cantilevers deflect downwards. In that manner, it is aimed to compute the surface stress on the cantilevers due to bending by using Equation 1.1. However, there is a problem about the usage of this equation for this purpose. Since the cantilevers are mono-layered nickel cantilevers and these cantilevers are not functionalized with any biological substance, this equation can not be used for stress calculation. Furthermore in previous studies [16, 25, 28], electro-plating process was carried out with nickel and gold materials, and bending was seen on cantilevers both towards upward and downward directions. This formulation also does not explain this difference either. Therefore it is believed that it will be enough to present only the deflection data. The deflection data for deflected cantilevers with and without grating parts can be seen in Figures 2.17 and 2.18.

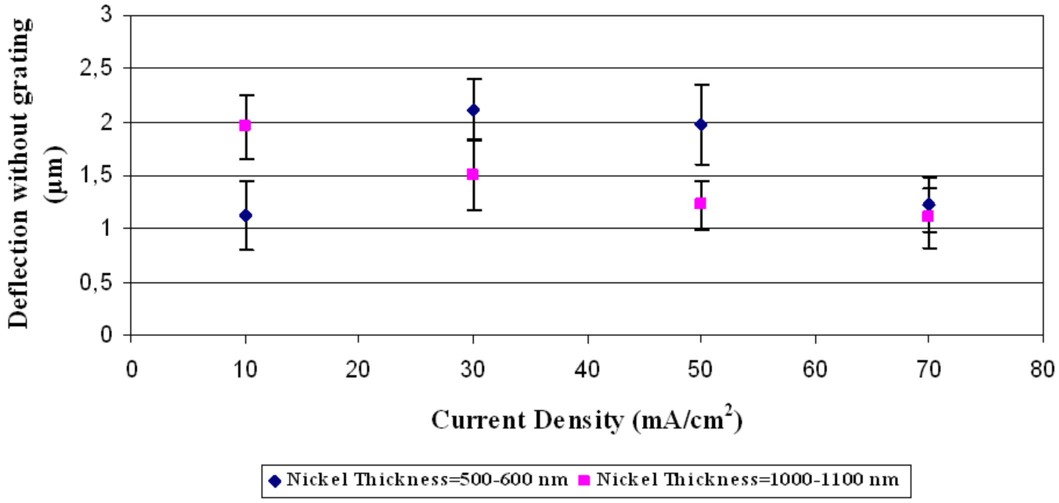

Figure 2.17: Deflection data for cantilevers without gratings.

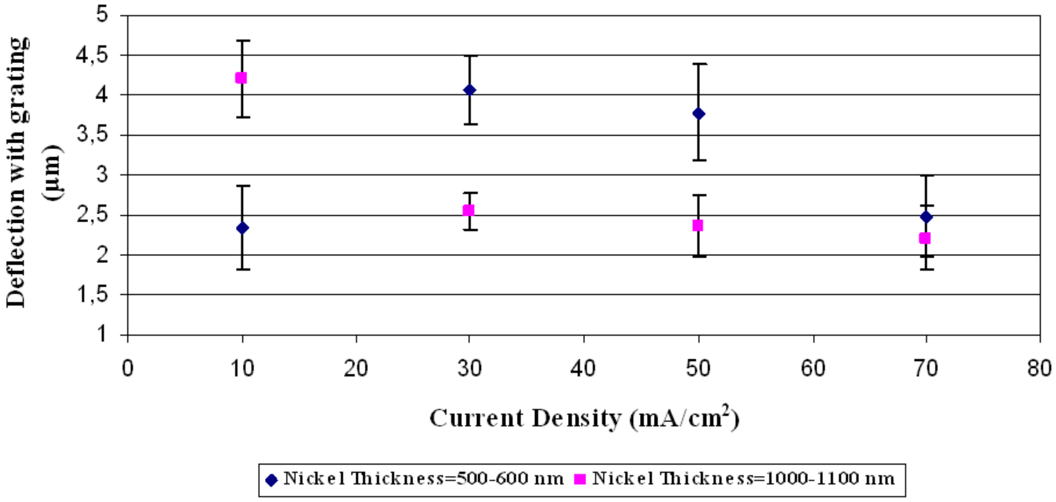

Figure 2.18: Deflection data for cantilevers with gratings.

In Figures 2.17 and 2.18, it can be seen that the amount of deflection is 1-2 µm for cantilevers without grating parts and is 2-4 µm for cantilevers with grating parts. The top views of the deflected cantilevers with fringes can be seen in Figure 2.19.

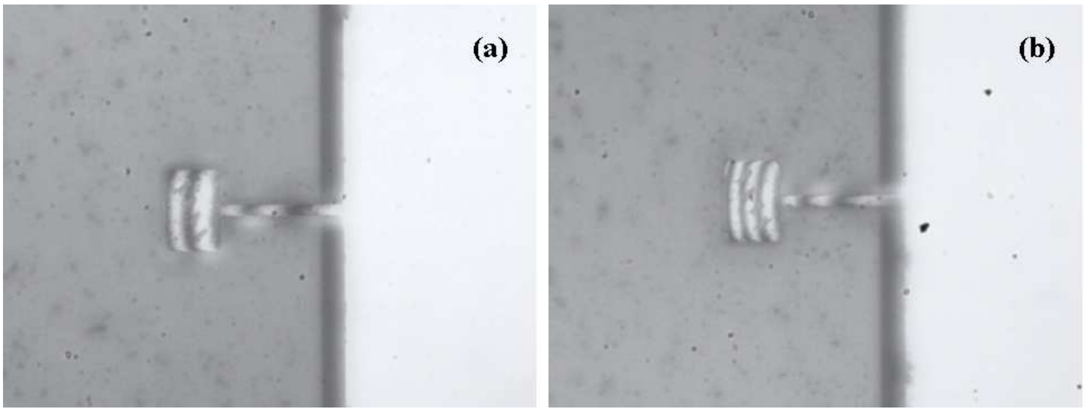

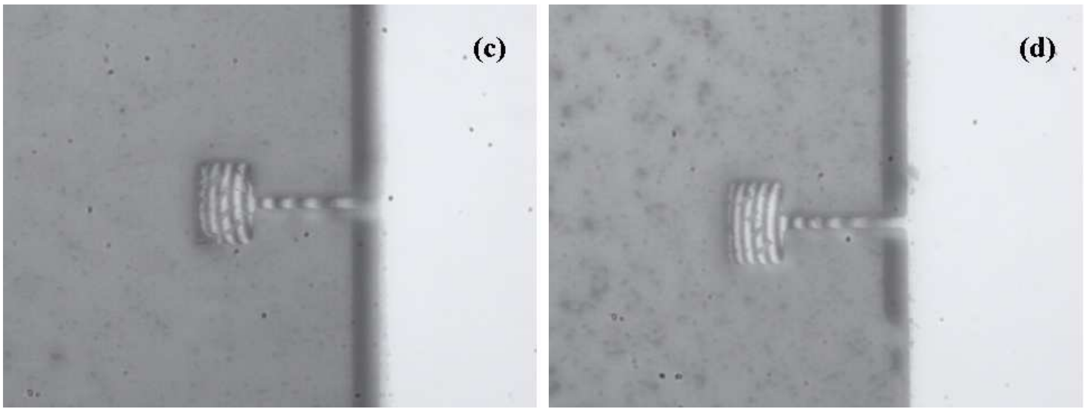

Figure 2.19: Top views of the deflected cantilevers with fringes. (Cantilever dimensions are 4 µm in width and 49 µm in length.)

2.3. 2nd Generation Layout

In this new layout, one mask is the nickel mask which has no difference with the previous biosensor mask, and the second mask is the gold mask which is used as producing the functionalization layer on the cantilever beams. Passing to two mask process changes the placement of functionalization layer. Gold layer is used as the functionalization layer as in the previous process; but instead of being under the nickel layer, this time it is planned to be on the nickel layer. Moreover, the functionalization can be done either on the grating part and beam together, or on the grating part itself.

The masks are designed for a 4" wafer, and are divided into 40 chips with areas of 1 cm^2. The cantilevers on the chips are aligned 0° with the boundaries of the chips, except for the double-clamped cantilevers which are aligned 45° with the boundaries of the chips. The width of cantilevers is kept constant at 4 µm, except some specific cantilevers. There are two different cantilever types on the masks which are static and dynamic cantilevers. Static cantilevers have geometry of either 500 µm length and 100 µm width, or 400 µm length and 75 µm width with specific comb finger designs attached to specific places. The dynamic cantilevers have two major types which are single-clamped or double-clamped. These cantilevers have grating structures at their tips for single-clamped cantilevers and at their centers for double-clamped cantilevers. The geometry of gratings are 21 µm x 21 µm, 21 µm x 31 µm and 21 µm x 36 µm in width and in length. Furthermore, the cantilevers are positioned until same line vertically by changing the structure of anchor. Hence, the change in cantilever length can be achieved after this operation. In addition to these types of cantilevers, there are also cantilevers which are designed as tuning forks. These cantilevers are also single-clamped cantilevers with two separate gratings having geometry of 21 µm x 21 µm.

The chips have four contact places at their corners for making contact during electro-plating process. Furthermore, the vertical and horizontal distances between the chips are 1500 µm and 2000 µm, respectively. These distances are suitable while cutting the wafer into dice with a diamond-tip pen. In Figures 2.20 and 2.21, the designs of the nickel mask and gold mask can be seen.

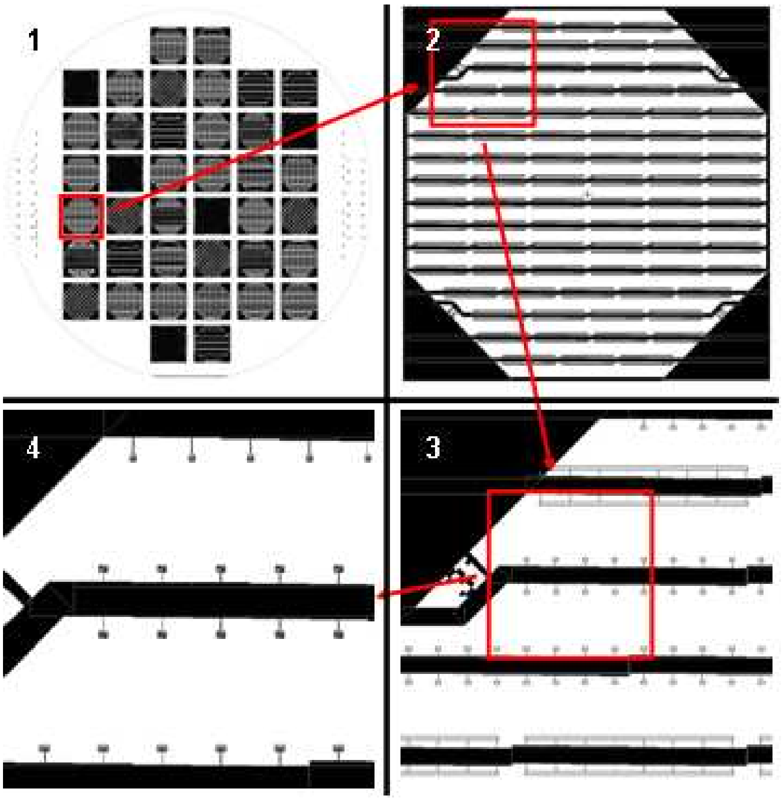

Figure 2.20: Nickel Mask Design: 1) 4" wafer with chips, 2) One single chip with contact places at each corner, 3) Cantilevers clamped to both sides of anchors, 4) Cantilevers with different gratings at the tips.

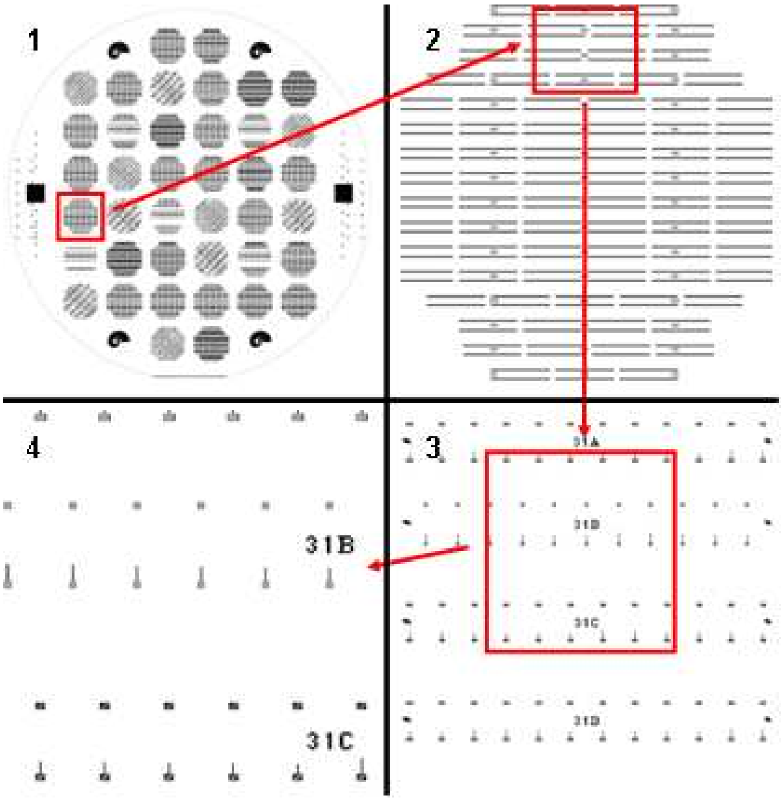

Figure 2.21: Gold (Functionalization) Mask Design: 1) 4" wafer with chips, 2) One single chip, 3) Differently functionalized cantilevers with labels between, 4) Differently functionalized cantilevers with labels between (Closer view).

2.3.1. Fabrication on Silicon Wafer

Working with 2nd Generation Layout requires some changes in the usual fabrication process. In that manner, lithography and development process in the fabrication flow is changed in order to obtain better patterns and to work with more critical dimensions. This improvement can be seen in Section 2.4.1.

Furthermore as a result of including a two-mask photolithography process, the whole wafer shouldn't be cut into dices before finishing the both photolithography steps. In that manner, after finishing the first photolithography process with the nickel mask, the wafer is thought to be coated with nickel by using the RF Sputtering method at first. The reason for this fact is to increase the smoothness of the coated nickel layer with this method which is relatively much more difficult to obtain by using electro-plating method. However, RF Sputtering method is not successful as a result of having problems with the nickel target magnetron. In the literature, this problem is defined as the low magnetic flux intensity caused with the sputtering of ferromagnetic materials such as nickel or cobalt. As a result of the low magnetic flux intensity in front of the target material on the magnetron, the plasma can not be ignited inside the vacuum chamber at low gas pressures and the target can not be sputtered. So, the conventional magnetron sputtering requires the usage of target materials whose thicknesses are smaller than 1.5 mm [46, 47]. Another way can be to increase the gas pressure during sputtering to ignite the plasma, but this may be dangerous for the device. Hence, electro-plating remains as the only option for the coating the whole wafer with nickel layer.

Since electro-plating process has not been tried before with a 4" wafer, it is decided that it will be more reasonable to start with a quarter of the 4" wafer first. Therefore as the first photolithography process is performed with the nickel mask, the wafer is cut into four parts with 10 chips per one part. Then, a new nickel sulphamate solution is prepared with same ratios of nickel sulphamate, nickel chloride and boric acid as stated at the beginning of this chapter. The quarter wafer is attached to the teeth of the four crocodile cables from available contact places, and electro-plating is performed with a current and temperature of 65 mA and 45°C. The process takes 15 minutes and, a nickel thickness of 1-1.5 µm is obtained. When the thickness of nickel is measured with Veeco® DEKTAK 8 Surface Profiler on different places of the wafer, it is seen that the variation in the thickness between the chips is not too much. Therefore, it will not be needed to establish a contact from the four corners of the chip for homogeneity during electro-plating process as stated in *Timurdogan et al* [39]. In conclusion, nickel coating of the quarter wafer with electro-plating method is performed for the first time at this clean room facility, and the results are pretty good. In Figure 2.22, the electro-plated quarter wafer can be seen.

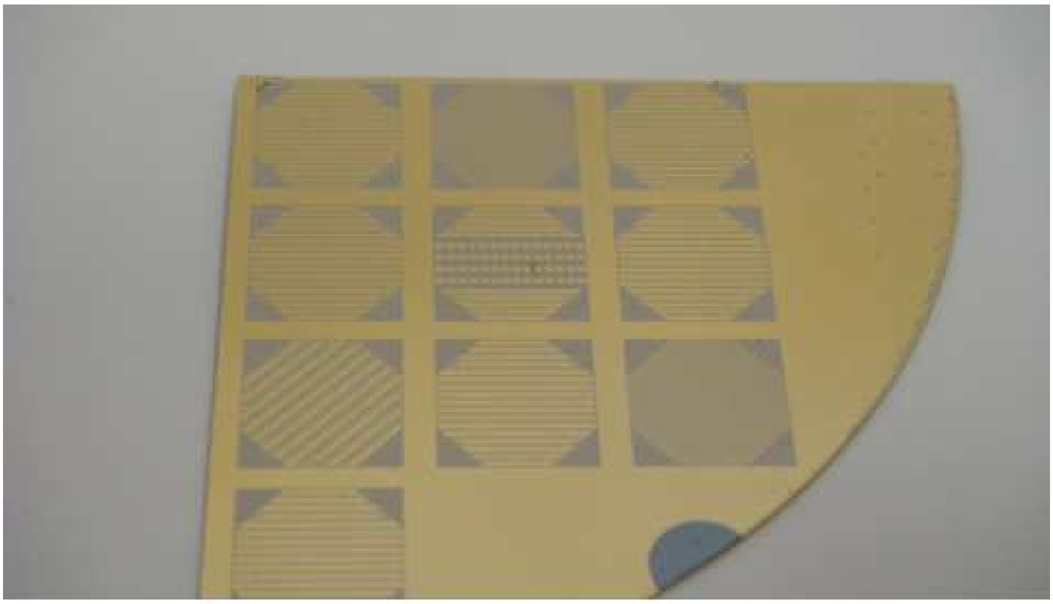

Figure 2.22: Electro-plated quarter wafer.

With the electro-plating of the quarter wafer, another major development is obtained about the attachment of the crocodile cables on the wafer. In the previous fabrication processes, the teeth of the crocodile cables harshly damage the contact places of the chips. These damages can lead to the being loosen of the nickel layer during fabrication. Therefore the crocodiles are covered with aluminum foil in order to decrease the severe effects of this problem [20]. However in spite of covering with aluminum foil, some damages still can occur on the corners of the chip and this can ruin the whole fabrication process. After passing to the process of electro-plating of the quarter wafer, the problem caused with the crocodiles is decreased because of not attaching the crocodiles from every corner of the chips. With the new method, four crocodile cables are still being used; however, instead of establishing contacts from every corner of each chip, only remote corners of the wafer is attached with the crocodiles. Hence, many chips on the wafer will be coated with nickel without being attached with the teeth of the crocodile cables. In Figure 2.23, the solved problem can be seen more clearly.

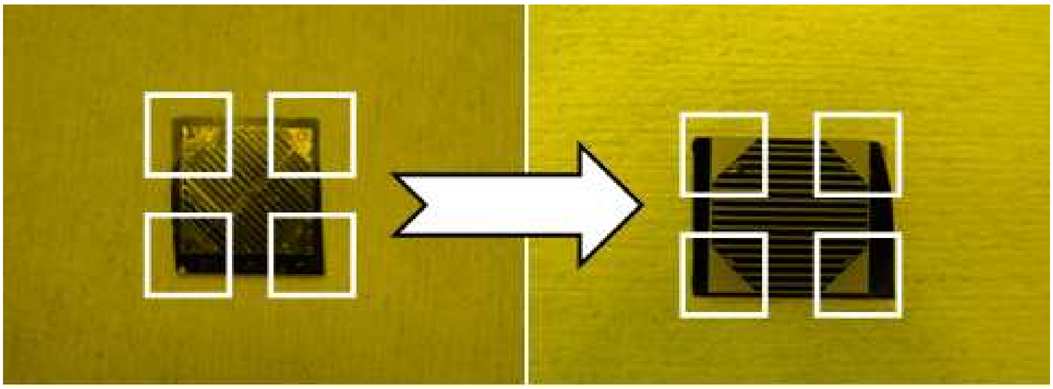

Figure 2.23: Better contact places on the corners of the chips obtained with electro-plating of the quarter wafer.

Once the quarter wafer is fully electro-plated, the process continues with the etching of gold and chromium layers on the quarter wafer. Without changing the concentrations of gold and chromium etchants used in the previous fabrication process, the wet etching process is performed by increasing the time for each etching process. In Figure 2.24, the quarter wafer whose gold and chromium layers are etched and which is ready for anisotropic silicon etching can be seen.

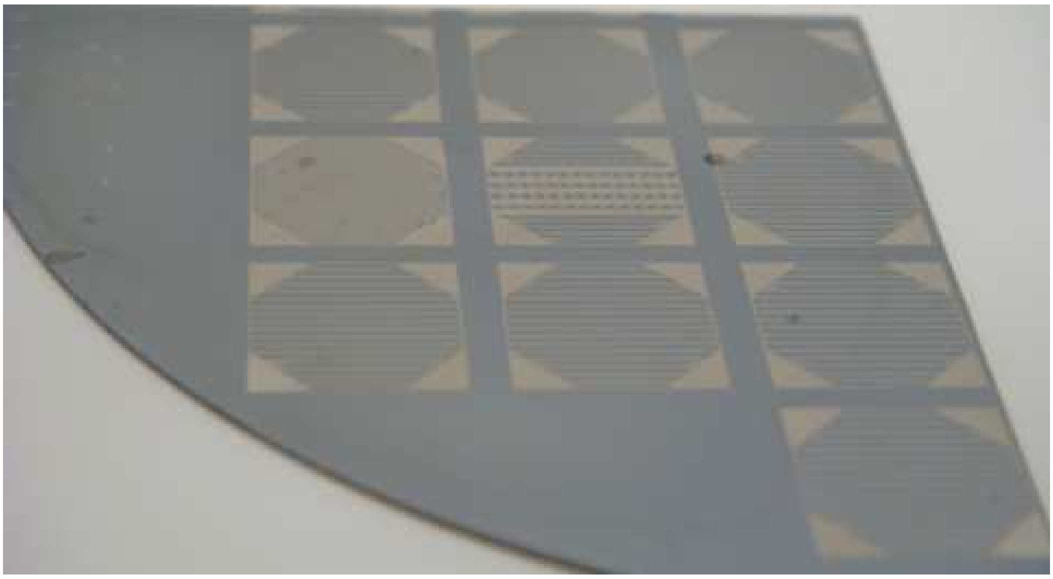

Figure 2.24: Gold and chromium layers etched quarter wafer.

After that, the silicon etching of quarter wafer inside the KOH solution is carried out chip by chip. At the beginning, it was tried to continue working on the quarter wafer with the silicon etching. But, it was seen that it would be difficult to obtain successful samples at the end of this step. Hence, the wafer is cut into dice before proceeding to KOH etch, and the silicon etching procedure takes place separately chip by chip. As a result of this, some successful samples are obtained as shown in Figure 2.25.

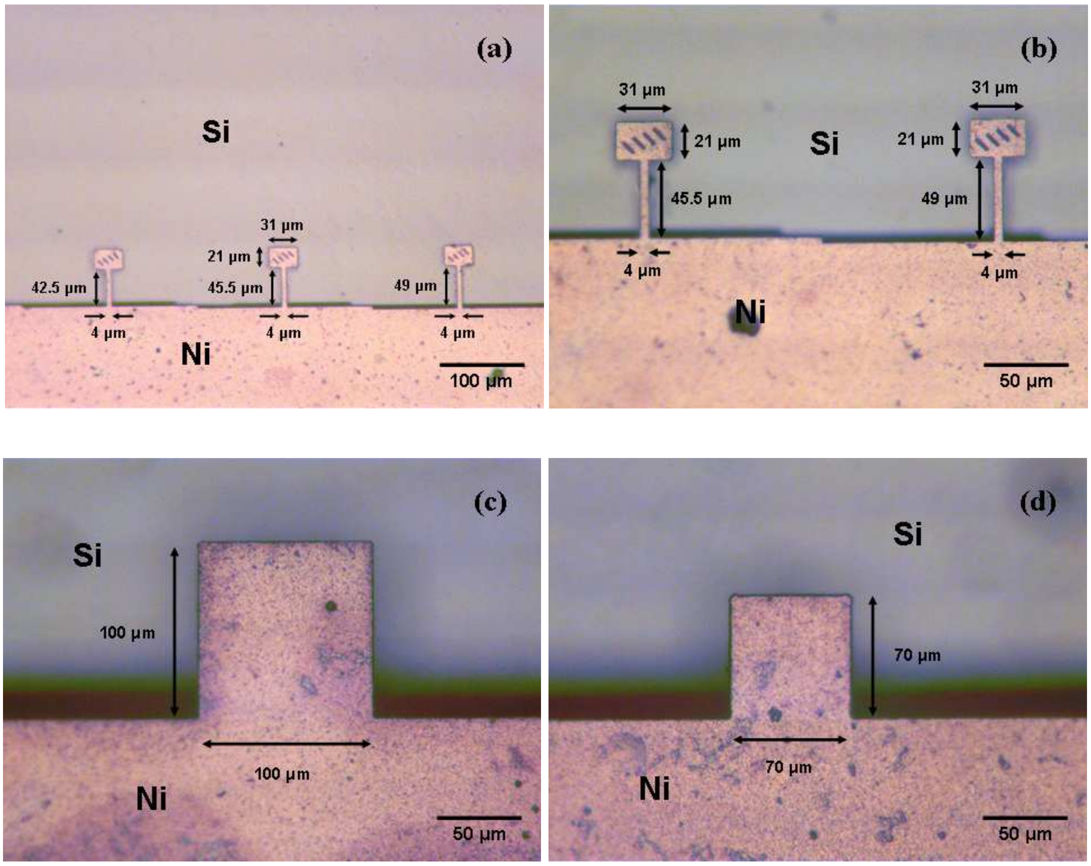

Figure 2.25: One-end-fixed cantilevers fabricated with 2nd Generation Layout on silicon wafer. a) cantilevers with 21 µm x 31 µm and 45° aligned gratings (10x magnification), b) cantilevers with 21 µm x 31 µm and 45° aligned gratings (20x magnification), c) cantilevers with 100 µm x 100 µm geometry (20x magnification), d) cantilevers with 70 µm x 70 µm geometry (20x magnification).

In Figure 2.25(c) and 2.25(d), because of having a larger geometry with respect to the usual cantilevers, it would be an obligation to increase the anisotropic silicon etching time in order to provide the releasing operation of the cantilevers. But, this fact does not affect the working of cantilevers. It should also be noted that the cantilevers are checked if they are completely released by using the stylus of Surface Profiler.

2.3.2. Fabrication on Silicon-on-Insulator (SOI) Wafer

After completing the fabrication successfully on silicon wafer, a new fabrication process is carried out with SOI wafer. SOI wafer has a relatively different structure with respect to the typical silicon wafer. The dimensions of the used SOI wafer are almost same as a silicon wafer with diameter and thickness values of 100±0.1 mm and 500±10 µm, respectively. Furthermore, the SOI wafer has a <1-0-0> orientation as the silicon wafer. However instead of including only a silicon layer, SOI wafer also has an oxide layer additionally. Also because of having different layers, SOI wafer has different resistivity values. The resistivity of oxide layer is between 0.001-0.002 Ω·cm, where the resistivity of the whole device is between 1-10 Ω·cm. In Figure 2.26, the schematic view of the SOI wafer can be seen.

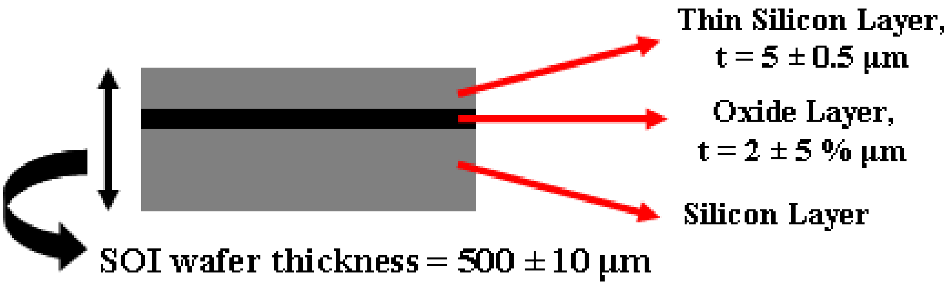

Figure 2.26: The schematic view of an SOI wafer.

The fabrication process on the SOI wafer starts with RF sputtering of the gold and chromium layers, spin-coating of AZ-5214® type photoresist and soft-baking steps without changing any parameters within the silicon wafer fabrication. For photolithography and development processes, same solution with same concentrations (80 % diluted AZ-351B® solution) is used; however, the some parameters change as it will be explained in Section 2.4.1. For the nickel electro-plating step, the full wafer is separated into four pieces as it was done for silicon wafer fabrication. Then, the quarter wafer is electro-plated inside same nickel sulphamate solution with 45°C and 10 mA temperature and current values. Current is kept same with the value found in the first characterization experiment. Electro-plating lasts for 45 minutes. As a result of this, a nickel thickness range between 850 and 1050 nm is obtained for micro-cantilevers. The obtained nickel surface roughness changes between 20 nm and 30 nm. After electro-plating process, photoresist is stripped off by using pure AZ-100® type remover, and chip is washed with DI water.

Then, the etching process is carried out with gold and chromium etching steps in same conditions (75 % diluted Transene Inc. GE-8148® for 1-2 minutes for gold etching, 75 % diluted Microchrome Inc. CEP-200® for 30-45 seconds for chromium etching). After that, silicon etching is performed inside 35 % KOH solution with 60°C temperature. Because of having a silicon layer thickness, which is 5±0.5 μm, etching takes a relatively shorter time. After 15-20 minutes, etching stops automatically because of reaching the oxide layer. Due to the specific orientation of the cantilevers employed in this layout, etching of cantilever does not lead to any undercut. Then, the chromium layer underneath the cantilevers is etched in same conditions with silicon wafer fabrication (75 % diluted Microchrome Inc. CEP-200® for 90 seconds). In Figure 2.27, different types of fabricated cantilevers can be seen.

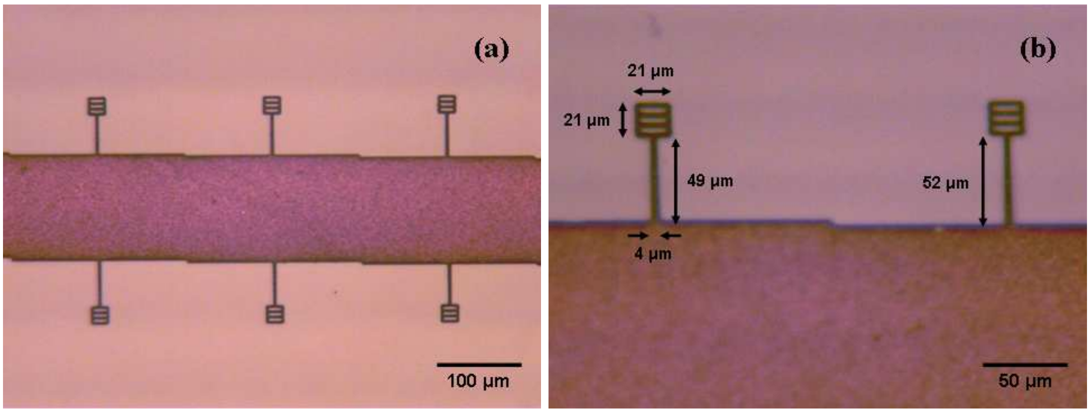

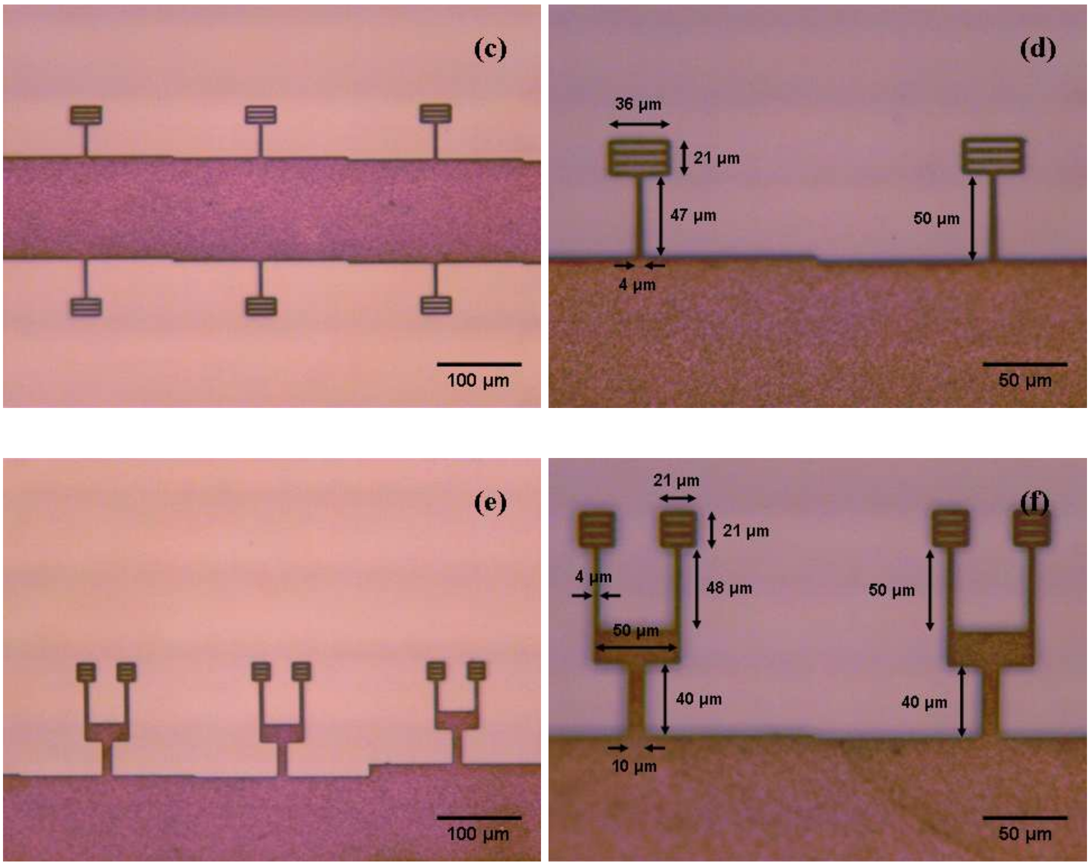

Figure 2.27: Cantilevers fabricated with 2nd Generation Layout on SOI wafer. a) One-end-fixed cantilevers with 21 µm x 21 µm and 0° aligned gratings (10x magnification), b) One-end-fixed cantilevers with 21 µm x 21 µm and 0° aligned gratings (20x magnification), c) One-end-fixed cantilevers with 21 µm x 36 µm and 0° aligned gratings (10x magnification), d) One-end-fixed cantilevers with 21 µm x 36 µm and 0° aligned gratings (20x magnification), e) Tuning fork cantilevers with 21 µm x 21 µm and 0° aligned gratings (10x magnification), f) Tuning fork cantilevers with 21 µm x 21 µm and 0° aligned gratings (20x magnification).

It can be seen in Figure 2.27 that different types of cantilevers including one-end-fixed and tuning fork designs are fabricated. As a result of etching until the oxide layer, a much better and smooth surface with respect to previously fabricated chips are achieved. At the end of fabrication, the surface roughness of the oxide layer is measured with Veeco® DEKTAK 8 Surface Profiler. The measurements show that the obtained surface roughness on the oxide layer changes between 0.5 and 5 nm which is quite perfect for the reflection of laser light in the Laser-PD mechanism. In previous fabrication processes performed on silicon surface, the obtained surface roughness was between 15 nm and 30 nm at least. Furthermore, the release of cantilevers is checked with the stylus of Surface Profiler.

2.4. Optimization Work on Fabrication

In addition to starting to work with a quarter wafer, three additional important developments are achieved in the fabrication process of a biosensor chip. The achieved developments are for lithography, development and wet etching & release steps. First development is for the lithography and development step. Second development is about the increasing the quality of the etched silicon surface. And final development is about the etching of gold layer underneath the nickel layer when it is needed to work with a single-layered nickel cantilever.

2.4.1. Improvements on Lithography

In 2^{nd} Generation Layout, because of having a critical length of 2 μm unlike the previous biosensor mask which has a critical length of 3 μm, the photolithography and development processes are changed. In the previous process, the exposure time in the photolithography process is 15 seconds with a development time of 10-15 minutes after 110°C soft bake step for 10 minutes. Without changing the developer solution and soft bake conditions, a calibration experiment is carried out in the photolithography step of the fabrication flow. As a result of this calibration performed with the biosensor mask, the exposure time in the photolithography process is changed to 17.5 seconds with a development time of 4-6 minutes with the usage of new layout. In Table 2.2, the calibration experiment can be seen.

Trial Number	**Exposure Time (seconds)**	**Development Time (minutes)**	**Final Situation**
1	12.5	4 – 6	Too underdeveloped
2	15	4 – 6	Slightly underdeveloped
3	17.5	4 – 6	Ideal
4	20	4 – 6	Overdeveloped

Table 2.2: Photolithography calibration experiment.

As a result of the calibration experiment, in addition to decreasing the development time with the increasing exposure time, some better results are obtained with the biosensor chips. In Figure 2.28 below, the results obtained after the improved recipe can be seen.

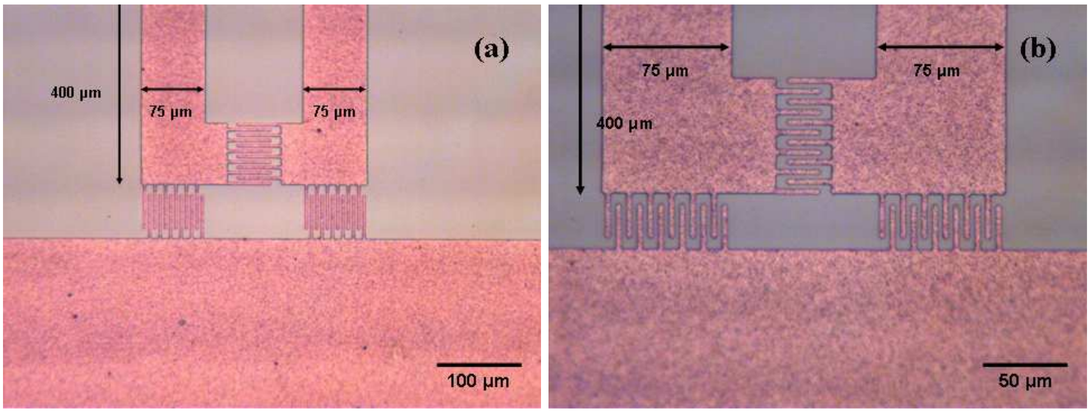

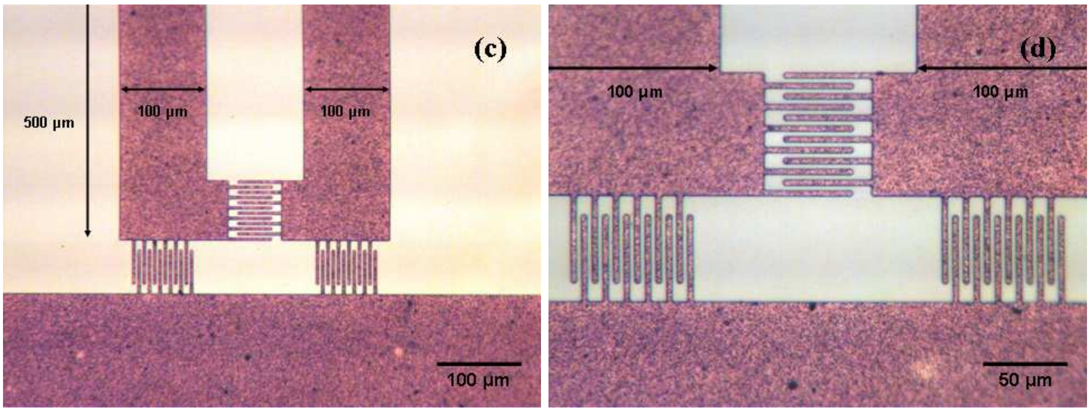

Figure 2.28: Better patterned surfaces obtained with photolithography calibration experiment. a) Static cantilevers having 75 µm x 400 µm geometry (10x magnification), b) Static cantilevers having 75 µm x 400 µm geometry (20x magnification), c) Static cantilevers having 100 µm x 500 µm geometry (10x magnification), d) Static cantilevers having 100 µm x 500 µm geometry (20x magnification).

In Figure 2.28 above, the distance between the fingers is 2 µm as the critical length in the mask. With the previous lithography and development processes, it would be difficult to obtain this distance as a result of overdevelopment or underdevelopment problems. But with the new recipe, this problem is eliminated as it can be seen in Figure 2.28.

2.4.2. Wet Etching of Silicon Layer

The wet etching of silicon layer is one of the most critical steps in the fabrication process. During this process, the final layer on which cantilevers are standing is engraved and cantilevers stand freely. In this step, the quality of the etched silicon surface is very important. If the etching process makes the silicon surface rough, this can affect the Laser-PD optical readout mechanism. Since part of the laser light reflects from the silicon surface, the reflected light may scatter or lose the correct path if the silicon surface is not smooth enough [43].

In previous fabrication flow, the anisotropic etching of the silicon layer is performed in a 35 % KOH solution at a temperature of 65°C as the optimum conditions [20, 39]. As the first change, the temperature of the KOH solution is decreased from 65°C to 60°C, and the concentration of the same solution is changed from 35 % to 44.44 % in order to slow down the etching rate and to perform the etching process in a more controlled manner. In previous studies [48, 49], it was shown that the rate of anisotropic KOH etching for <1-0-0> oriented silicon wafers decelerates with decreasing temperature and increasing concentration from 30 % to 40 % for an etching procedure performed around 60°C. And as the second change, the way of stopping the chemical reaction is improved. In the previous fabrication procedure, once the silicon etching is over, the chip is put inside quenching DI water Pyrex. Then, the Pyrex is placed under the DI water tank and the water is poured through the water Pyrex. Hence, the chip is washed at the same time. In order to dry the cantilevers, the chip is directly placed on the magnetic heater plate for some time. At the end of this process, the cantilevers are released. However, because of the harsh etching of silicon layer and washing of the chip afterwards; the silicon surface is rough, and some of the long cantilevers with aspect ratios of 15 and 20 are bended and stuck on the silicon surface. But because of working with short cantilevers having aspect ratios of 5, this is not considered as a big problem. In Figure 2.29 below, previously fabricated chips with cantilever sticking and silicon surface roughness problems can be seen.

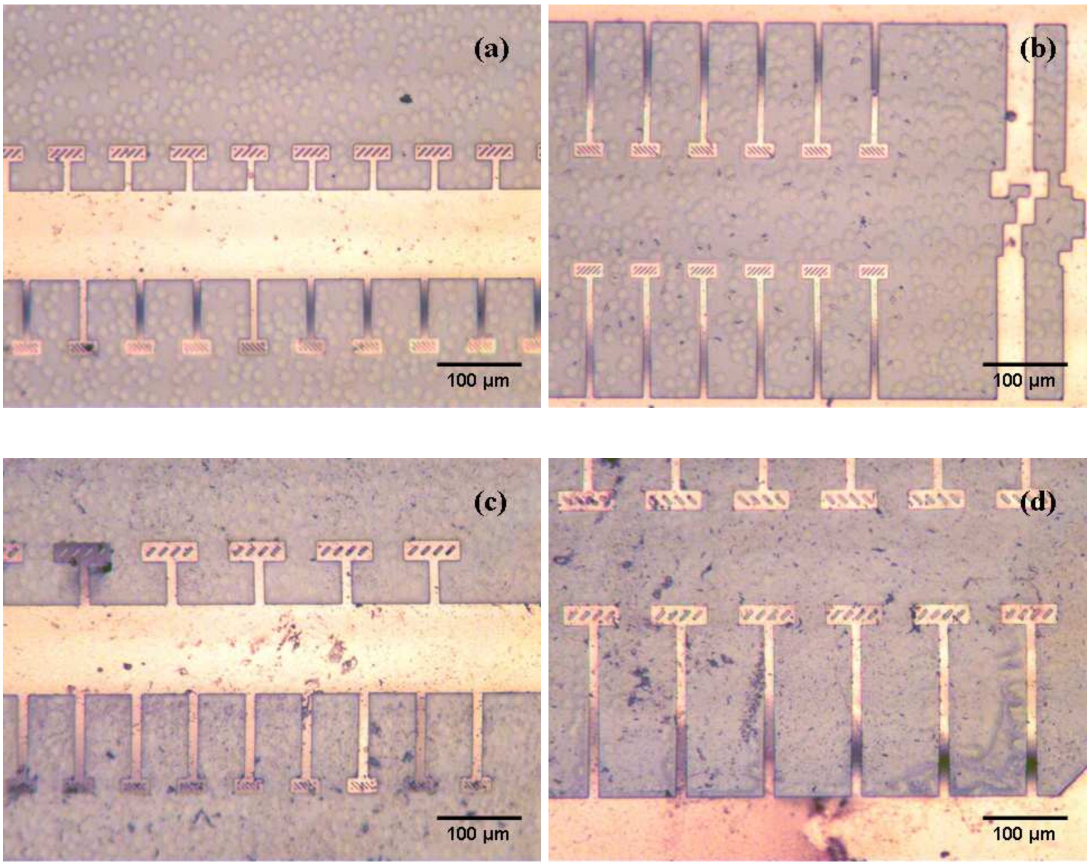

Figure 2.29: Released 7 µm-width cantilevers with sticking and silicon surface problems.

In order to overcome these problems, the step of washing the chip directly under the DI water tank is removed. Instead of this step, the chip is placed in acetone and Isopropyl Alcohol (IPA) solutions respectively right after quenching the chip with DI water. The chip is kept inside these solutions for 5-10 minutes separately. Then, the chip is placed on the magnetic heater plate with a tissue paper underneath it. In Table 2.3, the comparison between the new and old quenching steps for anisotropic silicon etching can be seen.

Step No.	**Process Name**	**Old Recipe**	**New Recipe**
0	Preparation	Solution Concentration = 35 %	Solution Concentration = 44.44 %
1	Heating	Solution Temperature = 65°C	Solution Temperature = 60°C
2	Quenching	Chip is washed under DI water tank.	Chip is kept inside Pyrex for some time.
3	Quenching	-	DI water inside Pyrex is changed regularly.
4	Cleaning	-	Chip is placed inside Acetone. (5-10 minutes)
5	Cleaning	-	Chip is placed inside IPA. (5-10 minutes)
6	Drying	Directly on the magnetic heater.	On magnetic heater with a tissue paper underneath.

Table 2.3: Comparison between the old and new recipes for anisotropic silicon etching process.

As a result of this behavior, better silicon surfaces are obtained with more usable long cantilevers. The surface roughness of the etched silicon layer is decreased from 50-100 nm to 15-30 nm. In Figure 2.30 below, the development of the fabricated chips can be seen.

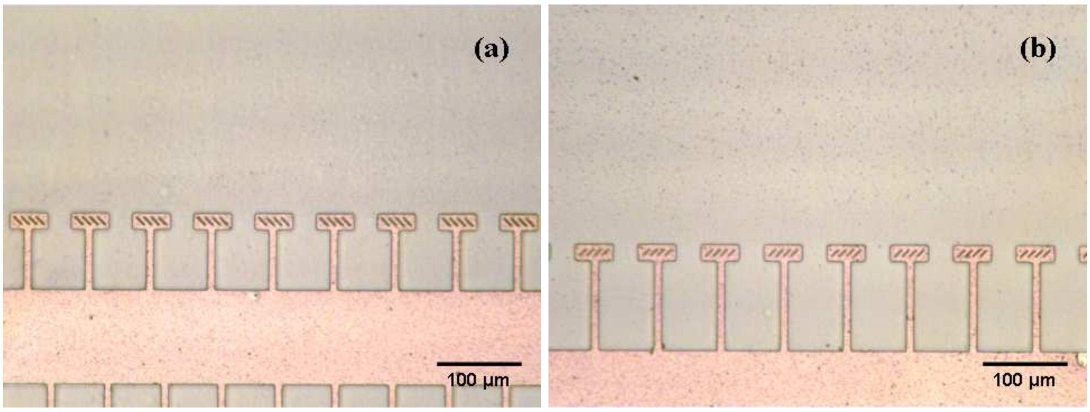

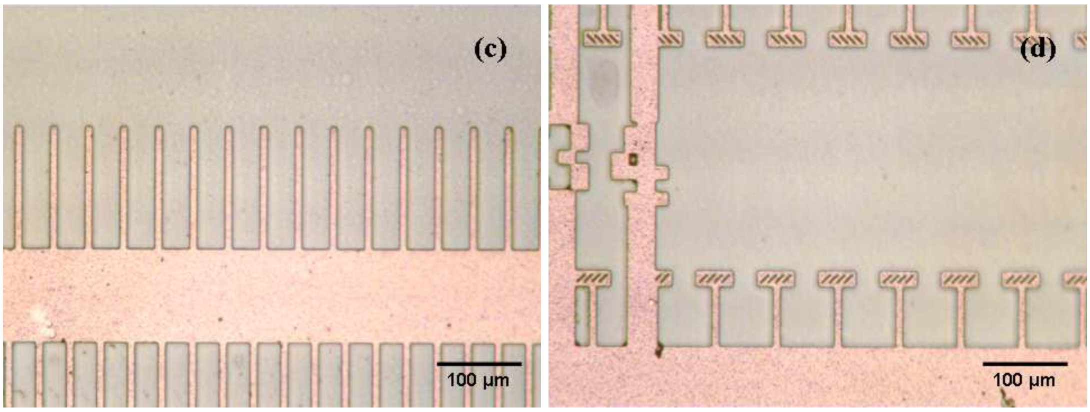

Figure 2.30: Released 7 µm-width cantilevers after solving the sticking and silicon surface problems.

Increasing the quality of the silicon surface is an important development for the fabrication process. In that manner, the quality of the optical readout mechanism also increases.

2.4.3. Wet Etching of Gold Layer underneath Nickel Layer

For some experiments, it is needed to fabricate mono-layered nickel cantilevers. In order to achieve this, the gold layer which is used as the functionalization layer underneath the nickel layer should also be etched. As it was stated at the beginning of this chapter, the wet etching of the gold layer on the surface is carried out with a commercial Transene Inc. GE-8148® type gold etchant. The etchant is mixed with DI water, and the gold surface is etched in order to reach the chromium surface. However, when the etching of gold layer underneath the nickel layer is subjected; there occurs a problem on the nickel surface and whole fabrication process is perished in the final step. In the literature, the reason for this problem is explained as the presence of either Copper-Iodine (CuI) or Gold-Iodine (AuI) in the environment. The damage on the cantilevers can be caused because of a localized difference in concentration or an abrupt decrease of localized pH [50]. This behavior is not observed when the gold layer on the surface is etched; but when the layer inside a gap is tried to be etched, the iodine causes the formation of a precipitation like structure on the cantilevers because of not being cleaned sufficiently. Figure 2.31 explains the problem clearly.

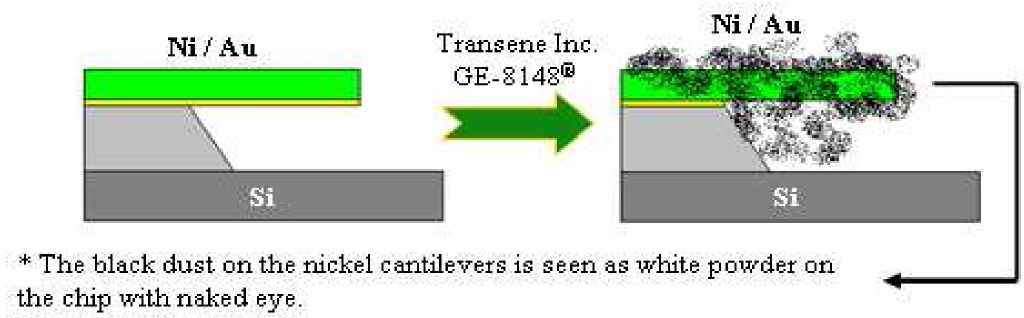

* The black dust on the nickel cantilevers is seen as white powder on the chip with naked eye.

Figure 2.31: The precipitation formation as a result of etching the gold layer underneath the nickel layer.

Since the Transene Inc. GE-8148® type gold etchant is composed of Potassium Iodide (KI), Iodine (I_2) complex and phosphate compound, the problem is caused because of this etchant [51]. In that case, it is advised to agitate the chip inside the gold etchant in spite of being a dangerous operation for the released cantilevers [50]. This is tried, but does not help to solve the problem. In Figure 2.32, the effects of etching the gold layer underneath the nickel layer by using Transene Inc. GE-8148® type gold etchant can be seen.

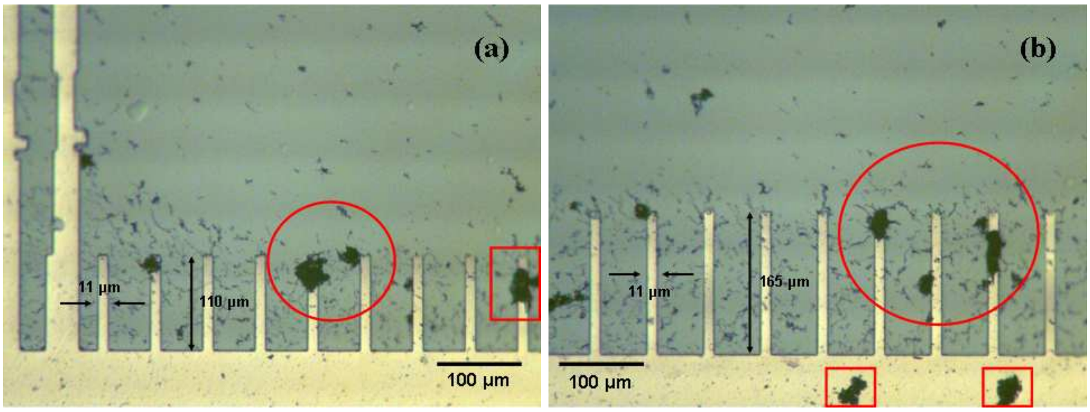

Figure 2.32: Black dust formation on the 11 µm-width cantilevers as a result of etching the gold layer underneath the nickel layer.

Hence, it becomes a necessity to find another solution as a gold etchant. In that manner, “Aqua Regia” is tried as the primary choice. Aqua Regia is composed of Nitric Acid (HNO_3) and Hydrochloric Acid (HCl), and is a very strong etchant both for gold and for many other materials. The etch rate of Aqua Regia for gold is around 10 µm/min, and can be increased to several 10 µm/min at elevated temperatures [52]. As a result of being a harsh solution, it is thought to dilute Aqua Regia with some amount of DI water. So, a new etchant is prepared which is composed of 3:1:2 HCl:HNO_3:DI water. The etch rate for this solution 680 nm/min for gold material; in addition to this, this solution can etch the nickel material and its etch rate is 100 nm/min [53]. Since the thickness of gold layer underneath the nickel layer is around 100 nm, it will be enough to keep the chip for 10 seconds inside the solution. At the same time, around 15 nm of nickel layer is also etched inside this solution. In Table 2.4, the comparison between the new and old etchants can be seen.

Etchant	**Composition**	**Etching Time (seconds)**	**Final Situation**
Transene Inc. GE-8148®	Potassium Iodide (KI), Iodine (I_2) complex, phosphate compound	15	White precipitation on the chip
Diluted Aqua Regia	Nitric Acid (HNO_3), Hydrochloric Acid (HCl), DI water	10	No damage to the cantilevers

Table 2.4: Comparison between Transene Inc. GE-8148® and Diluted Aqua Regia gold etchants.

When diluted Aqua Regia is tried, a relatively better chip is obtained. No white powder is observed on the chip, but there occurs some local damages on the silicon and nickel surfaces. However, these damages can be considered negligible with respect to the cantilevers fabricated with previous gold etchant. In Figure 2.32, released mono-layered nickel cantilevers can be seen.

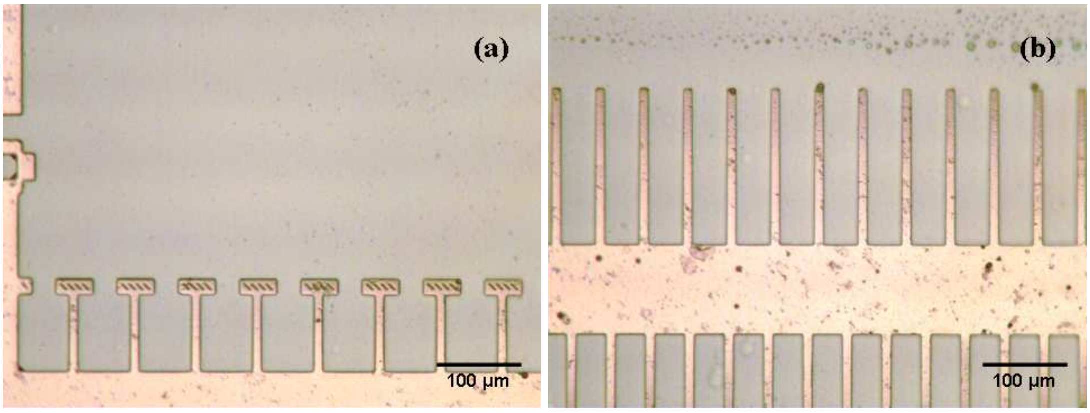

Figure 2.33: Released 9 μm-width cantilevers after etching the gold layer underneath the nickel layer with Aqua Regia.

In Figure 2.33 above, the local damages occurred on nickel and silicon surfaces can be seen. But, these may not affect the working quality of the cantilevers as the previous gold etchant. With some more characterization about Aqua Regia, the process may be more useful and nondestructive.

Chapter 3 - USE OF RESONANCE TECHNIQUE IN THE DETERMINATION OF THE MODULUS OF ELASTICITY

In this chapter, experiments are explained where elastic properties of the materials that are used in the micro-cantilever resonators are obtained. It is obvious that nickel, gold and chromium materials take the most important parts in these devices and it is indeed critical to have a good estimate of their mechanical properties. In that manner, the modulus of elasticity values of electro-plated nickel and sputtered gold and chromium materials will be shown by using two different setups with Laser Doppler Vibrometer (LDV) and Laser-Photo-diode (Laser-PD). In these experiments, three different cantilever structures are used. Mono-layered nickel cantilever beam is used to find the nickel modulus of elasticity, double-layered nickel-gold cantilever beam is used to find the gold modulus of elasticity and triple-layered nickel-gold-chromium cantilever beam is used to find the chromium modulus of elasticity. The structures with their intended uses can be seen in Figure 3.1.

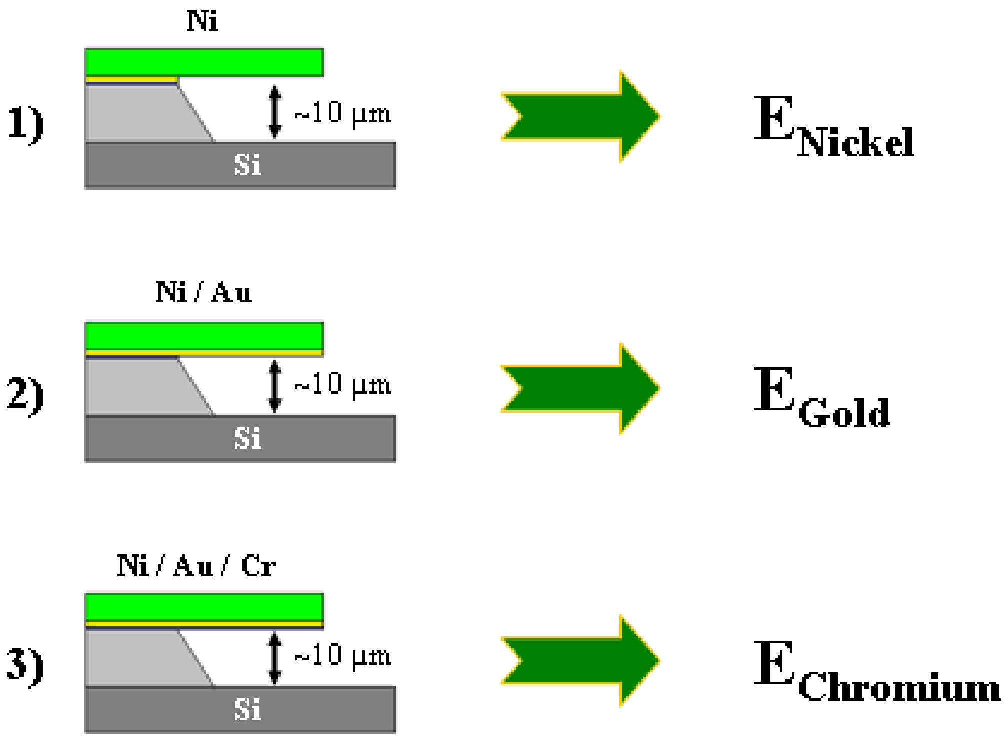

Figure 3.1: Different cantilever structures are used to obtain modulus of elasticity values.

The modulus of elasticity values are obtained with resonance technique. Hence, it is important to understand the resonance technique with LDV and Laser-PD setups. Therefore the working principles for these setups are demonstrated at the beginning of this chapter. The resonance behavior for a micro-cantilever resonator is explained with governing parameters. Then, formulations used for the calculation of modulus of elasticity values for electro-plated nickel and sputtered gold and chromium materials are shown. Furthermore, the experimental results obtained with the resonance frequency measurements are demonstrated. Finally, a long-term reliability study on micro-cantilever resonators will be illustrated.

As an important material that is used in MEMS fabrication, the mechanical properties of the nickel material should be carefully investigated. These properties can exhibit great differences from device to device. The utilized electro-plating bath can directly affect the performance of the whole device. Since the characteristics of plating bath changes with parameters such as temperature and current density, a specific modulus of elasticity value should be determined for further experiments [23].

In order to determine the modulus of elasticity of specific thin films, many methods have been used. These methods can be classified as destructive and non-destructive methods. Destructive methods are used to identify the mechanical property of a material such as yield stress and fracture toughness by simply damaging it or changing its structure. Bulge test, micro-beam bending, micro-tensile test, wafer curvature method and resonance method are the most important types for destructive methods [24, 54, 55]. Non-destructive methods are used to find the elastic properties of the materials only, and require special instrumentations. These methods are based on the direct measurement of acoustic-waves for obtaining modulus without changing any properties of the materials. In addition to these, Nanoindentation method can be used to find both elastic and hardness properties of the materials. [24, 54, 55]. As a result of these experimental methods, some values were obtained for the modulus of elasticity of the nickel thin films as shown in Table 3.1.

Methods	**Young's Modulus (GPa)**
Bulk	200
Tension	160 – 204
Bending	139 – 167
Indentation	146 – 184

Table 3.1: Modulus of elasticity values for the nickel thin films obtained in different experiments. (Adapted from Ref. [23])

Kim & Boyd worked with electro-plated nickel cantilever beams with a thickness around 1 μm [23]. The electro-plating current density was kept constant at 5.1

A/dm^2 (51 mA/cm^2). The modulus measurement is carried out by applying force onto the nickel electro-plated cantilever with the tapping mode of an Atomic Force Microscope (AFM). In Figure 3.2, the obtained Young's Modulus values can be seen.

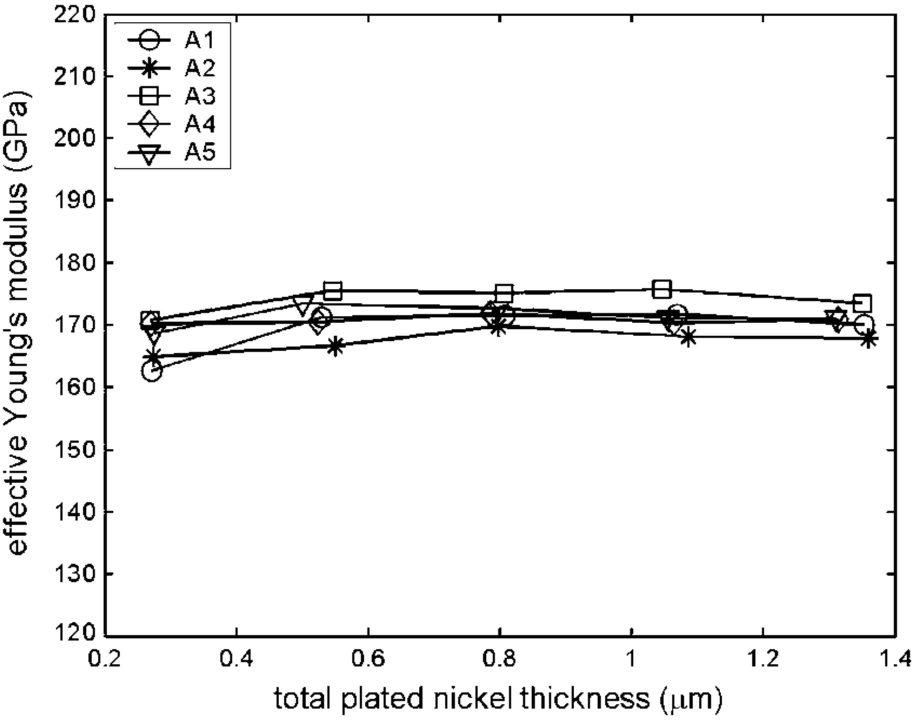

Figure 3.2: Modulus of Elasticity values for electro-plated nickel thin films. [23]

As it can be seen in Figure 3.2, the average Young's Modulus value for electro-plated nickel material was found as 170.73 ± 3.47 GPa in this study [23].

In another study, a characterization experiment was carried out by using electro-plated commercial nickel cantilever beams, and the modulus of elasticity was found between 155-164 GPa with an average of 159 GPa for these structures [25]. The results for this study can be seen in Figure 3.3. The cantilevers used in this study have geometry of 700-1000 μm length, 100 μm width and 20 μm thickness. The electro-plating of nickel was carried out in a solution which has a temperature and pH values of

30°C and 4, respectively, with a current density of 20 mA/cm^2. Furthermore, the modulus measurements in this study were performed with resonance technique [25].

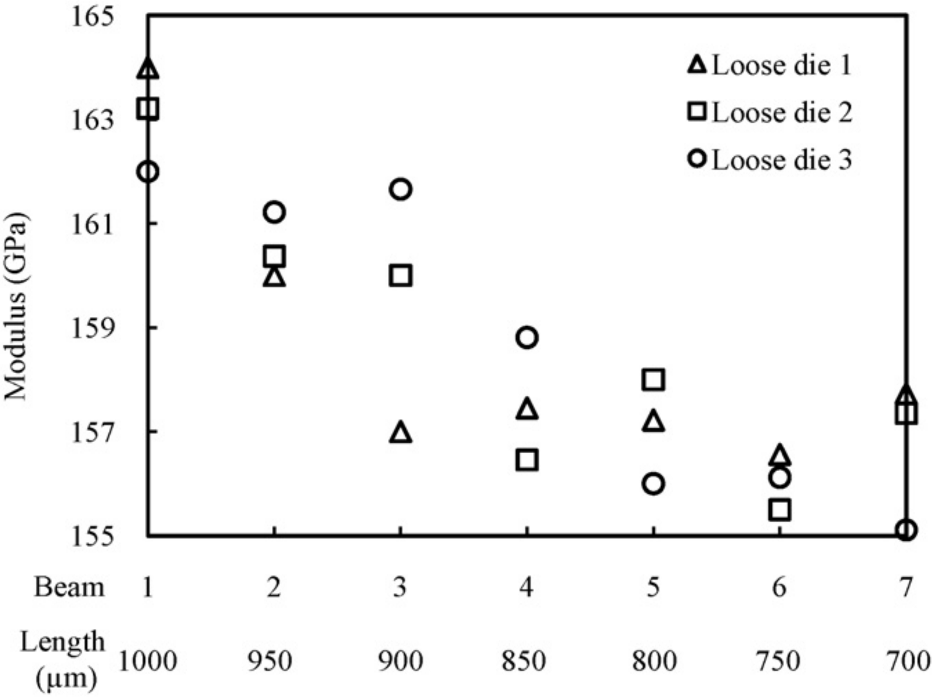

Figure 3.3: Modulus of Elasticity values for commercial electro-plated nickel thin films. [25]

In another study regarding the nickel modulus of elasticity [26], the effect of current density to modulus was investigated. In this study, the cantilevers have geometry of 700 and 715 μm lengths, 19.5 and 28.5 μm widths, and 25 μm thicknesses. At the end, it was shown that as the current density of the plating bath increased from 2 mA/cm^2 to 20 mA/cm^2, the modulus of elasticity of the electro-plated nickel decreased from 205 GPa to 165 GPa.

It can be easily seen that for modulus of elasticity studies of the electro-plated nickel material, the current density and temperature of the plating solution play an important role. Since these parameters change the characteristics of the electro-plating process, the modulus of elasticity also changes. In a similar study regarding the effects of these parameters to modulus of elasticity of the electro-plated nickel [27], it is also found that as the current density increases, modulus of elasticity of the electro-plated nickel material decreases. This experiment is carried out at 60°C temperature for the electro-plating bath. In Figure 3.4, this phenomenon can be seen clearly.

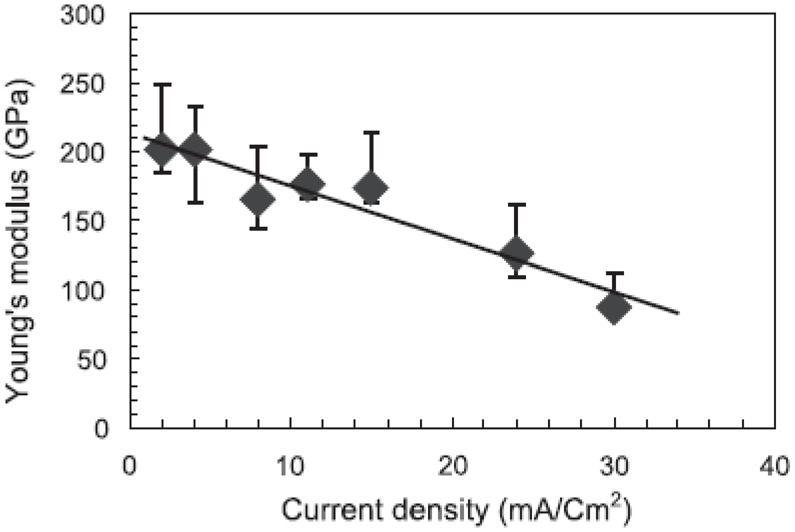

Figure 3.4: Current Density effect to Nickel Modulus of Elasticity. [27]

Similarly, many studies were conducted for gold thin films regarding its modulus of elasticity. These studies include the usage of different testing mechanisms such as micro-membrane deflection for e-beam deposited; nanoindentation for electro-plated; electrostatic actuation, bulge test, micro-membrane deflection, nanoindentation, micro-cantilever bending and Magnetostrictive Strip Sensor (MSS) for sputtered gold material. These results provided a range between 53 and 130 GPa for the gold thin film modulus of elasticity, whereas bulk modulus value is, 78 GPa [24]. Another study related to this subject was conducted with electro-plating method. Gold was electro-plated at different current densities such as 2 mA/cm^2 and 4 mA/cm^2 until reaching a total thickness of 3-4 μm. As a result of this research, a range of 42 and 52 GPa was obtained for the modulus of elasticity of the electro-plated gold material [28].

About the final crucial material in the fabrication process which is chromium, it was seen that the modulus of elasticity of sputtered chromium material is much lower than its bulk value which is 248 GPa. Previous studies showed that the modulus of elasticity for sputtered chromium material changes between 107 GPa and 234 GPa for nanoindentation test. For 3-point bending test, this value was found as 275 GPa [24]. In another study related to this subject, instead of using the sputtered chromium material, the cantilevers were fabricated with thermal evaporation method by using the chromium material. The cantilevers were made of thin chromium films with sub-100 nm thickness values as 50 nm, 68 nm and 83 nm. An external force was applied on the cantilevers and the deflections of them were monitored by an AFM probe. From these deflection values, the modulus of elasticity of these thin chromium films were found as in Figure 3.5.

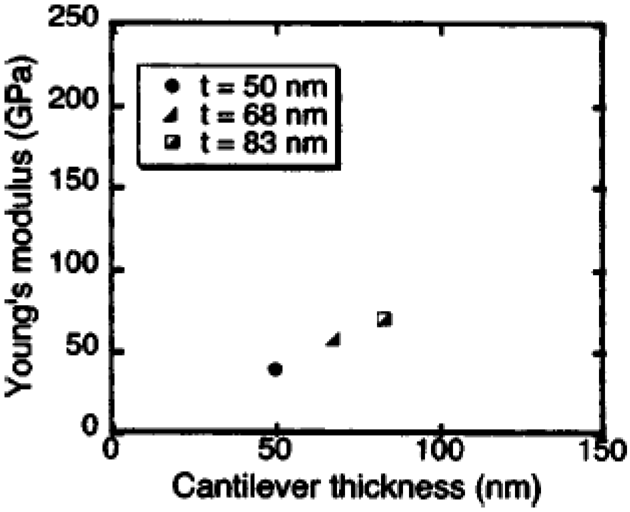

Figure 3.5: Modulus of elasticity values for thermally evaporated chromium cantilevers with sub-100 nm thicknesses. [29]

In Figure 3.5, it can be seen that when the thickness of chromium layer is smaller than 100 nm, modulus of elasticity is found between 40 GPa and 70 GPa which is considerably different with the bulk modulus value. However, the results were supported with previous studies [29, 56]. Another interesting point is that the experimental error for the obtained modulus of elasticity for the chromium material is negligible for 0,1 μm or higher thickness values; but the error increases with the decreasing thickness [24]. Hence, film thickness is a critical parameter for modulus of elasticity investigation for sputtered thin chromium films.

These studies emphasize the importance of modulus of elasticity of nickel, gold and chromium materials for experiments regarding micro-cantilever technology. Furthermore, the obtained results show that the experimental modulus values for the electro-plated nickel material are found smaller with respect to its bulk value. Parameters such as current density and temperature directly affect the experimental modulus results. The details of the electro-plating recipe are the major reason for this situation. For the modulus of elasticity of the sputtered gold and chromium materials, there is a wide range of experimental results. Furthermore, the thickness of the material plays an important role for the modulus calculations.

In this manner, experiments are carried out in order to estimate the modulus of elasticity of the electro-plated nickel, and sputtered gold and chromium materials with resonance frequency method by using LDV and Laser-PD setups. In Section 3.1, the working principle of LDV and Laser-PD setups are explained. This section will be followed by examples of resonance behavior and details of theoretical formulations. Then, the obtained results for modulus of elasticity of electro-plated nickel, and sputtered gold and chromium thin films will be illustrated. Finally, the reliability study for nickel coated cantilevers will be discussed.

3.1. Experimental Setups

The resonance frequency of micro-cantilever resonator is measured with an optical readout mechanism. In these mechanisms, either an LDV or a Laser-PD mechanism can be used as the major measurement tools. If resonance frequencies of mono-layered nickel cantilevers are measured, an LDV setup is used. If resonance frequencies of multiple-layered nickel cantilevers with grating structures at their tips are measured, a Laser-PD setup is used. For a Laser-PD mechanism, a HeNe laser with a 633 nm wavelength is used as the source of the light. In the mechanism, this light comes onto the nickel grating structures which are located at the tips of the cantilever beams. Part of this light reflects from the grating structure, and part of it reflects from the silicon surface underneath. As a result of this, diffraction orders form. These orders can be numerated as 0th, 1st, -1st, 2nd, -2nd, 3rd and -3rd. In Figure 3.6, the diffraction grating orders that occur as a result of the reflected light can be seen.

By using an optical aperture, the 1st order of this reflected light is chosen and this order is focused onto a photodiode. This photodiode observes the intensity modulation and creates a signal while the cantilevers are oscillating.

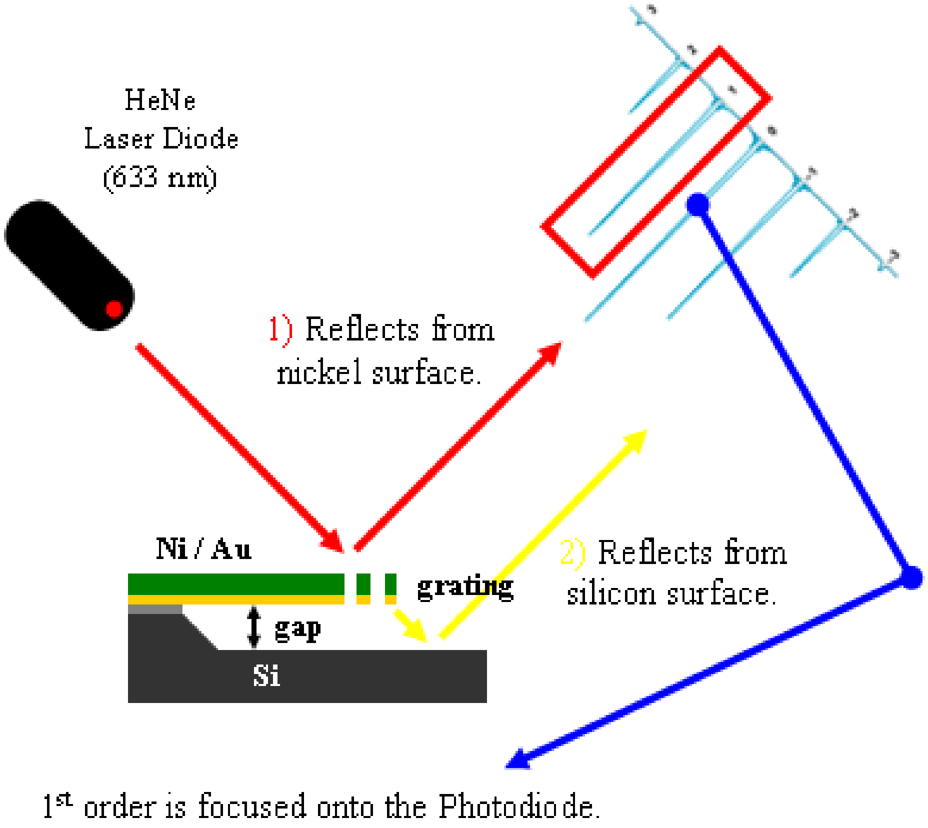

Figure 3.6: Formation of diffraction grating orders.

For an LDV mechanism, LDV is used as the source of the light. The light is focused onto the nickel surface. When it reflects from the nickel surface, it undergoes a frequency change depending on nickel's velocity. Hence, it is able to monitor the movement of the cantilever.

In addition to this, environmental noise also plays an important role for the LDV and Laser-PD measurement mechanisms. In order to show this, the resonance frequency of a micro-cantilever is measured by both an LDV and a Laser-PD setup at the same time without vibration isolation. In this study, it is seen that an LDV setup is affected more than a Laser-PD setup when subjected to a continuous environmental noise. This fact can be seen in Figure 3.7.

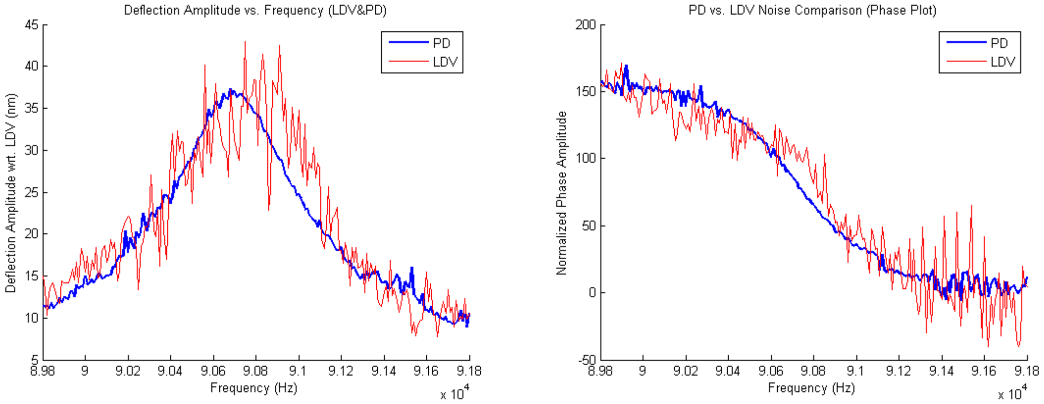

Figure 3.7: Comparison of LDV and Laser-PD setups. (Cantilever dimensions are 12 µm in width and 60 µm in length.)

For both mechanisms, the oscillation of the cantilevers is provided by using magnetic actuation method with an electrocoil. This electrocoil can excite many cantilevers at the same time; but because the light is focused on one cantilever only, the resonance frequency of this cantilever can be figured out.

In these setups, the instrumentation consists of a signal generator, an oscilloscope and a preamplifier. Signal generator is connected to the electrocoil, so it excites the cantilevers by feeding the electrocoil. Furthermore, the signal generator is connected to oscilloscope to see the given input signal. It is possible to see both the input and output signals by using the oscilloscope. Output signal is obtained with a connection through the photodiode in a Laser-PD mechanism or directly LDV itself. It is also possible to clear and increase the quality of this signal by using a preamplifier. As the signal is obtained with this mechanism, the resonance frequency can be found by using the signal generator. When the resonance frequency of the cantilever is reached, the output signal on the oscilloscope attains a maximum value. By using a GPIB interface and a MATLAB code, frequency is swept around a value which is near the resonance point. Frequency sweep plays an important role for finding the exact resonance frequency of a cantilever. In Figure 3.8 and 3.9 below, the schematic and the actual views of the Laser-PD setup, and in Figure 3.10 the schematic view of the LDV setup used in the experiments which are used to find the resonance frequency can be seen.

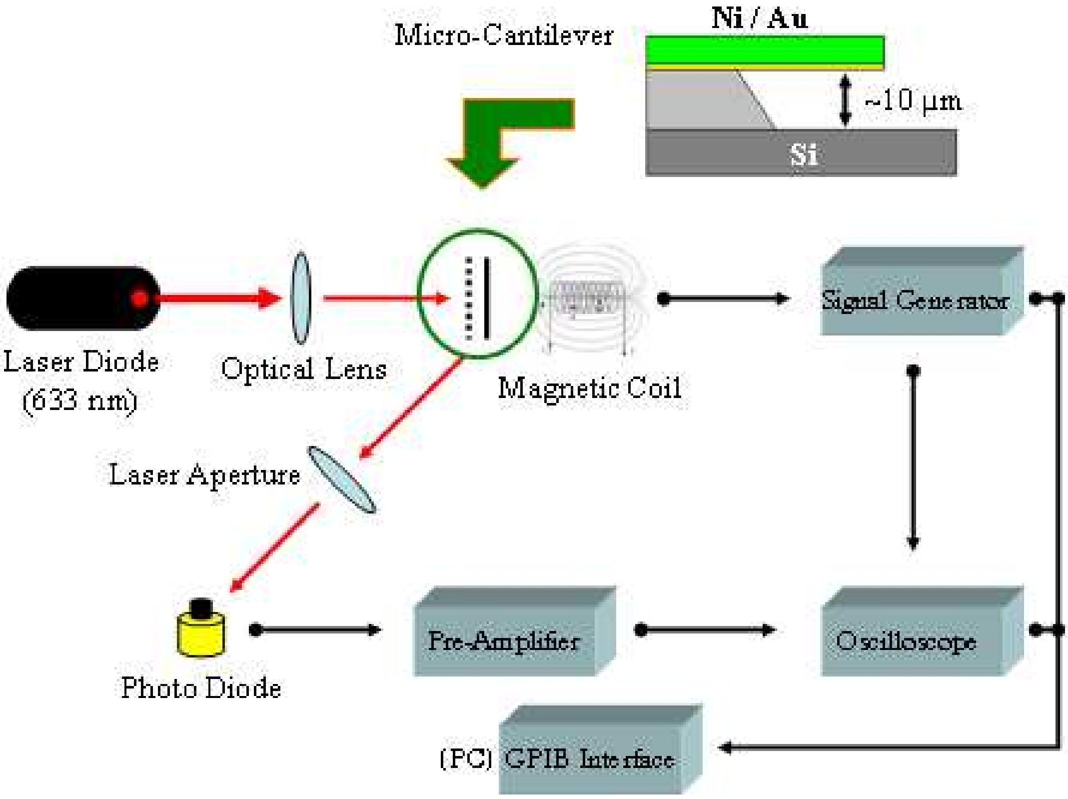

Figure 3.8: The schematic view of the Laser-PD mechanism.

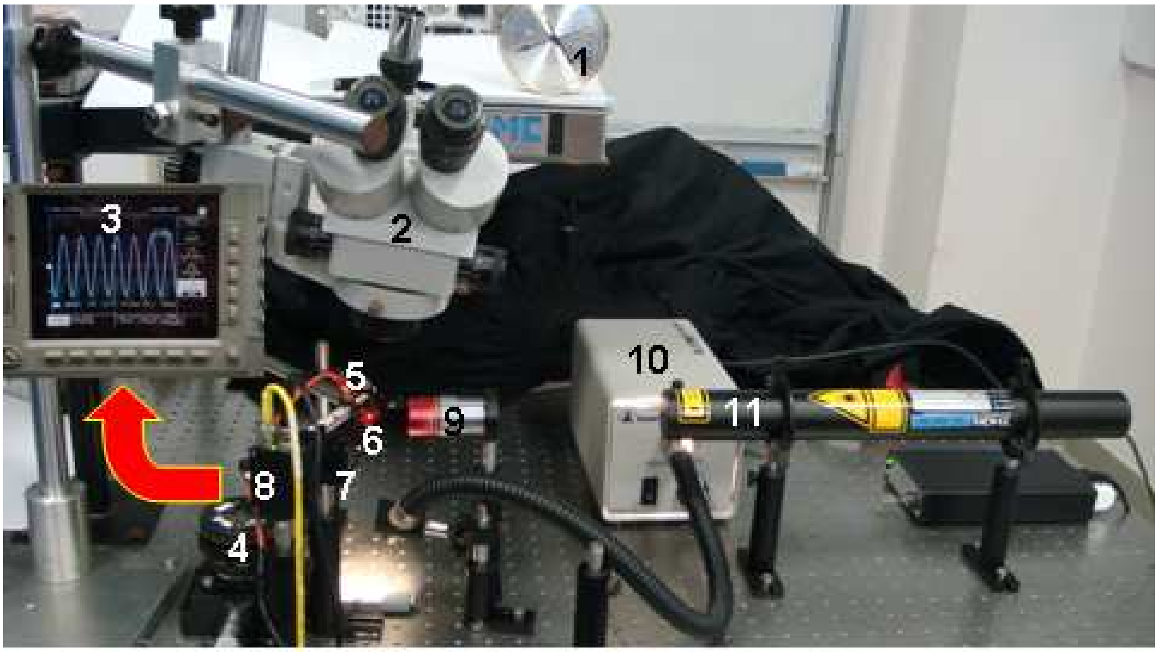

Figure 3.9: The actual view of the Laser-PD mechanism: 1) Thermometer and Hygrometer for temperature and relative humidity measurements, 2) Microscope for viewing the measured micro-cantilevers, 3) Input (green) and output (white) signals on the oscilloscope screen, 4) XYZ Stage for adjusting the micro-cantilever position, 5) Electrocoil for providing the magnetic actuation, 6) Micro-cantilever, 7) Laser Aperture, 8) Photodiode, 9) Optical Lens, 10) Light for increasing the visibility of micro-cantilevers in the microscope, 11) 633 nm HeNe Laser source.

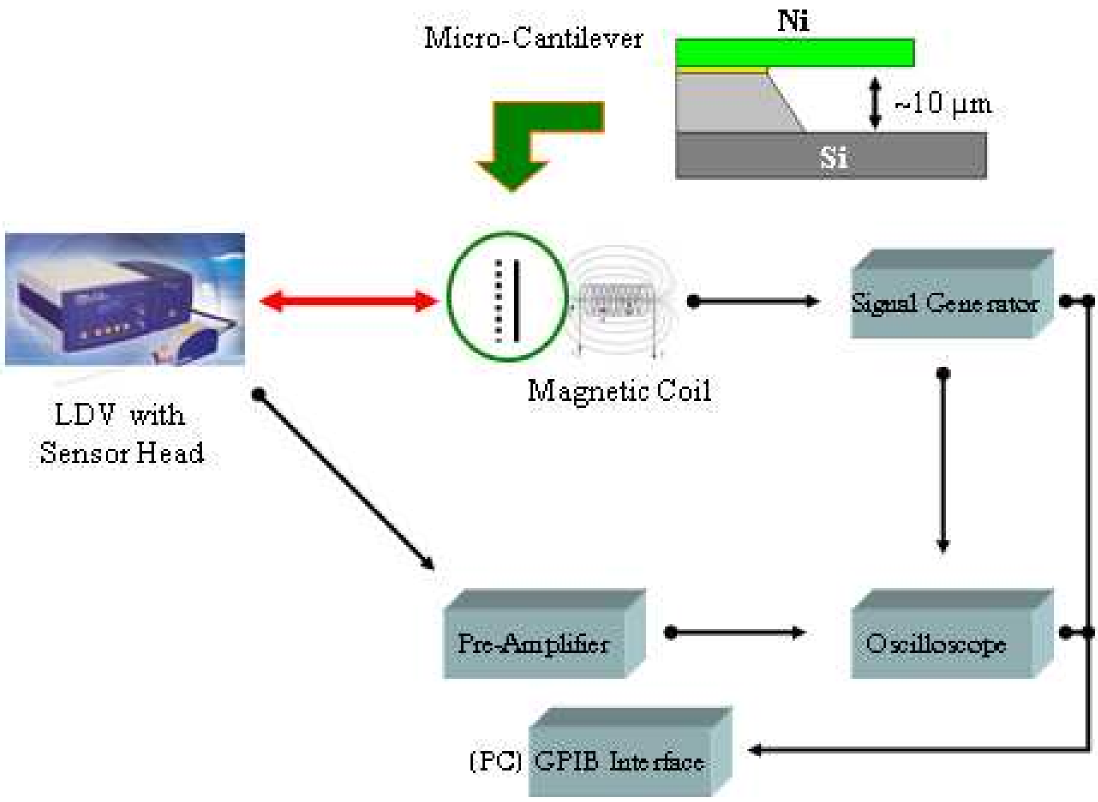

Figure 3.10: The schematic view of the LDV mechanism.

With the frequency sweep method, a graph is obtained for the resonance frequency of the cantilever. The peak value of this graph gives the desired frequency value for the experiments. A sample graph which is obtained as a result of this operation can be seen as in Figure 3.11. Here, the cantilever dimensions are 12 µm in width, 60 µm in length. This geometry leads to a resonance frequency around 119 kHz.

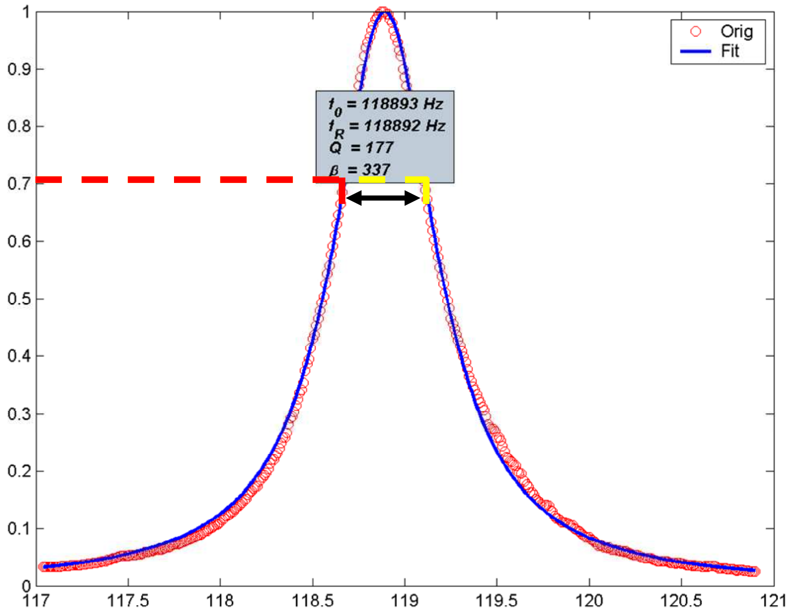

Figure 3.11: A sample graph obtained with the frequency sweep method.

In Figure 3.11, f_0 is the resonance frequency, f_R is the damped resonance frequency, Q is the quality factor and β is the damping factor. These parameters can be obtained by using a Lorentzian-like nonlinear fit onto the resonance frequency curve which is measured with the optical readout setup. In the curve, there is specific distance called "Linewidth". Linewidth (shown with black arrow on the graph) is the distance on the x-axis of the graph which corresponds to the place between the two specific points of the left and right sides of the frequency sweep curve. These two points can be found by multiplying the maximum point on the y-axis with $1/\sqrt{2}$, and drawing lines (shown with red and yellow dashed lines on the graph) from these points onto the x-axis. β can be found by dividing the Linewidth by 2. Q can be computed by dividing the resonance frequency, (f_0), with Linewidth. Finally, damped resonance frequency, (f_R), can be computed using Eqn. 3.1.

$$f_R = \sqrt{f_0^2 - 2\beta^2} \qquad \text{(Eqn. 3.1)}$$

The difference between the resonance frequency and the damped resonance frequency is negligible in air as evident from Figure 3.11.

The resonance behavior is significant both for Laser-PD and LDV measurement mechanisms. In Section 3.2, this behavior is explained with experimental data.

3.2. Resonance Behavior

Resonance frequency is an important concept for the micro-cantilever research area. Biological binding experiments are carried out with respect to the shifts in the resonance frequency of a cantilever beam [3, 18, 19]. Hence, it is critical to obtain the resonance frequency carefully. In order to achieve this, the parameters which affect the resonance frequency should be understood completely. These parameters can be divided into two groups as material properties and dimensions. In this section, two experimental data will be shown in order to clarify the effect of dimension on the resonance frequency. First experimental data are obtained by measuring the resonance frequencies of 12 μm-width and 60 μm-length cantilevers. By using these cantilever types, the effect of thickness to the resonance frequency is figured out. In Figure 3.12 below, this effect can be seen. It can be seen in Figure 3.12 that there is a linear relationship between the thickness and the resonance frequency. As the thickness of the cantilever increases, the resonance frequency also increases.

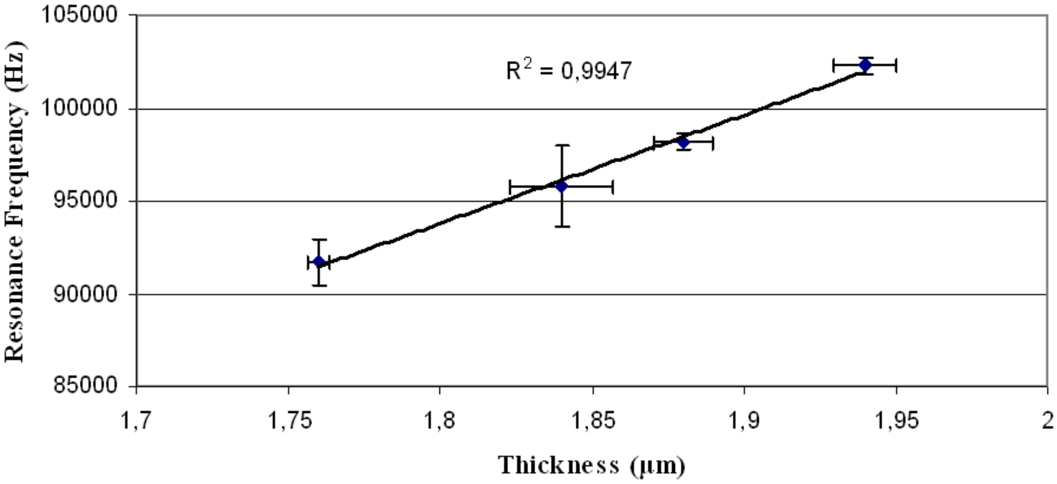

Figure 3.12: Resonance frequency variation with respect to thickness change.

Second experimental data are obtained by measuring the resonance frequencies of five different cantilever types. The cantilevers have a width of 3, 4, 5, 6 and 7 µm with an aspect ratio of 5, where the aspect ratio is defined as the ratio of length to the width of a cantilever beam. In Table 3.2, the change in the resonance frequency with respect to the change in size can be seen.

It can easily be seen in Table 3.2 that there is a variation for the nickel thickness between 1 µm and 1.8 µm. To eliminate the effect of thickness, one can compute the resonance frequency, (f_0), for each cantilever assuming that it has a thickness of 1 µm. This operation is an acceptable practice, since it is well-known that f_0 changes linearly with thickness as seen in Figure 3.12. With respect to this in Figure 3.13 below, the normalized frequency data showing the length effect can be seen.

Chip Number	Width (µm)	Average Nickel Thickness (µm)	Type	# of Measured Cantilevers per Chip	Resonance Frequency (Hz)	Standard Deviation (Hz)
1	3	1	3x15IZ33	55	***320625.89***	***±20593.12***
2	3	1.1	3x15IZ33	44	***332943.54***	***±19841.59***
3	4	1.8	4x20IZ33	46	***308606.02***	***±23681.87***
4	5	1	5x25IZ33	46	***146744.24***	***±13171.18***
5	5	1.3	5x25IZ33	46	***186879.58***	***±11607.68***
6	6	1.2	6x30IZ33	49	***138198.22***	***±18932.04***
7	7	1.1	7x35IZ34 7x35IZ53	48	***102109.54***	***±10269.26***

Table 3.2: Experimental resonance frequency data. ("IZ" defines the grating geometry of the cantilever beams which is introduced in the thesis of Hüseyin İlker Ocaklı [16].)

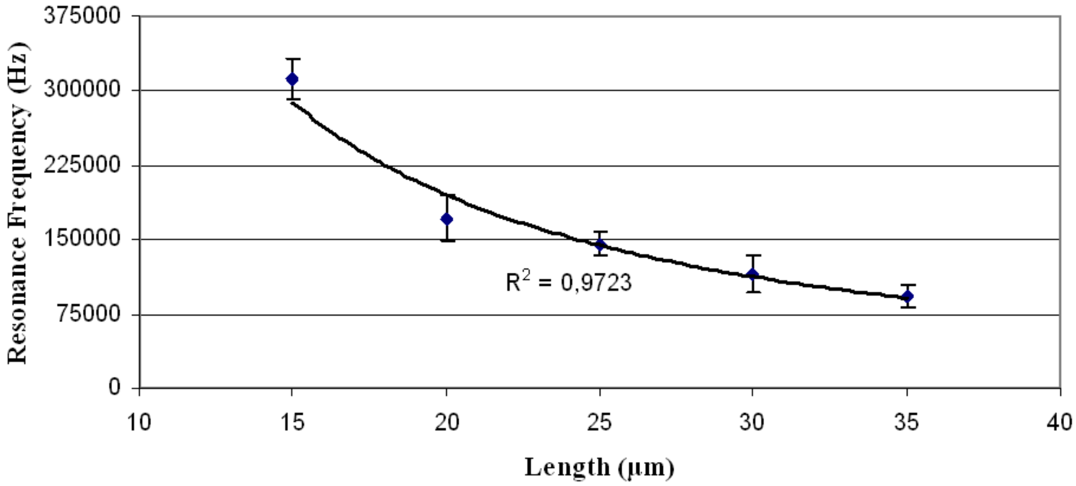

Figure 3.13: Resonance frequency variation with respect to length change.

It can be seen in Figure 3.13 that there is an inverse square relationship between the length and its resonance frequency. As the length increases, the resonance frequency decreases.

In addition to measuring the resonance frequency of a cantilever beam with an optical readout mechanism, some formulations are developed for the calculation of resonance frequency. In Section 3.3, these formulations are demonstrated. The formulations will be utilized when computing the modulus of elasticity.

3.3. Theoretical Formulations

For modulus of elasticity experiments, micro-cantilevers with different geometries are used. As the first experiment, a chip which includes 5 μm-width cantilevers is fabricated. The cantilevers are mono-layered and are composed of nickel material only. Then, 119 cantilevers inside this chip are selected and their resonance frequencies are measured with an LDV setup in order to obtain the nickel modulus of elasticity. For this experiment, a formulation is needed in order to calculate the modulus of elasticity from the resonance frequency. This formulation can be seen as Eqn. 3.2 below;

$$f_0^l = \frac{\sqrt{3}}{12}\frac{(1{,}8751)^2 h}{\pi L^2}\sqrt{\frac{E}{\rho}} \qquad \text{(Eqn. 3.2)}$$

where f_0^l is the resonance frequency for mono-layered cantilever beam.

In the second experiment, three different chips which include 4 μm-width and 5 μm-width cantilevers are fabricated. The cantilevers are double-layered and are composed of nickel and gold materials. Then, 69 cantilevers inside these chips are selected and their resonance frequencies are measured with a Laser-PD setup in order to obtain the gold modulus of elasticity. For this experiment, another formulation is needed in order to calculate the modulus of elasticity from the resonance frequency. This formulation will be the one which was produced from double-layered Bernoulli beam theory and can be seen as Eqn. 3.3 below [20, 57];

$$f_0^{u}=\frac{(1,8751)^2 m_1}{4\pi\rho_1 AL^2}\sqrt{\left(\frac{E_1}{3\rho_1}\right)\frac{\left(\rho_r^4+4\rho_r^3E_rm_r+6\rho_r^2E_rm_r^2+4\rho_rE_rm_r^3+E_r^2m_r^4\right)}{(1+m_r)(\rho_r+E_rm_r)\rho_r^3}} \quad \text{(Eqn. 3.3)}$$

where $\rho_r=\frac{\rho_2}{\rho_1}, E_r=\frac{E_2}{E_1}, m_r=\frac{m_2}{m_1}=\frac{\rho_2h_2wL}{\rho_1h_1wL}$ (L_1=L_2=L), respectively, and f_0^{u} is the resonance frequency for double-layered cantilever beam. When these parameters are included in the formula, a relatively simpler new version will be obtained. This new formula can be seen as Eqn. 3.4.

$$f_0^{u}=\frac{\sqrt{3}}{12}\frac{(1,8751)^2}{\pi L^2}\sqrt{\frac{\left(E_1^2h_1^4+4E_1h_1^3E_2h_2+6E_1h_1^2E_2h_2^2+4E_1h_1E_2h_2^3+E_2^2h_2^4\right)}{(\rho_1h_1+\rho_2h_2)(E_1h_1+E_2h_2)}} \quad \text{(Eqn. 3.4)}$$

In addition to being double-layered cantilever beams, these cantilevers have specific grating structures at their tips. Hence, Eqn. 3.4 is modified as if the cantilevers are carrying end loads at their tips. This modification is made for including the grating effect in the formulation. In this manner, the formulation for calculating the resonance frequency is changed. This formulation can be seen as Eqn. 3.5 below;

$$f_{0-grating}^{u}=f_0^{u}\psi \qquad \text{(Eqn. 3.5)}$$

where $f_{0-grating}^{u}$ is the resonance frequency for double-layered cantilever beam with a grating structure at its tip, and ψ is shown by Eqn. 3.6 below.

$$\psi=0.4926\times\sqrt{\frac{w}{\left(\frac{(w_g-w)L_g}{L'}+Cw-\frac{A_R}{L'}\right)}\frac{L^2}{L'^2}} \qquad \text{(Eqn. 3.6)}$$

In Eqn. 3.6, L' (shown in Figure 3.17) is the specific length parameter for the cantilevers having a grating structure at their tips ($L' = L + (2/3)L_g$). This term is useful for including the grating part effect which is considered as an end load at the tip of the cantilever for resonance frequency calculations [58]. Since the grating part is considered as a separate end load, the weight of the cantilever beam can not be treated as distributed load. Therefore the resonance frequency calculations are not reasonable. If the length of the cantilever beam is taken as L^1 instead of L, the weight of cantilever beam can be treated as distributed load with its grating part.

L^1 is optimized by using a Finite Element Program (ANSYS), and the calculations for this term are available in the thesis of Mehmet Salih Kılıç [20].

In the third experiment, another chip which includes 4 µm-width cantilevers is fabricated. The cantilevers are triple-layered and are composed of nickel, gold and chromium materials. Then, 59 cantilevers inside these chips are selected and their resonance frequencies are measured with a Laser-PD setup in order to obtain the chromium modulus of elasticity. For this experiment, another formulation is needed in order to calculate the modulus of elasticity from the resonance frequency. This formulation will be the one which was derived exactly in the same way with the one that had been done for Eqn. 3.5. The triple-layered grating formulation can be seen as Eqn. 3.7;

$$f_{0-grating}^{III} = \frac{1.732}{2\pi L^2}\sqrt{\left(\frac{A}{h_1\rho_1 + h_2\rho_2 + h_3\rho_3}\right)}\sqrt{\frac{w}{\frac{(w_g - w)L_g}{L'} + Cw - \frac{A_R}{L'}}}\frac{L^2}{L'^2} \qquad \text{(Eqn. 3.7)}$$

where $f_{0-grating}^{III}$ is the resonance frequency for triple-layered cantilever beam, and A parameter can be found with Eqn. 3.8;

$$A = \frac{E_1 h_1^3 + E_2\left(\left(h_1 + h_2\right)^3 - h_1^3\right) + E_3\left(\left(h_1 + h_2 + h_3\right)^3 - \left(h_1 + h_2\right)^3\right)}{3} - z_0\left(E_1 h_1^2 + E_2\left(h_2^2 + 2h_1 h_2\right) + E_3\left(h_3^2 + 2h_3\left(h_1 + h_2\right)\right)\right) + z_0^2\left(E_1 h_1 + E_2 h_2 + E_3 h_3\right) \qquad \text{(Eqn. 3.8)}$$

in which z_0 is the neutral axis of the cantilever beam which can be found as in Eqn. 3.9;

$$z_0 = \frac{\dfrac{E_1 h_1^2 + E_2 h_2^2 + E_3 h_3^2}{2} + E_2 h_1 h_2 + E_3\left(h_1 + h_2\right)h_3}{E_1 h_1 + E_2 h_2 + E_3 h_3} \qquad \text{(Eqn. 3.9)}$$

Since the formulations for calculating the resonance frequency of different cantilever types are determined, the results for modulus of elasticity values can be obtained. In Section 3.4, these results are illustrated.

3.4. Measurements & Results

In this section, the obtained results are shown for the modulus of elasticity values of electro-plated nickel, and sputtered gold and chromium materials.

3.4.1. Measurement of Nickel Modulus of Elasticity

As it was stated in Section 3.3, the resonance frequencies of mono-layered nickel cantilevers are measured with an LDV setup. The resonance frequency measurements are carried out under ambient temperatures. Furthermore, the electro-plated nickel layer thicknesses of the cantilever beams are measured with Veeco® DEKTAK 8 Surface Profiler Machine in the Clean Room. The nickel electro-plating process of the cantilevers is carried out inside a nickel sulphamate bath at 45°C with a current of 40 mA. This corresponds to a current density range of 77.28 mA/cm^2 and 80.84 mA/cm^2.

In this experiment the cantilevers whose widths are 5 µm, and aspect ratios are as 10, 15 and 20 are used. This makes the length of the cantilevers as 50 µm, 75 µm and 100 µm, respectively. In Figure 3.14, the schematic view of a cantilever used in this experiment can be seen.

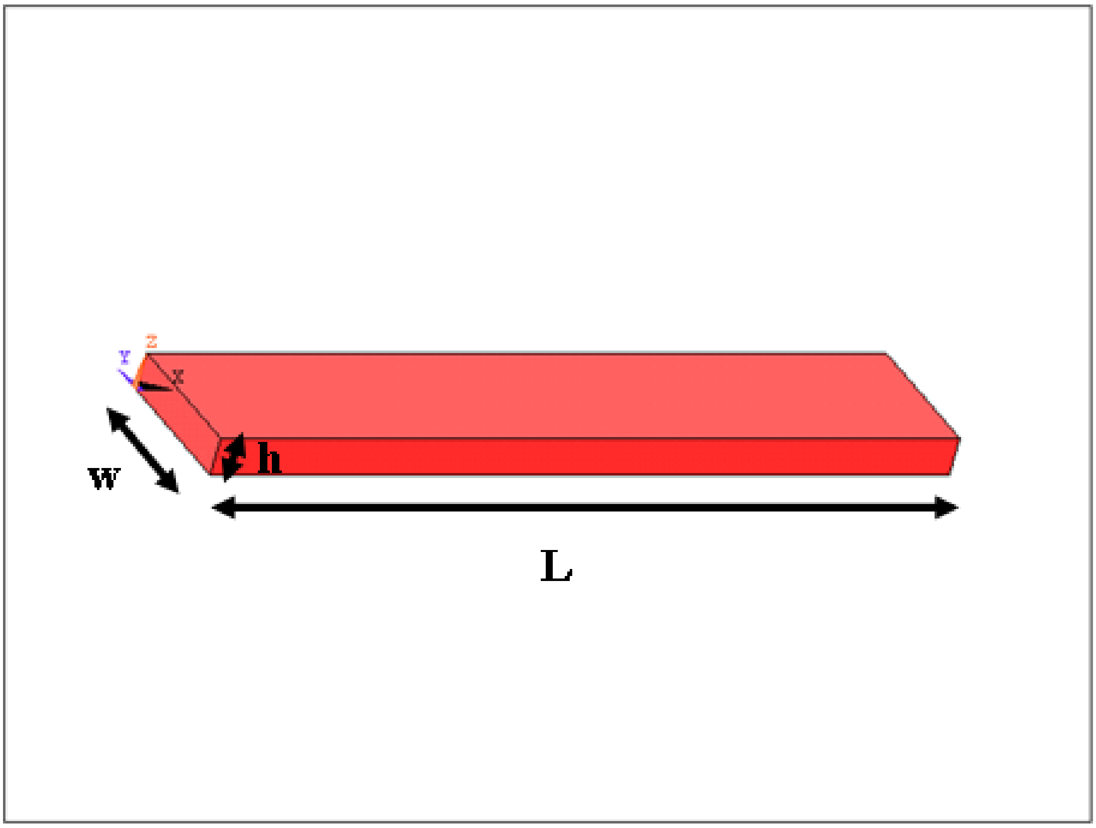

Figure 3.14: Sample cantilever beam used in nickel modulus of elasticity experiment (ANSYS model).

In the current layout, there are two copies for the same geometry which are located in different regions of the chip. These regions on the chip can be seen in Figure 3.15.

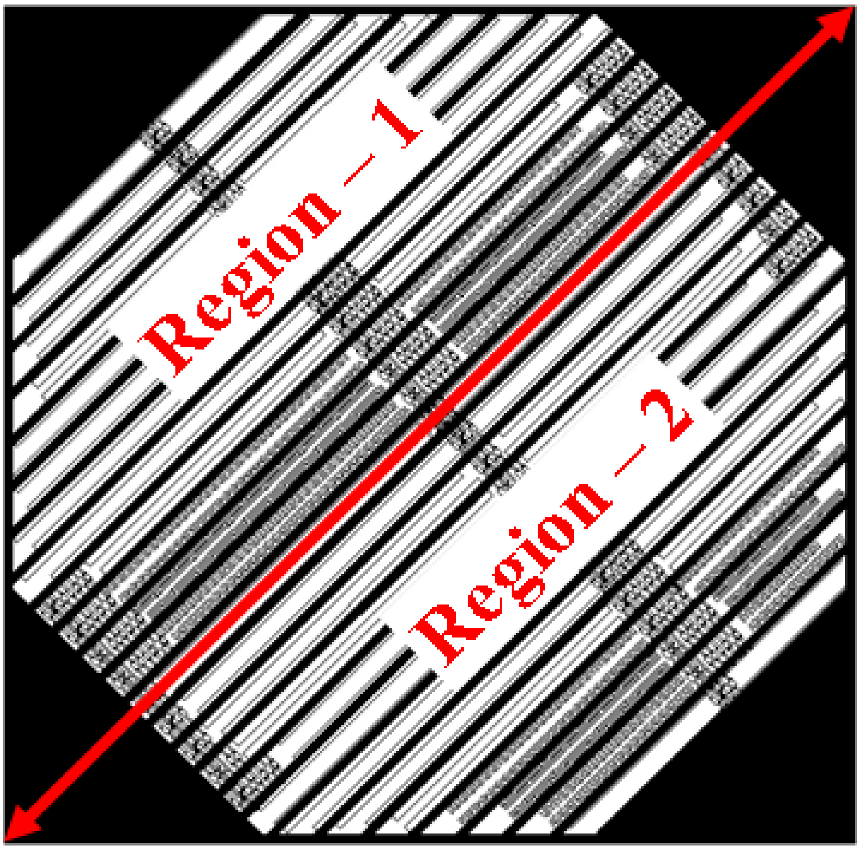

Figure 3.15: Different regions on the chip.

As a result of taking measurements for three different lengths six different modulus of elasticity values are found. Measuring three different cantilever types on two different regions on the chip gives six different modulus values. Two different values are found for 5x100, 5x75 and 5x50 type geometries, one for the Region – 1 cantilevers and the other for the Region – 2 cantilevers. Moreover, measured nickel thicknesses for each of these geometries are found as 0.820 and 0.888 μm for Region – 1 and Region – 2 of 5x100 geometry, 0.776 and 0.888 μm for Region – 1 and Region – 2 of 5x75 geometry, 0.728 and 0.899 μm for Region – 1 and Region – 2 of 5x50 geometry.

At the end, the average moduli of elasticity values of the measured cantilever beams are determined by using the Eqn. 3.2. Table 3.3 shows the final results of this experiment.

NICKEL MODULUS OF ELASTICITY TABLE					
Region – 1			**Region – 2**		
Beams	**Average Modulus of Elasticity (GPa)**	**Standard Deviation (x10^9) (GPa)**	**Beams**	**Average Modulus of Elasticity (GPa)**	**Standard Deviation (x10^9) (GPa)**
5 x 100	169.092	7.64	**5 x 100**	181.056	8.21
5 x 75	160.565	6.62	**5 x 75**	170.839	7.92
5 x 50	155.720	9.72	**5 x 50**	155.854	4.32
General	161.792	9.74	**General**	169.250	11.26
Final Average Modulus of Elasticity (GPa)			**165.521 (±10.49)**		

Table – 3.3: Nickel Modulus of Elasticity. (# of measurements: 70 for Region – 1, 49 for Region – 2)

It can be seen in Table 3.3 that 165.5 ± 10.5 GPa is found for the modulus of elasticity of the electro-plated nickel material. In previous studies [23, 25], 170.37 GPa and 159 GPa were found for the modulus of elasticity of the electro-plated nickel thin films. Hence, this result can be considered as reliable data because of being closer to what was found in the literature before.

For the calculations, the dimensions of the cantilevers are taken exactly same as the ones which are determined in the mask design. This situation foresees that there are no overdevelopment or underdevelopment problems during the photolithography step of the fabrication flow. This can be understood better with a one to one comparison between the positions of a micro-cantilever before and after fabrication. This comparison of a cantilever between its mask design initially, and its fabricated situation finally can be seen in Figure 3.16.

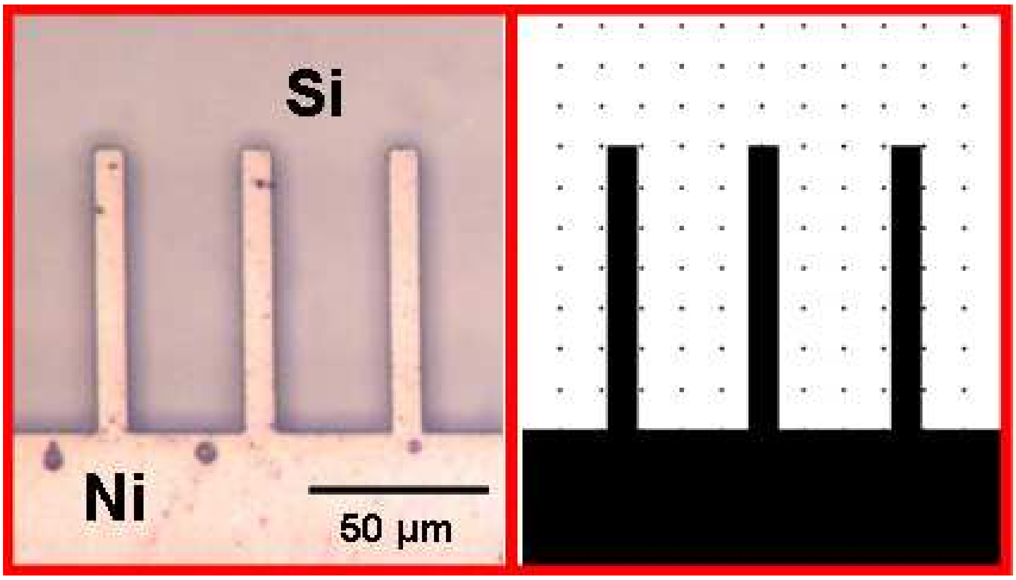

Figure 3.16: Size comparison between the fabricated cantilever having geometry of 7 µm x 70 µm and its L-edit design.

In addition to this, the density of the nickel material is taken as 8900 kg/m^3 which is the typical density value of nickel. Some studies on thin films also used this value as the density of the electro-plated nickel in their calculations [26]. However some other studies in the literature did not represent any information about the density of the nickel for their studies in order to calculate the electro-plated nickel modulus of elasticity [23, 25]. Hence, by accepting the density as a variable parameter, another term, which is $\sqrt{E/\rho}$, is obtained. In the literature, this term is considered as the speed of sound [59]. By using Eqn. 3.2 again, $\sqrt{E/\rho}$ term is also calculated. The results can be seen in Table 3.4.

NICKEL MODULUS OF ELASTICITY TABLE					
Region – 1			**Region – 2**		
Beams	**Average** $\sqrt{\frac{E}{\rho}}$ **(m / s)**	**Standard Deviation (m / s)**	**Beams**	**Average** $\sqrt{\frac{E}{\rho}}$ **(m / s)**	**Standard Deviation (m / s)**
5 x 100	4357.66	101.58	**5 x 100**	4509.40	102.24
5 x 75	4246.61	86.92	**5 x 75**	4380.15	101.24
5 x 50	4180.96	130.03	**5 x 50**	4184.32	57.91
General	4261.74	128.72	**General**	4357.95	145.72
Final Average $\sqrt{E/\rho}$ **(m / s)**			**4309.85** **(±137.20)**		

Table 3.4: $\sqrt{E/\rho}$ Term for Nickel Modulus of Elasticity. (# of measurements: 70 for Region – 1, 49 for Region – 2)

As it can be seen in Table 3.4, 4310 ± 137.2 m/s is found for the $\sqrt{E/\rho}$ term regarding the electro-plated nickel material.

3.4.2. Measurement of Gold Modulus of Elasticity

In micro-cantilever technology, gold layer is used to utilize the biological mass detection for a functionalized surface [41]. Hence, it can be said that gold is the most important material if the cantilever is used for biological applications. Depending on the amount of gold deposition, the resonance frequency would change as dictated by Eqn. 3.4.

As it was stated in Section 3.3, the resonance frequencies of double-layered nickel-gold cantilevers are measured with a Laser-PD setup. The resonance frequency measurements are carried out under ambient temperatures similar as the nickel modulus of elasticity experiment. The thickness of the sputtered gold material is taken as 100 nm. Furthermore, the nickel layer thicknesses of the double-layered cantilever beams are measured with Veeco® DEKTAK 8 Surface Profiler Machine in the Clean Room.

In this experiment, three different chips which include cantilevers having widths of 4 µm and 5 µm, and aspect ratios of 5 are used. This makes the length of the cantilevers as 20 µm and 25 µm, respectively. These chips also have two copies for the same geometry which are located in different regions of the chip same as the chip used for the previous experiment. Furthermore in this experiment, the cantilevers having grating structures at their tips are used. The grating geometry of the cantilevers is defined as “IZ33” which determines the width and length of the grating part as 35 µm and 18 µm. Inside the grating, there are 2 square-openings with a side length of 3 µm, and 3 rectangle-openings with side lengths of 3 µm and 15 µm. In Figure 3.17, the schematic view of a cantilever with a grating structure at its tip can be seen.

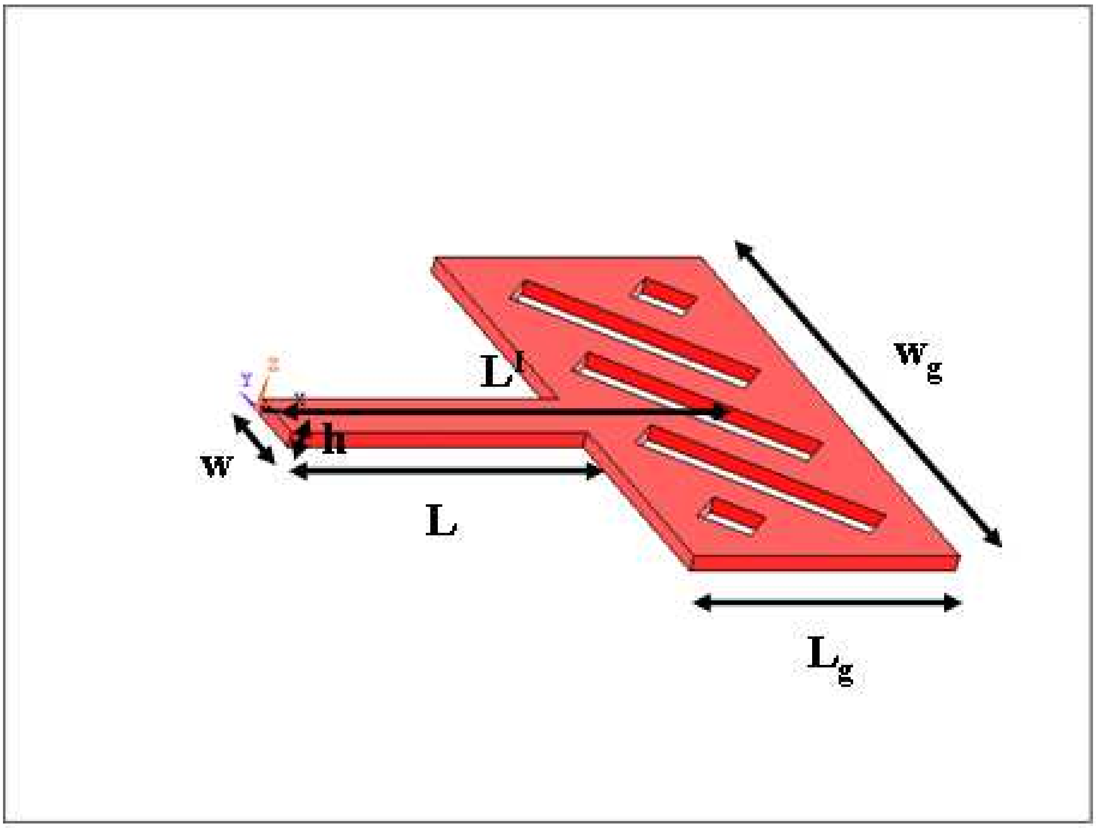

Figure 3.17: Sample cantilever beam used in gold modulus of elasticity experiment (ANSYS model).

As a result of doing measurements for three different chips six different gold modulus of elasticity values are found again. Two different values are found for 4x20IZ33, 5x25IZ33(a) and 5x25IZ33(b) type geometries, one for the Region – 1 cantilevers and the other for the Region – 2 cantilevers. Moreover, measured nickel thicknesses for each of these geometries are found as 1.853 and 2.102 µm for the Region – 1 and Region – 2 of 4x20IZ33 geometry, 0.981 and 1.109 µm for the Region – 1 and Region – 2 of 5x25IZ33(a) geometry, 1.391 and 1.287 µm for the Region – 1 and Region – 2 of 5x25IZ33(b) geometry.

For the calculations, the density values of the nickel and gold materials are taken as 8900 kg/m^3 and 19300 kg/m^3 which are the typical density values of nickel and gold. Some previous studies also used 19300 kg/m^3 as the density of gold for modulus of elasticity calculations [24, 28, 57]. Furthermore, the modulus of elasticity for the electro-plated nickel material is taken as 165 GPa which was found in the previous study. In addition to these, the dimensions of the cantilevers with grating structures at their tips are taken exactly same as the ones which are determined in the mask design. The comparison of this cantilever type between its mask design initially, and its fabricated situation finally can be seen in Figure 3.18.

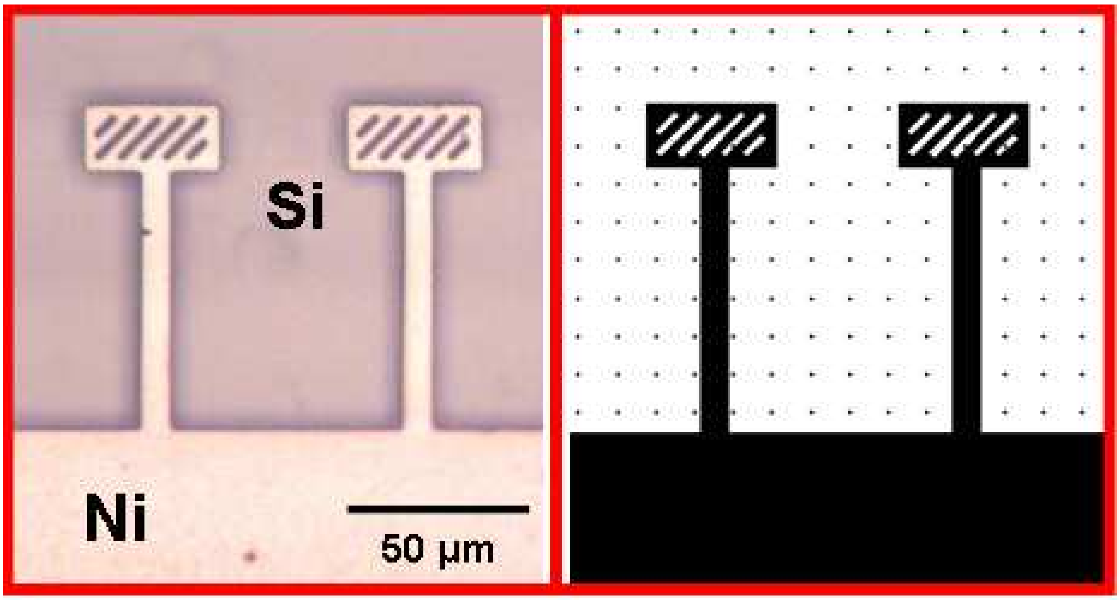

Figure 3.18: Size comparison between the fabricated cantilever having geometry of 7 µm x 70 µm and its L-edit design.

At the end, the average moduli of elasticity values of the measured cantilever beams are determined by using Eqn. 3.5. Table 3.5 shows the final results of this experiment.

<table>
<tr><th colspan="6">GOLD MODULUS OF ELASTICITY TABLE</th></tr>
<tr><th colspan="3">Region – 1</th><th colspan="3">Region – 2</th></tr>
<tr><th>Beams</th><th>Average Modulus of Elasticity (GPa)</th><th>Standard Deviation (x10⁹) (GPa)</th><th>Beams</th><th>Average Modulus of Elasticity (GPa)</th><th>Standard Deviation (x10⁹) (GPa)</th></tr>
<tr><td>4x20IZ33</td><td>42,43</td><td>30,31</td><td>4x20IZ33</td><td>48,85</td><td>47,68</td></tr>
<tr><td>5x25IZ33 (a)</td><td>35,22</td><td>18,49</td><td>5x25IZ33 (a)</td><td>70,28</td><td>37,72</td></tr>
<tr><td>5x25IZ33 (b)</td><td>26,20</td><td>9,33</td><td>5x25IZ33 (b)</td><td>68,50</td><td>49,01</td></tr>
<tr><td>General</td><td>33,80</td><td>20,03</td><td>General</td><td>67,37</td><td>43,53</td></tr>
<tr><td colspan="3">Final Average Modulus of Elasticity (GPa)</td><td colspan="3">53,75
(±39,37)</td></tr>
</table>

Table 3.5: Gold Modulus of Elasticity. (# of measurements: 28 for Region – 1, 41 for Region – 2)

It can be seen in Table 3.5 that 53.75 ± 39.37 GPa is found for the modulus of elasticity of the sputtered gold material. In Figure 3.19, Scanning Electron Microscope (SEM) image of the bottom surface of a fabricated double-layered cantilever which is similar with the one used in this study can be seen. In order to take the bottom side image of the cantilevers, nickel surface on the chip is peeled off with a scotch tape. Hence, the bottom side of the chip is viewed. In the chip, cantilevers are 5 μm in width.

By looking at Figure 3.19, the reason for obtaining a high standard deviation with respect to the average gold modulus value can be understood. The calculations can deviate because the structure of gold layer changes during the fabrication. This change can be seen as an undercut phenomenon in the sides of the gratings, cantilever and the anchor.

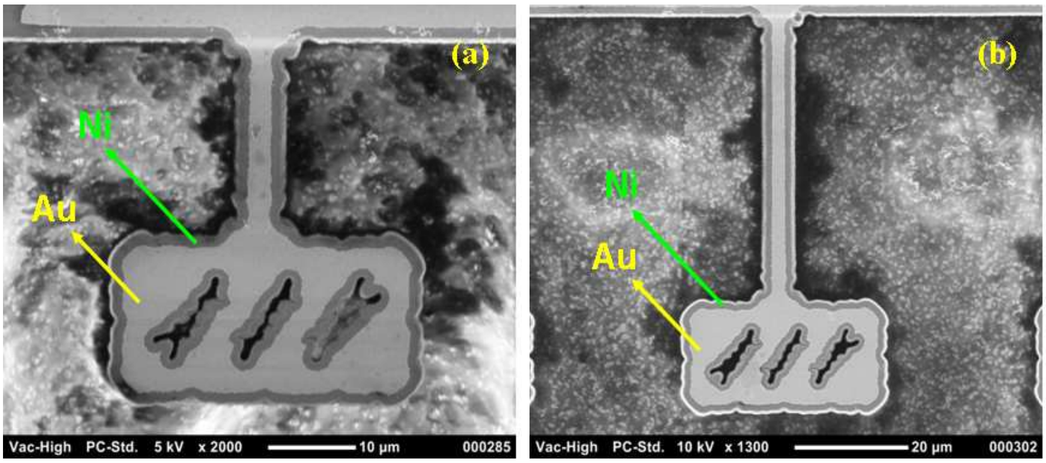

Figure 3.19: SEM images of a fabricated cantilever: a) 5 µm-width cantilever having a length of 25 µm, b) 5 µm-width cantilever having a length of 50 µm.

In previous studies [24], a range between 53 GPa and 130 GPa was found for the modulus of elasticity for thin gold films. Hence, although the standard deviation is found relatively bigger with respect to the actual average value, the result can be considered as consistent data by considering previous studies.

3.4.3. Measurement of Chromium Modulus of Elasticity

In micro-cantilever technology, chromium layer also has an important role because of improving the adhesion of gold layer [40]. Therefore the mechanical properties of chromium material should be carefully investigated in order to include its effect to the resonance frequency of the whole thin film. In this part, one of the important mechanical properties of chromium, which is modulus of elasticity, is investigated with resonance frequency method.

As it was stated in Section 3.3, the resonance frequencies of triple-layered nickel-gold-chromium cantilevers are measured with a Laser-PD setup. The resonance frequency measurements are carried out under ambient temperatures as in the previous experiments. The thicknesses of the sputtered gold and chromium materials are taken as 100 nm for gold and 20 nm for chromium. Furthermore, the nickel layer thicknesses of the cantilever beams are measured with Veeco® DEKTAK 8 Surface Profiler Machine in the Clean Room.

In this experiment, a chip which includes cantilevers having widths of 4 µm, and aspect ratios of 5 are used. This makes the length of the cantilevers as 20 µm. These chips also have two copies for the same geometry which are located in different regions of the chip same as the chips used for the previous experiments. Moreover, the cantilevers have also "IZ33" grating geometry at their tips same as the cantilevers used in gold modulus of elasticity experiment.

As a result of doing measurements for the cantilevers in this chip two different chromium modulus of elasticity values are found for 4x20IZ33 type geometry, one for the Region – 1 cantilevers and the other for the Region – 2 cantilevers. Moreover, measured nickel thicknesses for this geometry are found as 0.815 and 0.804 µm for the Region – 1 and Region – 2 of 4x20IZ33 geometry.

For the calculations, the density values of the nickel, gold and chromium materials are taken as 8900 kg/m^3, 19300 kg/m^3, 7140 kg/m^3 which are the typical density values of nickel, gold and chromium. Some previous studies also used 7140 kg/m^3 as the density of chromium for modulus of elasticity calculations [24]. Moreover, the modulus of elasticity values for electro-plated nickel and sputtered gold materials are taken as 165 and 53 GPa which were found in the previous experiments.

At the end, the average moduli of elasticity values of the measured cantilever beams are determined by using Eqn. 3.7. Table 3.6 shows the final results of this experiment for 20 nm sputtered chromium thickness.

<table>
<tr><th colspan="6">CHROMIUM MODULUS OF ELASTICITY TABLE</th></tr>
<tr><th colspan="3">Region – 1</th><th colspan="3">Region – 2</th></tr>
<tr><th>Beams</th><th>Average Modulus of Elasticity (GPa)</th><th>Standard Deviation (x10⁹) (GPa)</th><th>Beams</th><th>Average Modulus of Elasticity (GPa)</th><th>Standard Deviation (x10⁹) (GPa)</th></tr>
<tr><td>4x20IZ33</td><td>66,39</td><td>14,81</td><td>4x20IZ33</td><td>67,61</td><td>17,45</td></tr>
<tr><td colspan="3">Final Average Modulus of Elasticity (GPa)</td><td colspan="3">66,99
(±16,03)</td></tr>
</table>

Table 3.6: Chromium Modulus of Elasticity (for 20 nm sputtered chromium thickness) (# of measurements: 30 for Region – 1, 29 for Region – 2)

It can be seen in Table 3.6 that 67 ± 16 GPa is found for the modulus of elasticity of the sputtered chromium material with 20 nm thickness. In this experiment, it is assumed that no oxidation occurs on the chromium surface and the obtained value for the modulus of elasticity is for the thin chromium film. In previous studies [24, 29], a wide range between 107 GPa and 275 GPa was obtained for the sputtered thin chromium films. But, as the thickness of the chromium layer decreases to “nm” range, it is seen that the modulus of elasticity is found between 40 GPa and 70 GPa. Hence, because of having nm-thickness, this result can also be considered as compatible data when compared with previous studies.

Furthermore, since different chips are used for gold modulus of elasticity experiment and chromium modulus of elasticity experiment, more amount of standard deviation obtained for gold modulus with respect to chromium modulus can be considered acceptable. There may be a problem with the chip used for the gold modulus experiment during fabrication.

3.5. Reliability Study

It is a critical question whether the resonance frequency of a cantilever is stable or it changes over time. Even if the resonance frequency changes, what factors can be effective for this situation? In the previous studies on the effect of environment to the resonance frequency and usability of a micro-cantilever, it was shown that relative humidity and temperature can cause significant changes in the resonance frequency [60, 61]. It is also known that there are many micro-cantilever type and MEMS-based structures in the commercial arena which is used for determining the relative humidity and temperature of an environment. However, these devices are not working with respect to the change in the resonance frequency of the cantilever beams. The beam is coated with a polyimide sensing film which is sensitive to humidity; this film absorbs the water vapor on the environment. As a result of this, the cantilever beam deflects and there occurs a capacitance, resistance or conductivity change on the beam surface. Hence, relative humidity or temperature can be measured with these devices [7, 62, 63].

In spite of the previous studies, the effect of environment can change from sample to sample. And as a result of the lack of the information obtained from the literature, an experiment is decided to be conducted for investigating the effect of relative humidity and temperature to the resonance frequency. With this experiment, the long term effect of the working environment on the resonance frequency will be investigated unlike the studies performed in the literature for searching the short term effect. In that manner, two different chips are prepared for the measurements. The chips are composed of double-layered nickel and gold cantilevers which have bridge (both-end-fixed) structures with a width of 7 and 8 μm. The sample view of these kinds of structures can be seen in Figure 3.20.

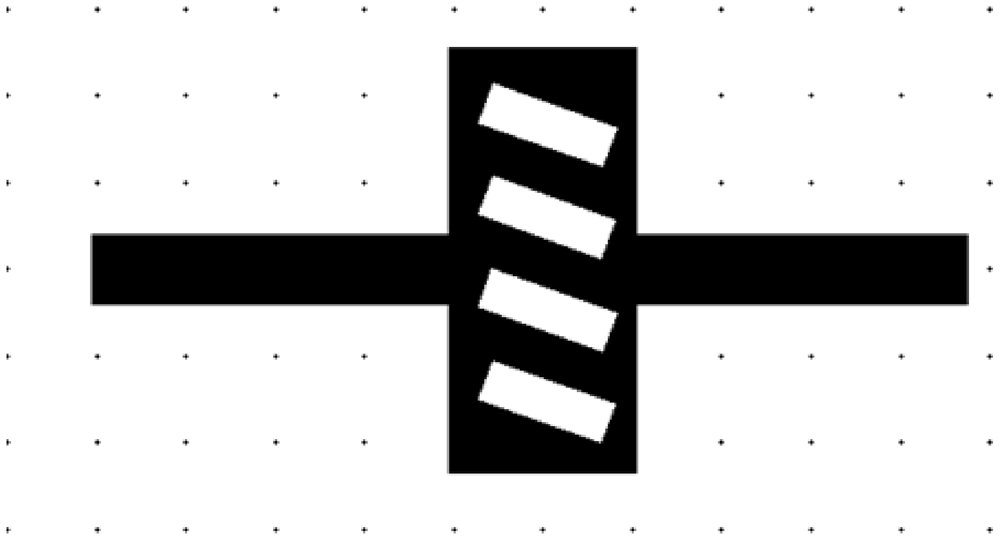

Figure 3.20: Sample bridge-structured cantilever beam used in Reliability Study.

The measurements are performed with the optical readout setup (Laser – PD) under ambient temperatures on three different geometries with aspect ratios as 10, 15 and 20. Hence, six different graphs are obtained for 7x70IZ53, 7x105IZ53, and 7x140IZ53; 8x80IZ53, 8x120IZ53 and 8x160IZ53 type geometries. At the beginning of this experiment, it was thought to repeat the measurements every month. But because of working in other projects, five measurements can be performed on the same cantilever beams. The results of this experiment can be seen as in the following graphs.

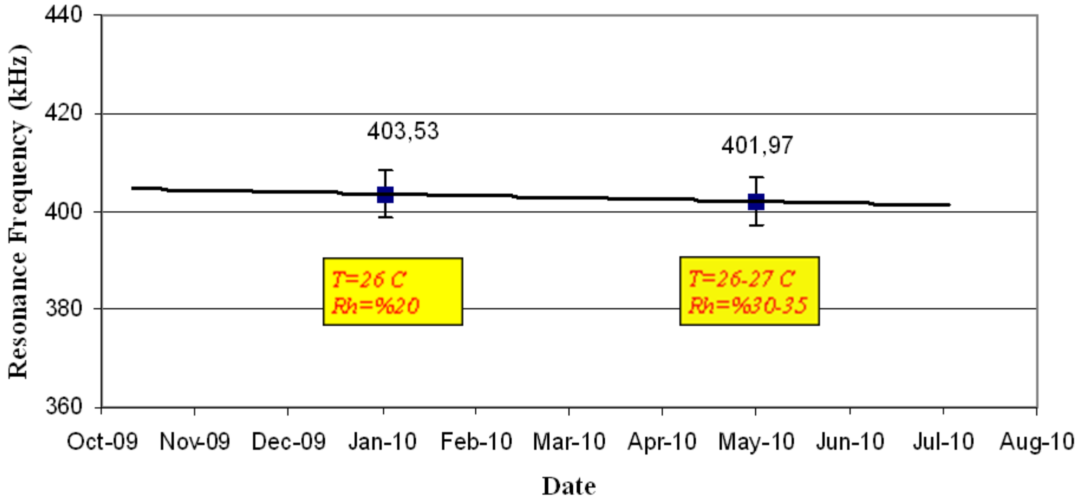

Figure 3.21: Resonance frequency variation with respect to the environmental factors. (for 7x70IZ53 type geometry.) (# of measurements: 10)

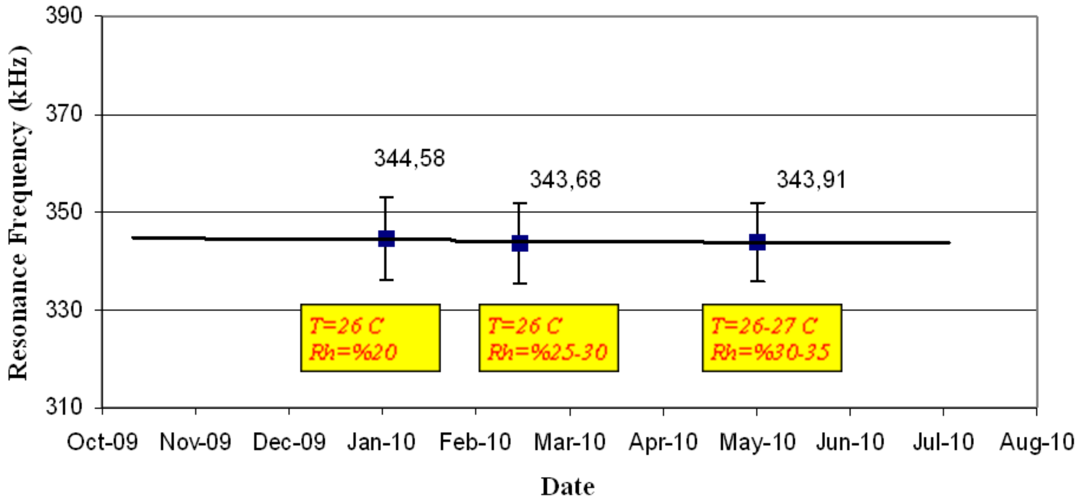

Figure 3.22: Resonance frequency variation with respect to the environmental factors. (for 7x105IZ53 type geometry.) (# of measurements: 20)

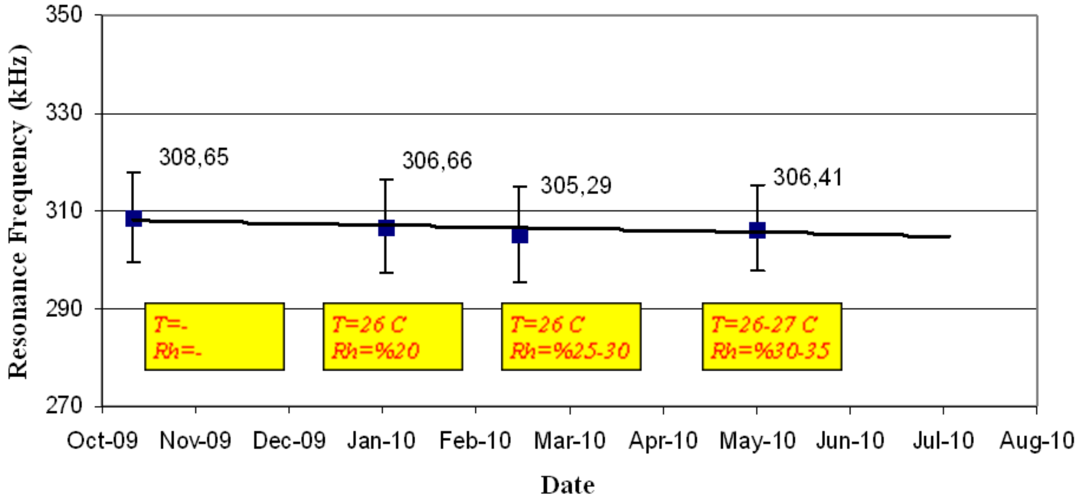

Figure 3.23: Resonance frequency variation with respect to the environmental factors. (for 7x140IZ53 type geometry.) (# of measurements: 20)

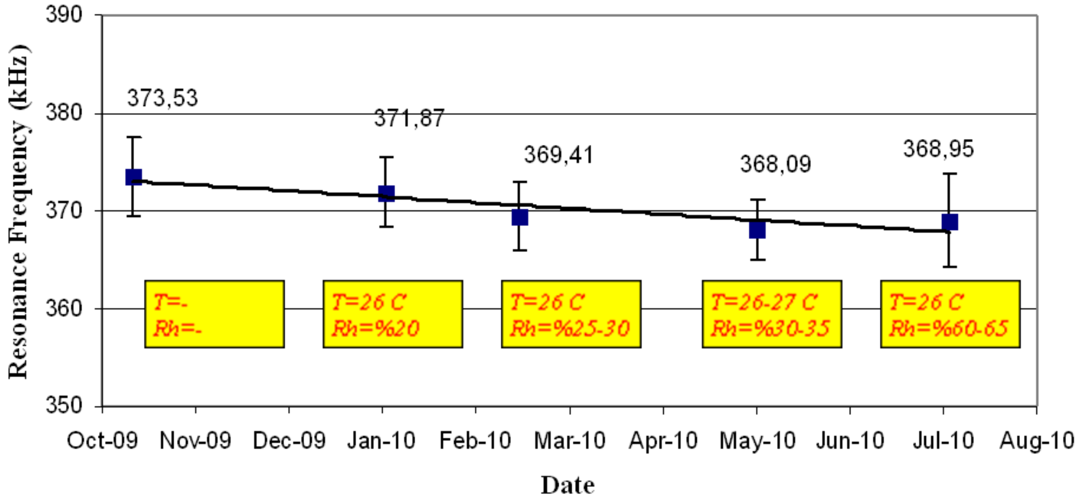

Figure 3.24: Resonance frequency variation with respect to the environmental factors. (for 8x80IZ53 type geometry.) (# of measurements: 20)

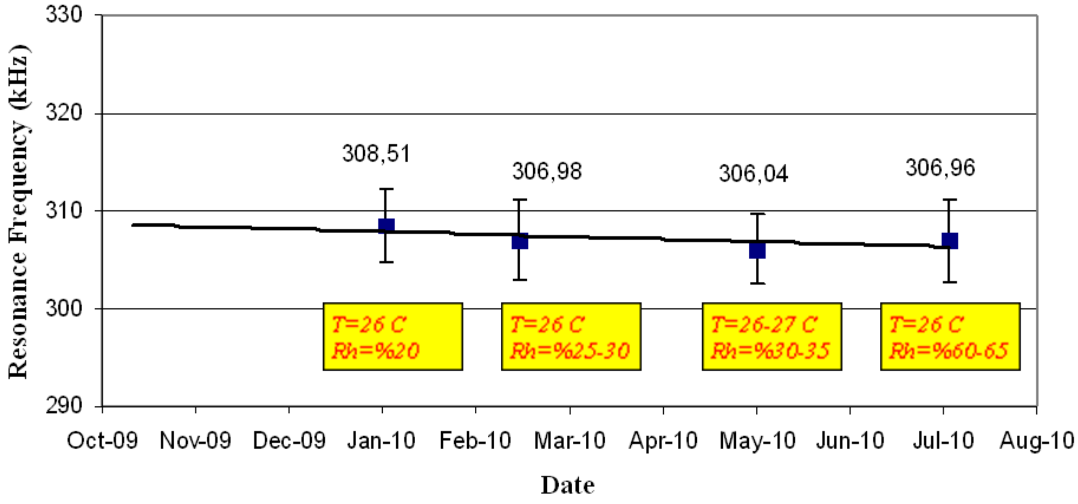

Figure 3.25: Resonance frequency variation with respect to the environmental factors. (for 8x120IZ53 type geometry.) (# of measurements: 16)

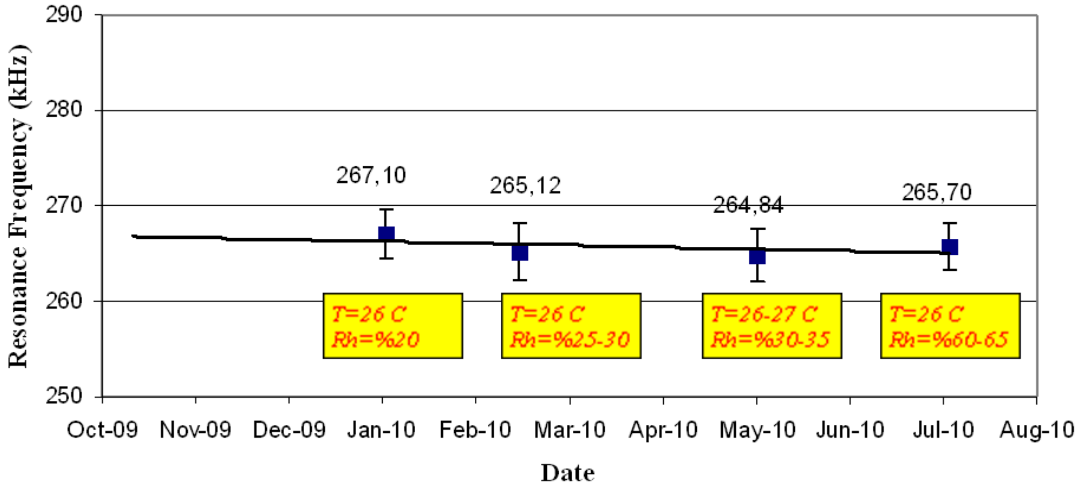

Figure 3.26: Resonance frequency variation with respect to the environmental factors. (for 8x160IZ53 type geometry.) (# of measurements: 15)

In the graphs, it can be seen that some of the measurements can not be made for every month as a result of the lack of reliable data. For the experiment result, there is generally a decreasing trend in the resonance frequency. It is also interesting that temperature stays almost constant at 26-27°C between the measurements, however it is possible to see an increase in relative humidity from 20 % up to 65 %. On the other hand, at the beginning of measurements as humidity increases from 20 % to 35 %, resonance frequency decreases; but at the end of measurements as humidity increases from 35 % to 65 %, resonance frequency increases.

Furthermore, the change in the resonance frequency is around 1-2 kHz at most. This can be normal by looking at the time range which is in months. Also, it is important to say that after a 10-month period the cantilevers start to lose their magnetic actuation characteristics which cause the corruption of signal.

In some of the previous studies [60, 61], the effect of relative humidity and temperature to the resonance frequency was illustrated explicitly. The relative humidity was accepted as a damping factor in the environment for the resonance frequency measurements [61]. Therefore this effect can cause a negative shift in the resonance frequency of a cantilever beam. Furthermore, some experiments showed that there is an inversely proportional relationship between the resonance frequency and the environmental factors. As the relative humidity or temperature increases, resonance frequency decreases; and as the relative humidity or temperature decreases, resonance frequency increases. The change in the resonance frequency is in “Hz” range with respect to the minute and hour change in time. Also, temperature affects the resonance frequency much more than relative humidity [60]. Moreover, some studies emphasized the corrosion effect due to relative humidity about the performance of the electronic components which directly affect the magnetic characteristics of these devices. Although micro-cantilevers are coated with electro-plated nickel for corrosion resistance, galvanic corrosion can be seen between two dissimilar metals when they are coupled together. In addition to this, the rate of corrosion increases during power-down or storage periods between measurements [64].

In conclusion, it will not be incorrect to say that these results partly support previous studies [60, 61] which were done about the effects of environmental factors. The inversely proportional relationship between the resonance frequency and the environmental factors is also seen in some parts of Reliability Study. But, it is important to say that the decrease in resonance frequency is within the standard deviation (0.5-1 % change at most) which means there is a stable manner in general. In addition to this, if the general distribution of whole data is carefully investigated, it will be seen that it is difficult to get a reasonable conclusion. Since there is an inconsistency between the rate of change of resonance frequency and relative humidity, a conclusion about environmental factors can be misleading. Furthermore, since the effect of humidity to corrosion is not obvious, a conclusion about this factor can not be made either.

Chapter 4 - CONCLUSION & FUTURE WORK

4.1. Conclusion

In this thesis, the micro-cantilever resonators which will be used for biological experiments are investigated mainly in two aspects: fabrication and mechanical properties. Firstly, the general fabrication flow for these specific micro-cantilevers is presented with problems occurring during this operation. The problems are generally encountered during etching and release, which is one of the most important steps of fabrication. Being the last step of fabrication flow makes etching and release step even more critical. As a result of this, some improvements are made either by changing the chemicals used or by replacing some sub-steps with new ones. At first, the way of quenching the biosensor chip after the silicon etching step is modified. As a result of this, the surface roughness of etched silicon layer decreased from 50-100 nm to 15-30 nm, and bending and sticking problems for long cantilevers are prevented. In addition to this, the chemical used for the etching of gold layer underneath the nickel layer is changed from Transene Inc. GE-8148® to Aqua Regia. Therefore the precipitation formation on the cantilevers after the etching of gold layer underneath the nickel layer is prevented. It can be seen that both of these changes give relatively better results. Moreover, photolithography and development steps in the fabrication flow are improved as a result of calibration experiments. As a result of this, the ability to obtain smaller critical lengths down to 2 μm is achieved. Finally, these improvements increased the fabrication yield and reliability of micro-cantilevers.

Furthermore, a new photolithography mask is designed, so that the range of experiments is extended with various cantilever designs. The new mask is tested both on silicon and SOI wafers. As expected, the surface underneath the cantilevers becomes smoother with the use of SOI wafer. The surface roughness underneath the cantilevers is decreased from 15-30 nm to 0.5-5 nm. Improved surface roughness is expected to give better results in the resonance frequency measurement setup as a result of increasing the quality of the reflected laser light from this surface.

Moreover some characterization of electro-plating process is carried out to study deposition parameters. The experiments are controlled by changing the current density and time. As a result of these experiments, some data are obtained in addition to the ones in the literature. It is shown that as the current density increases, nickel thickness and surface roughness also increase. Furthermore as deposition time increases, nickel thickness and surface roughness also increase. But this increase saturates gradually after 1500 nm and 30 minutes under specific conditions indicating that the relationship between deposition time and nickel thickness is linear at the beginning and turns into a logarithmic behavior afterwards. In addition to these, it is seen that there is a linear relationship between nickel thickness and surface roughness, and the effect of nickel thickness to surface roughness is much more prevailing than the effect of current density. In the final characterization experiment, it is observed that the surface roughness is stabilized between 10 nm and 20 nm for 1000 nm nickel thickness.

The second aspect of this thesis is aimed to investigate the measurement of mechanical properties of materials which are used in the micro-cantilever fabrication process by using the resonance technique. Hence, the materials used in the fabrication flow of a micro-cantilever are taken into consideration. The modulus of elasticity values for electro-plated nickel, and sputtered gold and chromium materials are obtained experimentally by using different micro-cantilever structures. 165.5 ± 10.5 GPa, 53.75 ± 39.37 GPa and 67 ± 16 GPa are measured for the modulus of elasticity values of thin nickel, gold and chromium films, respectively. Moreover, the effect of micro-cantilever design including length and thickness on the resonance frequency is explained. Expected relationships are obtained, i.e. resonance frequency changes linearly with cantilever thickness, and resonance frequency changes with inverse square of cantilever length.

Finally, a long term experiment is carried out both for observing the behavior in the resonance frequency of a both-end-fixed and double-layered nickel-gold micro-cantilever in different environmental conditions, and for observing its endurance limit. The experiment is carried out for a 10-month period in an environment having a constant temperature around 26-27°C, but a changing relative humidity between 20 % and 65 %. In this experiment, it is observed that the resonance frequency changed during the experiment. However, the change is not in a stable fashion, it is sometimes decreasing and sometimes increasing with increasing relative humidity. Furthermore, a discrepancy between the rate of change of resonance frequency and relative humidity is observed. In addition to this, the effect of humidity to corrosion of nickel and gold materials can not be fully understood. According to these results, it is concluded that it would be incorrect to establish a relationship between resonance frequency and environmental factors.

In the appendix, some other experiments and fabrication flows are presented. The experiments include the wet etching of ZnSe crystal; wet etching of whole 4" silicon wafer for wagonwheel formation; and wet etching of ITO samples. These extra studies give the opportunity of working with different substrates, chemicals and processes for different purposes.

In conclusion, this thesis can be a helpful source for the research which will be conducted for investigating the fabrication and characterization of specific micro-cantilever resonators. Continuously developing technology in this area will cause these devices to be used for many other applications. Therefore it is critical to understand details about the working principle and structure of micro-cantilevers for their effective use in every area. In that manner, this thesis investigated the fabrication issues and structural characteristics of specific micro-cantilevers with different characterization experiments, calculations, measurement setups and fabrication flows.

4.2. Future Work

The production of a micro-cantilever requires a long fabrication period with use of many chemicals and materials. In this thesis, many fabrication processes are carried out with two different layouts. As a result of these fabrication processes, around 100 samples are produced for different applications. Furthermore, mechanical properties of the critical materials used in these samples are obtained. However in spite of these achievements, some additional steps remain unaccomplished as future works.

First of all, starting to work with a quarter wafer for electro-plating and etching steps is an important development presented in this thesis. However, it will not be enough for proceeding to the next level which is the fabrication work performed with the functionalization mask in the 2nd Generation Layout. Since 2nd Generation Layout requires two masks, whole 4" wafer should not be separated without finishing the fabrication work with both masks as mentioned in Section 2.3.1. In order to achieve this, as done with the quarter wafer, whole wafer should be electro-plated at once. Hence, a new setup should be integrated into the nickel sulphamate bath. The design of this setup is finished. As the manufacturing of the setup is completed, the electro-plating process of the whole wafer can be achieved. Moreover with the help of this new setup, the temperature of the electro-plating solution can be controlled in a better way.

In addition to this, because of not electro-plating the whole wafer, it is not possible to work with the functionalization mask. For biological experiments, same fabrication procedure is applied as performed by using the previous layout. With the usage of functionalization mask in the 2nd Generation Layout, different biological experiments can be carried out as a result of having the ability of binding molecules in different places. Furthermore, it will be relatively easier to monitor the placement and situation of biological molecules on the cantilever surfaces because of having the functionalization layer above.

Finally, the proposed methodology for the measurement of the modulus of elasticity of thin film materials can be applied to other materials in a more systematic way in order to study the scale-effect in mechanical properties.

With the completion of these future works, the aim of this thesis will be met and a contribution to micro-cantilever technology will be achieved.

APPENDIX A – PROCESS DEVELOPMENT

This appendix summarizes process development and fabrication work carried out on alternative substrates such as Zinc Selenide (ZnSe) crystal and on Indium Tin Oxide (ITO), and on silicon wafer by using different solutions.

In the first fabrication work, the etching behavior of a ZnSe crystal is observed inside a solution which is composed of Potassium permanganate ($KMnO_4$), Sulfuric Acid (H_2SO_4) and DI water, and the etch rate of this solution is figured out for the crystal experimentally.

In the second fabrication work, a specifically patterned 4" wafer is etched in a solution which is composed of KOH and DI water in order to obtain an alignment mark.

In the third and final fabrication work, ITO samples are etched inside HCl and DI water solution after being patterned with a specific photolithography mask.

A1. Zinc Selenide (ZnSe) Crystal

In this study, since etch rate of the $KMnO_4$, H_2SO_4 and DI water solution is tried to be figured out; a protective material should be found. Hence, while the protected region is kept safe from being etched, the other region will be etched and the etch rate can be determined with that way. As a result of this, AZ-5214® type photoresist is selected as the protective material. However, since the solution used in this study is a harsh solution, it is thought that it will also etch the photoresist and this etch rate should also be determined. The steps performed in this fabrication process can be seen as follows [For Step definitions refer to Figure A.2.];

1) A 22 mm x 22 mm cover glass piece is cleaned in acetone and Isopropyl Alcohol (IPA) chemicals, respectively.
2) The sample is coated with AZ-5214® type photoresist in the spinner machine and soft-baked on a hot plate at 110°C for 10 minutes.
3) Half of the photoresist on the glass sample is stripped off manually by using acetone. (Thickness of photoresist is measured with Veeco® DEKTAK 8 Surface Profiler.)
4) The glass piece is placed in 20:2:1 $KMnO_4$:H_2SO_4:DI water solution for 3 minutes. (Thickness of photoresist is measured after this step again, and it is seen that the solution etches photoresist as it is expected. The etch rate of the solution for photoresist is recorded.)
5) ZnSe crystal is cleaned in acetone and IPA chemicals, respectively.
6) The sample is coated with AZ-5214® type photoresist in the spinner machine and soft-baked on a hot plate at 110°C for 10 minutes.
7) Half of the photoresist on the crystal surface is stripped off manually by using acetone. (Thickness of photoresist is measured with Veeco® DEKTAK 8 Surface Profiler.)

8) The crystal is placed in 20:2:1 $KMnO_4$:H_2SO_4:DI water solution for 3 minutes. (Thickness between photoresist and crystal is measured again and by using the photoresist etch rate which is found in the previous process as the reference value (Step#4), the etch rate of this solution of the ZnSe crystal is found out.)

In Figures A.1 and A.2, ZnSe crystal used in this experiment and the schematic view of the whole fabrication process used in this experiment can be seen.

Figure A.1: ZnSe crystal after being etched in the $KMnO_4$, H_2SO_4 and DI water solution.

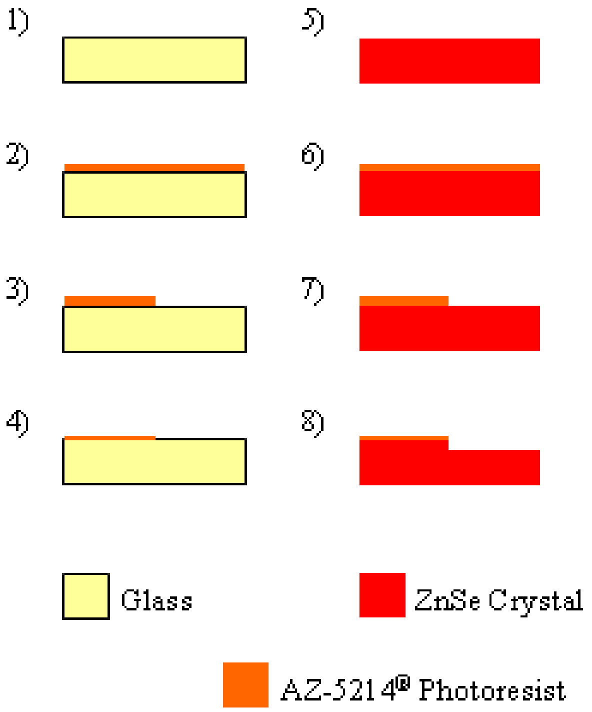

Figure A.2: Schematic view of the fabrication flow used in ZnSe crystal etching rate experiment.

As a result of this experiment, some etching rate values are obtained for the $KMnO_4$, H_2SO_4 and DI water solution. However, the values are not compared well with those repeated in the literature. In the previous studies which were performed about this subject, the etch rates were found as 0.56916 μm/min for 20:2:10 $KMnO_4$:H_2SO_4:DI water solution and 1 μm/min for 20:2:8 $KMnO_4$:H_2SO_4:DI water solution [65]. It can be seen that the etch rate increases with decreasing amount of DI water in the solution. However in this study, obtained etch rate for 20:2:1 $KMnO_4$:H_2SO_4:DI water solution is 17 nm/min. In spite of removing the amount of DI water completely in the solution, obtained etch rate is found as 120-200 nm/min which is too under with respect the results obtained in the literature. But the surface of ZnSe crystal is damaged at the end of whole fabrication work as seen in Figure A.1 which prevents getting healthy results. Furthermore, there have seen cracks on the photoresist surface. In conclusion, it is understood that photoresist is not a suitable protective material for ZnSe crystal in the etching solution.

A2. Wagon Wheel

In this study, the main objective is to obtain membrane like structures on a whole 4" Silicon wafer. This process requires the usage of two photolithography masks which are designed by Sevilay Arslan. First mask has four wagon wheels on each corner as the alignment marks for the second mask. Second mask is the actual membrane mask for the production of membranes. Hence, this experiment consists of two processes with two masks, but because of the time limit only first process can be completed. In the first process, the aim is to obtain a wagon wheel structure on the wafer with the first mask. The steps performed in this fabrication process can be seen as follows [For Step definitions refer to Figure A.4.];

1) 4" wafer is coated with AZ-5214® type photoresist in the spinner machine and soft-baked on the hot plate at 110°C for 10 minutes. (The wafer is cleaned with HF chemical for removing the oxide layer on the silicon surface.)
2) The wagon wheel structure is patterned on the silicon wafer with photolithography and development processes. (Exposure: 15 seconds, Development: 10-15 minutes)
3) Silicon surface is covered with 50 nm of gold and 20 nm of chromium layers with RF sputtering method.
4) Wafer is placed in ultrasonic remover bath directly after RF sputtering, and lift-off process is applied. (As a result of this step, chromium and gold layers are removed from the silicon surface, but the layers on the wagon wheel parts are remained because of not having photoresist underneath.)
5) Wafer is placed in 35 % KOH solution and the silicon part around the wagon wheel is etched with a depth of 22.5-23.5 μm. (Wagon wheel structure remains above with respect to the silicon surface around it because of being protected with chromium and gold layers.)

6) Finally, remained chromium and gold layers are also etched and bulged wagon wheel structure is obtained as alignment mark for the second mask.

In Figures A.3 and A.4, wagon wheel structure fabricated in the experiment and the schematic view of the whole fabrication process used in the first process of this experiment can be seen.

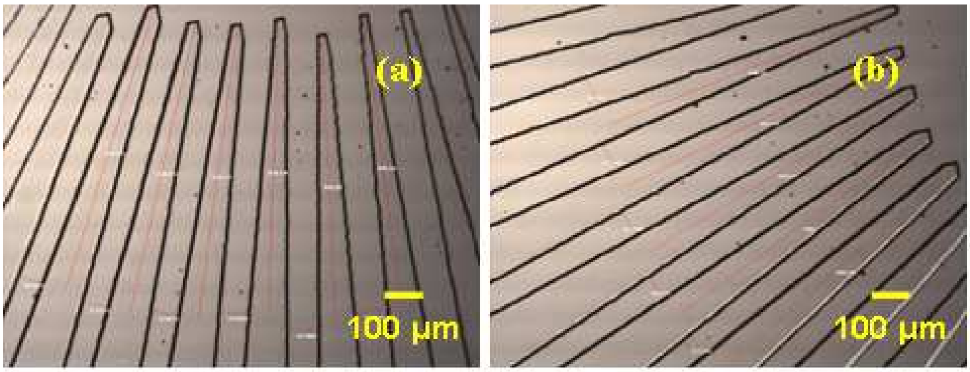

Figure A.3: Obtained wagon-wheel structure at the end of the experiment. (Red lines on Figure A.3(a) and A.3(b) show the deepened silicon surfaces with KOH solution.)

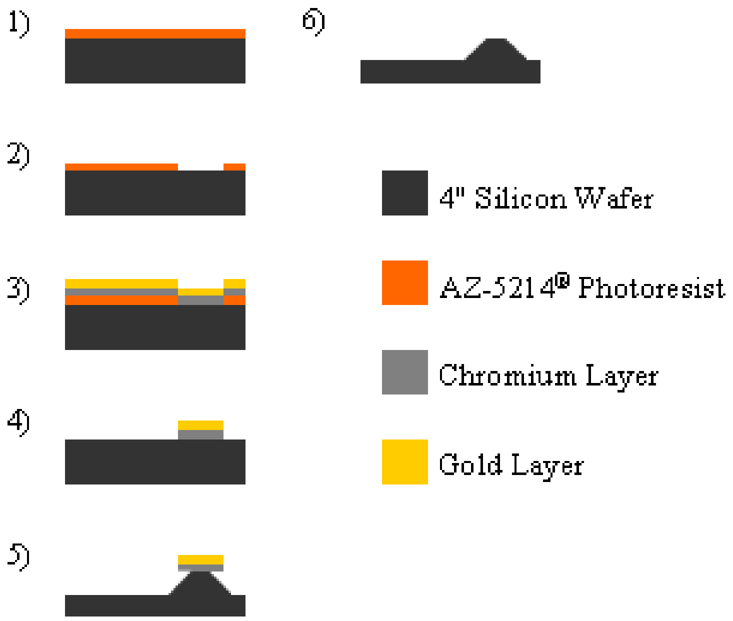

Figure A.4: Schematic view of the fabrication flow used in the wagon wheel experiment.

As a result of this fabrication work, first process of the experiment is completed and a wagon wheel structure is obtained on the silicon wafer. It is prepared for the second photolithography process.

A3. Indium Tin Oxide (ITO)

ITO substrates used in this fabrication work have 120 nm-thick ITO films on the cover glasses, and resistance is passing on these thin films. In this study, fabrication flow consists of one-mask photolithography process for the pattern formation on ITO samples. Since ITO substrates are etched inside HCl and DI water solution; as in the first fabrication work, a protective material is needed also in this work for preventing the solution from damaging the patterned ITO surfaces. As a result of this, AZ-5214® type photoresist is again selected as the protective material. The steps performed in this fabrication process can be seen as follows [For Step definitions refer to Figure A.5.];

1) ITO substrates are cleaned with acetone and IPA chemicals, respectively.
2) Substrates are coated with AZ-5214® type photoresist in the spinner machine and soft-baked on the hot plate at 110°C for 10 minutes.
3) ITO surface is specifically patterned on the ITO substrates with photolithography and development processes. (Exposure: 15 seconds, Development: 10-15 minutes)
4) Substrates are etched chemically in 1:1 HCl:DI water solution for 5 minutes. (In this step, it is known that the etch rate of this solution is 8 Å/sec [66]. And the substrates are kept inside the solution until being sure about unprotected ITO parts are gone completely.)
5) The ITO substrates are put inside remover solution for stripping the photoresist off. (Finally, electrical conductivity of the substrate surfaces is checked with a digital multimeter.)

In Figure A.5, the schematic view of the whole fabrication process used in this experiment can be seen.

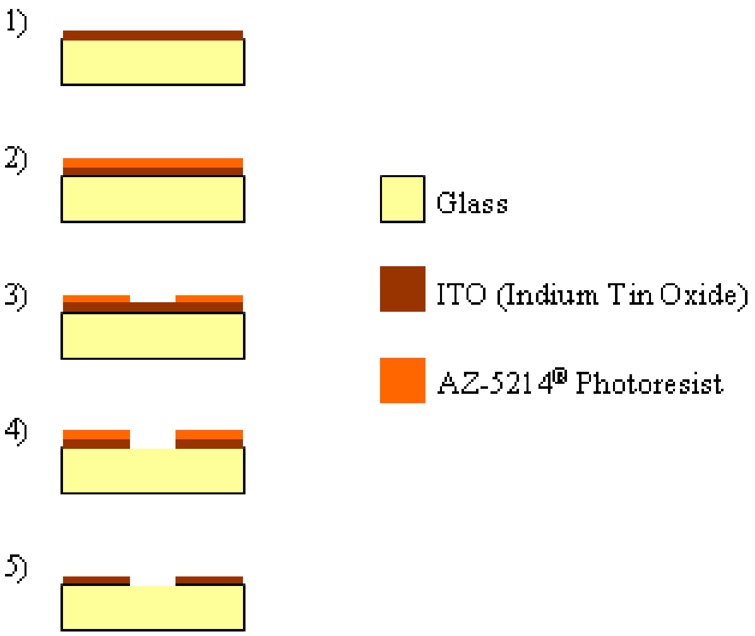

Figure A.5: Schematic view of the fabrication flow used in ITO experiment.

According to this experiment, it is tried to obtain ITO surfaces so that channels will form under the unprotected regions and ITO will remain under the protected regions. There is no electrical conductivity between the regions which are separated with these channels and electrical conductivity will be inside every protected ITO region. In conclusion, some successful samples are obtained in this study. But, it is clearly observed that photoresist is not a suitable protective material also for ITO films against the etching solution used in this fabrication work.

BIBLIOGRAPHY

1. *Electromechanical Monolithic Resonator*, United States Patent, 3614677, (1971).

2. Wilfinger R.J., Bardell P.H. and Chhabra D.S., *The Resonistor: A Frequency Selective Device utilizing the Mechanical Response of a Silicon Substrate*, IBM Journal of Research and Development, **12** (1), (1968), 113-118.

3. Ramos D., Calleja M., Mertens J., Zaballos A. and Tamayo J., *Measurement of the Mass and Rigidity of Adsorbates on a Microcantilever Senso*r, Sensors, **7**, (2007), 1834-1845.

4. Ansari M.Z., Cho C., Kim J. and Bang B., *Comparison between Deflection and Vibration Characteristics of Rectangular and Trapezoidal profile Microcantilevers*, Sensors, **9**, (2009), 2706-2718.

5. Raiteri R., Grattarola M., Butt H.J. and Skládal P., *Micromechanical Cantilever-Based Biosensors*, Sensors and Actuators B, **79**, (2001), 115-126.

6. Zhu Y., Barthelat F., Labossiere P.E., Moldovan N. and Espinosa H.D., *Nanoscale Displacement and Strain Measurement*, Proceedings of the 2003 SEM Annual Conference and Exposition on Experimental and Applied Mechanics, Charlotte, North Carolina, Session 77, Paper 105, (June 2-4, 2003).

7. Manges W.W., Warmack R.J., Britton Jr. C.L., Bryan W.L., Simpson M.L., Smith S.F., Scott K.J., Jacobson K.B., Thundat T.G., Wintenberg A.L., Oden P.I., Howell Jr. L.N., Hosker Jr. R.P. and Auble D.L., *A New Microtelesensor Chip for Meteorology*, Proceedings of the Seventh Atmospheric Radiation Measurement (ARM), Science Team Meeting, San Antonio, Texas, (1997).

8. Wang Y.H., Lee C.Y. and Chiang C.M., *A MEMS-based Air Flow Sensor with a Free-standing Micro-cantilever Structure*, Sensors, **7**, (2007), 2389-2401.

9. Tiliakos N., Papadopoulos G., O´Grady A., Modi V., Larger R. and Frechette L., *A MEMS-based Shear Stress Sensor for High Temperature Applications*, 46th American Institute of Aeronautics and Astronautics (AIAA) Aerospace Sciences Meeting and Exhibit, Reno, Nevada, 092407, (January 7-10, 2008), 1-9.

10. Eyre B., Miller L. and Pister K.S.J., *MEMS Magnetic Sensor in Standard CMOS*, Science Closure and Enabling Technologies for Constellation Class Missions, (1998), 99-102.

11. Mutyala M.S.K., Bandhanadham D., Pan L., Pendyala V.R. and Ji H.F., *Mechanical and Electronical Approaches to improve the Sensitivity of Microcantilever Sensors*, Acta Mechanica Sinica, **25**, (2009), 1-12.

12. Lechuga L.M., Tamayo J., Álvarez M., Carrascosa L.G., Yufera A., Doldán R., Peralías E., Rueda A., Plaza J.A., Zinoviev K., Domínguez C., Zaballos A., Moreno M., Martínez-A C., Wenn D., Harris N., Bringer C., Bardinal V., Camps T., Vergnenégre C., Fontaine C., Díaz V. and Bernad A., *A Highly Sensitive Microsystem Based on Nanomechanical Biosensors for Genomic Applications*, Sensors and Actuators B, **118**, (2006), 2-10.

13. Hwang K.S., Lee S.M., Kim S.K., Lee J.H. and Kim T.S., *Micro- and Nanocantilever Devices and Systems for Biomolecule Detection*, Annual Review of Analytical Chemistry, **2**, (2009), 77-98.

14. Ansari M.Z. and Cho C., *Design and Analysis of a high sensitive Microcantilever Biosensor for Biomedical Applications*, IEEE International Conference on Biomedical Engineering and Informatics, (2008), 593-597.

15. Voiculecsu I., Zahgloul M.E., McGill R.A., Houser E.J. and Fedder G.K., *Electrostatically Actuated Resonant Microcantilever Beam in CMOS Technology for the Detection of Chemical Weapons*, IEEE Sensors Journal, **5** (4), (2005), 641-647.

16. Ocakli H.I., *Fabrication and Characterization of Magnetic Microresonators*, M.S. Thesis, Koc University, (July 2008).

17. Ozturk A., *Development of a Diffraction-Grating-Based Micro-Gravimetric Sensing Method for Biological Applications*, M.S. Thesis, Koc University, (July 2008).

18. Yu H. and Li X., *Bianalyte Mass Detection with a single Resonant Cantilever*, Applied Physics Letters, **94**, (2009), 011901.

19. Tamayo J., Ramos D., Mertens J. and Calleja M., *Effect of the Adsorbate Stiffness on the Resonance Response of Microcantilever Sensors*, Applied Physics Letters, **89**, (2006), 224104.

20. Kilic M.S., *Investigation of a Microgravimetric Sensor and an Application to the Detection of Protein-Antibody Interaction*, M.S. Thesis, Koc University, (September 2009).

21. Rao P.D.S., *Strength of Materials (A Practical Approach)*, Universities Press (India), **1**, (1999).

22. Mills I., Cvitaš T., Homann K., Kallay N. and Kuchitsu K., *Quantities, Units and Symbols in Physical Chemistry*, International Union of Pure and Applied Chemistry Physical Chemistry Division (IUPAC), Blackwell Science, 2nd Edition.

23. Kim S.H. and Boyd J.G., *A new technique for measuring Young's Modulus of Electroplated Nickel using AFM*, Measurement Science & Technology, **17**, (2006), 2343-2348.

24. Liang C. and Prorok B.C., *Measuring the thin film elastic modulus with a magnetostrictive sensor*, Journal of Micromechanics and Microengineering, **17**, (2007), 709-716.

25. He S., Chang J.S., Li L. and Ho H., *Characterization of Young's Modulus and Residual Stress Gradient of MetalMUMPs electroplated nickel film*, Sensors and Actuators A: Physical, **154**, (2009), 149-156.

26. Fritz T., Griepentrog M., Mokwa W. and Schnakenberg U., *Determination of Young's Modulus of electroplated nickel*, Electrochimica Acta, **48**, (2003), 3029-3035.

27. Luo J.K., Flewitt A.J., Spearing S.M., Fleck N.A. and Milne W.I., *Young's Modulus of electroplated Ni thin film for MEMS applications*, Materials Letters, **58**, (2004), 2306-2309.

28. Baek C.W., Kim Y.K., Ahn Y. and Kim Y.H., *Measurement of the mechanical properties of electroplated gold thin films using micromachined beam structures*, Sensors and Actuators A, **117**, (2005), 17-27.

29. Nilsson S.G., Borrisé X. and Montelius L., *Size effect on Young's Modulus of thin chromium cantilevers*, Applied Physics Letters, **85** (16), (2004), 3555-3557.

30. Kiesewetter L., Zhang J.M., Houdeau D. and Steckenborn A., *Determination of Young's moduli of micromechanical thin films using the resonance method*, Sensors and Actuators A, **35**, (1992), 153-159.

31. Petersen K.E., *Young's modulus measurements of thin films using micromechanics*, Journal of Applied Physics, **50**, (1979), 6761-6766.

32. Berkowski K.L., Plunkett K.N., Yu Q. and Moore J.S., *Introduction to Photolithography: Preparation of Microscale Polymer Silhouttes*, Journal of Chemical Education, **82** (9), (2005), 1365-1369.

33. Madou M. J., *Fundamentals of Microfabrication*, CRC Press, (1997).

34. De Los Santos H.J., Fischer G., Tilmans H.A.C. and van Beek J.T.M., *Fabricación de RF MEMS*, (2009).

35. Xuefeng D., *Microfabrication Using Bulk Wet Etching with TMAH*, M.S. Thesis, McGill University, (August 2005).

36. McKendry R., Zhang J., Arntz Y., Strunz T., Hegner M., Lang H.P., Baller M.K., Certa U., Meyer E., Güntherodt H.J. and Gerber C., *Multiple label-free biodetection and quantitative DNA-binding assays on a nanomechanical cantilever array*, Proceedings of the National Academy of Sciences, **99** (15), (July 23, 2002), 9783-9788.

37. Sadeghian H., Goosen J.F.L., Bossche A. and van Keulen F., *A Mechanistic Model for Adsorption-Induced change in Resonance Response of Submicron Cantilevers*, MEMS/MOEMS Components and Their Applications V. Special Focus Topics: Transducers at the Micro-Nano Interface, Proceedings of SPIE, **6885**, **68850E**, (January 19-24, 2008), 1-8.

38. Ono T., Li X., Miyashita H. and Esashi M., *Mass sensing of adsorbed molecules in sub-picogram sample with ultrathin silicon resonator*, Review of Scientific Instruments, **74** (3), (2003), 1240-1243.

39. Timurdogan E., Ozber N., Nargul S., Yavuz S., Kilic M.S., Kavakli I.H., Urey H and Alaca B.E., *Detection of human κ-opioid antibody using microresonators with integrated optical readout*, Biosensors and Bioelectronics, **26** (1), (September 15, 2010), 195-201.

40. Sader J.E., Chon J.W.M. and Mulvaney P., *Calibration of Rectangular Atomic Force Microscope Cantilevers,* Review of Scientific Instruments, **70** (10), (1999), 3967-3969.

41. Sandberg R., Mølhave K., Boisen A. and Svendsen W., *Effect of Gold Coating on the Q-factor of a Resonant Cantilever*, Journal of Micromechanics and Micro engineering, **15**, (2005), 2249-2253.

42. Pai R.S., *Nickel Electroplating using Shipley Megaposit SPR 220 Positive Resist as a Mold*, University of Louisville Cleanroom, (2001).

43. Ozturk A., Ocakli H.I., Ozber N., Urey H., Kavakli I.H. and Alaca B.E., *A Magnetically Actuated Resonant Mass Sensor with Integrated Optical Readout*, IEEE Photonics Technology Letters, **20** (23), (December 1, 2008), 1905-1907.

44. Deqing W., Ziyuan S. and Tangshan K., *Composite plating of hard chromium on aluminum substrate*, Surface & Coatings Technology, **191**, (2005), 324-329.

45. Veeco® DEKTAK 8 Surface Profiler Manual.

46. Kawabata K., Tanaka T., Kitabatake A., Yamada K., Mikami Y., Kajioka H. and Toiyama K., *High Rate Sputtering for Ni films by an rf-dc coupled magnetron sputtering system with multipolar magnetic plasma confinement*, Journal of Vacuum Science & Technology A, **19** (4), (July / August 2001), 1438-1441.

47. O´Donnell K., Kostetsky J., Devito R., Bellido-Gonzalez V., Powell S. and Monaghan D., *A sputtered nickel under bump metallurgy structure for lead-free solder for use in flip chip packaging*, Flip Chip Conference, NEXX Systems, (2003), 1-6.

48. Yun M.H., Burrows V.A. and Kozicki M.N., *Analysis of KOH etching of (100) silicon on insulator for the fabrication of nanoscale tips*, Journal of Vacuum Science & Technology B, **16** (5), (September / October 1998), 2844-2848.

49. Virginia Semiconductor Inc., *Wet-Chemical Etching and Cleaning of Silicon*, (January 2003).

50. Cohen A.L., Lockard M.S., Kim K., Le Q.T., Zhang G., Frodis U., Mcpherson D.S. and Smalley D.R., *Electrochemical Fabrication Methods incorporating dielectric materials and/or using Dielectric Substrates*, United States Patent, 7524427, (2009).

51. Transene Company Inc., *Gold Etchants for Microelectronics Circuits*.

52. MicroChemicals GmbH, *Gold Etching*.

53. Williams K.R., Gupta K., Wasilik M., *Etch Rates for Micromachining Processing-Part II*, Journal of Microelectromechanical Systems, **12** (6), 2003, 761-778.

54. Marshall J.C., Herman D.L., Vernier P.T., DeVoe D.L. and Gaitan M., Young's *Modulus Measurements in Standard IC CMOS Processes Using MEMS Test Structures*, IEEE Electron Device Letters, **28** (11), (2007), 960-963.

55. Yaralioglu G.G., Ergun A.S., Bayram B., Marentis T. and Khuri-Yakub B.T., *Residual Stress and Young's Modulus Measurement of Capacitive Micromachined Ultrasonic Transducer Membranes*, IEEE Ultrasonics Symposium, (2001), 953-956.

56. Nilsson S.G., Sarwe E.L. and Montelius L., *Fabrication and mechanical characterization of ultrashort nanocantilevers*, Applied Physics Letters, **83** (990), (2003).

57. Sandberg R., Svendsen W., Mølhave K. and Boisen A., *Temperature and Pressure Dependence of Resonance in Multi-layer Micro cantilevers*, Journal of Micromechanics and Micro engineering, **15**, (2005), 1454-1458.

58. Young W.C. and Budynas R.G., *Roark's Formulas for Stress and Strain*, McGraw-Hill, (2002), 7th Edition.

59. *The Nature of Sound*, The Physics Hypertext book, Waves & Optics / Sound.

60. Schmid S., Wägli P. and Hierold C., *All-Polymer Micro string Resonant Humidity Sensor with Enhanced Sensitivity due to Change of Intrinsic Stress*, Proceedings of the Euro sensors Conference, Dresden, Germany, (2008), 697-700.

61. Hurley D.C. and Turner J.A., *Humidity effects on the determination of elastic properties by atomic force acoustic microscopy*, Journal of Applied Physics, **95** (5), (March 1, 2004), 2403-2407.

62. Govardhan K. and Alex Z.C., *Mems Based Humidity Sensor*, Proceedings of ISSS (International Conference on Smart Materials, Structures and Systems), Bangalore, India, **SE-04**, (July 28-30, 2005), 20-27.

63. Chen L.T., Lee C.Y. and Cheng W.H., *MEMS-based Humidity Sensor with Integrated Temperature Compensation Mechanism*, Sensors and Actuators A: Physical, **147**, (2008), 522-528.

64. Yunovich M., *Appendix Z – Electronics (Production & Manufacturing)*, Corrosion Cost.

65. Tamura H., Okuno Y. and Kato H., *Chemical Etching of ZnSe Crystals*, Journal of Electronic Materials, **23** (8), (1994), 835-838.

66. Brigham Young University Cleanroom, *Wet Chemical Etching of Metals and Semiconductors*.

VITA

Serhat Yavuz was born in Fatih, Istanbul on September 7th, 1985. He graduated from Private Beylikdüzü Fatih Science High School in 2003. He had his undergraduate studies at Koç University, Sarıyer, Istanbul and he received his Bachelor of Science Degree from the Mechanical Engineering Department. After graduation in 2008, he was accepted from the Department of Mechanical Engineering Department at Koç University Graduate School of Sciences and Engineering program. During his Master of Science period, he worked on *Biosensor Applications for the Detection of Various Substances with Microelectromechanical Systems (MEMS)* as an assistant student to the ongoing research project under the supervision of Assist. Prof. B. Erdem Alaca. His major interests in this project are Process Development for Micro-fabrication, Resonance Frequency Measurements, Mechanics of Micro-cantilever Resonators, and Finite Element Modeling of these devices.